First-principles investigation of equilibrium magnesium isotope fractionation among mantle minerals: Review and new data

Wenzhong Wang[1,2,3*], Zhongqing Wu[1,4], Shichun Huang[5], Fang Huang[4,6]

[1]Laboratory of Seismology and Physics of Earth's Interior, School of Earth and Space Sciences, University of Science and Technology of China, Hefei, Anhui 230026, China

[2]Earth and Planets Laboratory, Carnegie Institution for Science, Washington, DC 20015, USA

[3]Department of Earth Sciences, University College London, London WC1E 6BT, United Kingdom

[4]CAS Center for Excellence in Comparative Planetology, USTC, Hefei, Anhui 230026, China

[5]Department of Earth and Planetary Sciences, The University of Tennessee, Knoxville, TN, 37996 United States

[6]CAS Key Laboratory of Crust-Mantle Materials and Environments, School of Earth and Space Sciences, University of Science and Technology of China, Hefei, Anhui 230026, China

[*]Correspondence: Wenzhong Wang (wz30304@mail.ustc.edu.cn)

Abstract

Equilibrium inter-mineral Mg isotope fractionation factors ($10^3\ln\alpha$) are key for using Mg isotopes to investigate high-temperature geochemical processes. First-principles calculations based on density functional theory (DFT) has been proven to be a reliable approach to predict the reduced partition function ratio ($10^3\ln\beta$) and the inter-mineral $10^3\ln\alpha$ values, and there are large amounts of data calculated based on different methods in the literature. We here review previous DFT calculations on inter-mineral $10^3\ln\alpha$ of Mg isotopes and complement new calculations for some minerals, and thoroughly discuss and compare the results from different methods. Two types of approximations, the local density approximation (LDA) and the generalized gradient approximation (GGA), are adopted to model the exchange-correlation potential in DFT calculations. Static calculations and quasi-harmonic approximation (QHA) are both used to calculate the $10^3\ln\alpha$. In theory, the QHA method is more reliable but more computationally expensive than the static method, because the former derives the pressure- and temperature-dependent $10^3\ln\beta$ from its volume- and temperature-dependent form via the equation of states.

The structural and vibrational properties of mantle minerals predicted by the LDA calculations agree well with experimental results, while the GGA calculations overestimate the volumes and Mg-O bond lengths. There are systematic differences between the calculated $10^3\ln\beta$ values using static LDA and GGA calculations; however, both approaches predict similar inter-mineral $10^3\ln\alpha$ values at high temperatures because the systematic difference between two $10^3\ln\beta$ values cancels out. Furthermore, the inter-mineral $10^3\ln\alpha$ values predicted by the static LDA method generally agree with those from the LDA+QHA method, which is used to calculate the pressure effect on $10^3\ln\alpha$. Two sets of inter-mineral $10^3\ln\alpha$ values of $^{26}Mg/^{24}Mg$ calculated by static LDA and LDA+QHA methods are present as a function of temperature and/or pressure in this review. Large Mg isotope fractionation exists between some minerals, and inter-mineral $10^3\ln\alpha$ values could be significantly affected by pressure due to the difference

in the pressure slopes of their $10^3 \ln\beta$. The measured forsterite-magnesite and spinel-magnesite Mg isotope fractionation factors in previous experiments are consistent with the calculated results within uncertainties. Using the calculated data, we examine the degree to which the observed inter-mineral Mg isotope fractionation in natural rocks represents equilibrium and model the Mg isotope fractionation during late-stage basalt differentiation.

Keywords: first-principles calculations, equilibrium isotope fractionation, Mg isotopes, geothermometer, quasi-harmonic approximation, basalt differentiation

1. Introduction

Magnesium is a major rock-forming element. It is the fourth most common element in the Earth (McDonough and Sun, 1995) and the fifth most abundant element in the continental crust (Rudnick and Gao, 2014). Magnesium has three stable isotopes, ^{24}Mg, ^{25}Mg, and ^{26}Mg, with relative abundances of 78.99%, 10.00%, and 11.01%, respectively. The Mg isotope composition is usually reported as $\delta^{26}Mg = [(^{26}Mg/^{24}Mg)_{sample}/(^{26}Mg/^{24}Mg)_{standard} - 1]\times1000$ (‰), where $(^{26}Mg/^{24}Mg)_{standard}$ refers to the Mg isotopic ratio in a standard sample. Recent advances in Mg isotope analytical technique lead to an analytical precision of $\delta^{26}Mg$ to the level of < 0.1 ‰ (2SD), and large $\delta^{26}Mg$ variations were found in natural samples (see review in Young and Galy (2004) and Teng (2017)). This makes Mg isotopes a useful tool in the studies of a variety of geological processes, including chemical weathering and alteration (Brewer et al., 2018; Cuozzo et al., 2020; Huang et al., 2018, 2016, 2012; Li et al., 2010; Liu et al., 2014; Teng et al., 2010b), magma differentiation (Huang et al., 2011a; W.-Y. Li et al., 2016; Liu et al., 2011; Teng et al., 2007, 2010a; Wang et al., 2012, 2016; X.-J. Wang et al., 2021; Young et al., 2009), the recycling of surficial materials into the mantle (Hu et al., 2020, 2017; Huang et al., 2015; S.-G. Li et al., 2016; Liu et al., 2010; Wang et al., 2014; X.-J. Wang et al., 2017; Yang et al., 2012), and planetary evolution (Hin et al., 2017; Young et al., 2019).

Applications of Mg isotopes in high-temperatures geochemical processes require the understanding of equilibrium mineral-melt and inter-mineral Mg isotope fractionation. The similar $\delta^{26}Mg$ values of mantle peridotites, mid-ocean ridge basalts, and ocean island basalts from different regions (e.g., Teng et al., 2010a, 2007) suggest a negligible Mg isotope fractionation during partial melting of mantle peridotites and basalt differentiation. This also reveals an unresolvable Mg isotope fractionation between olivine and melt ($\Delta^{26}Mg_{olivine\text{-}melt}$ = 0.0 ± 0.04 ‰) at magmatic temperatures when compared with the current levels of precision (Teng et al., 2010a, 2007). Mineral-melt Mg isotope fractionation for other minerals can be derived from the equilibrium mineral-olivine Mg isotope fractionation factors and $\Delta^{26}Mg_{olivine\text{-}melt}$. There are extensive studies in the literature investigating the $\delta^{26}Mg$ of constituent minerals in a variety of mantle xenoliths, including olivine, pyroxenes, garnet, and spinel (Chen et al., 2018; Handler et al., 2009; Yan Hu et al., 2016; Hu et al., 2020; Li et al., 2011; Liu et al., 2011; Stracke et al., 2018; Wang et al., 2015, 2012; Xiao et al., 2016, 2013; Young et al., 2009). These studies found that the orthopyroxene-olivine Mg isotope fractionation ($\Delta^{26}Mg_{orthopyroxene\text{-}olivine} = \delta^{26}Mg_{orthopyroxene} - \delta^{26}Mg_{olivine}$) ranges from -0.05 ± 0.14 ‰ to 0.25 ± 0.14 ‰ (2SD), and the measured $\Delta^{26}Mg_{cpx\text{-}ol}$ varies in a wide range from -0.25 ± 0.07 ‰ (Yan Hu et al., 2016) to +0.42 ± 0.14 ‰ (Young et al., 2009). The observed $\Delta^{26}Mg_{clinopyroxene\text{-}garnet}$ ranges from +0.11 ± 0.06 ‰ in garnet-bearing pyroxenites from Yan Hu et al. (2016) to +1.14 ± 0.04 ‰ in eclogites from Li et al. (2011), and the $\Delta^{26}Mg_{spinel\text{-}olivine}$ ranges from +0.17 ± 0.14 ‰ in north China craton peridotites from Xiao et al. (2013) to +0.87 ± 0.14 ‰ in San Carlos xenoliths from Young et al. (2009). The degree to which the observed inter-mineral fractionation in natural samples represents equilibrium warrants a closer examination.

Olivine- and spinel-carbonate Mg isotope fractionation factors, and hence the Mg isotope fractionation between spinel and forsterite ($\Delta^{26}Mg_{spinel\text{-}forsterite}$) have been determined experimentally using the three-isotope method (Macris et al., 2013; Tang et al., 2021). They reported large $\Delta^{26}Mg_{spinel\text{-}forsterite}$ values at 873-1073 K and 1 GPa, and

found that $\Delta^{26}Mg_{spinel\text{-}forsterite}$ is also affected by the Cr content in spinel. The Mg isotope fractionation factors among other minerals have not been yet investigated by experiments until now. Alternatively, first-principles calculations based on DFT have been widely used to determine the equilibrium isotope fractionation for many systems including Mg (Blanchard et al., 2017; Feng et al., 2014; Gao et al., 2018; Huang et al., 2014, 2013; Li et al., 2019b, 2019a; Méheut et al., 2009; Schauble, 2011; W. Wang et al., 2021b, 2021a, 2017b, 2017a; Wang et al., 2020a, 2019b; W. Wang et al., 2021e; Wu et al., 2015). Specifically, Schauble (2011) calculated the equilibrium Mg isotope fractionation factors among olivine, spinel, pyroxene, and magnesite at static 0 GPa. Huang et al. (2013) calculated the equilibrium Mg isotope fractionation factors among garnet, clinopyroxene, orthopyroxene, and olivine at various pressures and temperatures, and found a substantial pressure effect on the equilibrium Mg isotope fractionation among garnet, pyroxene, and olivine. These two studies used different approximations for the exchange-correlation potential (GGA vs. LDA) to perform the DFT calculations and different methods (the static method vs. the QHA method) to calculate the equilibrium Mg isotope fractionation factors from the Urey equation, but their results for the first order are consistent with each other at 0 GPa (Huang et al., 2013).

In this contribution, we review previous first-principles studies on the equilibrium Mg isotope fractionation among a variety of mantle minerals and present new calculated results for Fe-Ti oxides (magnesioferrite and ilmenite), which play an important role during late-stage basalt differentiation (e.g., X.-J. Wang et al., 2021). We thoroughly discuss the results calculated from different approximations for the exchange-correlation potential and different methods, and provide a full set of self-consistent equilibrium inter-mineral Mg isotope fractionation factors for future usage. Furthermore, we compare the theoretical results with experimental measurements, and use the data to examine whether the observed inter-mineral Mg isotope fractionation in mantle rocks represents equilibrium or not. Finally, we apply the fractionation data to

interpret the Mg isotope fractionation during late-stage basalt differentiation.

2. Methods

2.1 Equilibrium isotope fractionation factor

The equilibrium isotope fractionation factor between Phases A and B is defined as the ratio of the isotopic ratios in Phases A and B:

$$\alpha_{A\text{-}B}=R_A/R_B=(Y^*/Y)_A/(Y^*/Y)_B \quad (1)$$

where Y* and Y refer to the concentrations of two isotopes. In the theoretical calculations, the equilibrium isotope fractionation factor can be expressed as the ratio of the reduced partition function ratios (β factor) of the two phases:

$$\alpha_{A\text{-}B}=\beta_A/\beta_B \text{ or } 10^3\ln\alpha_{A\text{-}B}\ (‰)=10^3\ln\beta_A-10^3\ln\beta_B \quad (2)$$

The reduced partition function ratio of a given phase describes the isotopic fractionation between that specific phase and an ideal atomic gas. Following Bigeleisen and Mayer (1947) and Richet et al. (1977), based on the harmonic approximation and the Teller-Redlich rule, the reduced partition function ratio β_A of an element X in Phase A is given by:

$$\beta_A = \frac{Q_h}{Q_l} = \prod_i^{3N} \frac{u_{ih}}{u_{il}} \frac{e^{-\frac{1}{2}u_{ih}}}{1-e^{-u_{ih}}} \frac{1-e^{-u_{il}}}{e^{-\frac{1}{2}u_{il}}} \quad (3)$$

where *h* and *l* represent the heavy and light isotopes, respectively; Q_h and Q_l refer to the vibrational partition function for the heavy and light isotopes, respectively. The running index *i* refers to the vibrational frequency mode, and *N* is the number of atoms in the unit cell. Parameters u_{ih} and u_{il} are defined as:

$$u_{ih\ or\ il} = \hbar\omega_{ih\ or\ il}/k_BT \quad (4)$$

where $\hbar$ and k_B are the Planck and Boltzmann constants, respectively; $\omega_{ih\ or\ il}$ is the vibrational frequency; and *T* is the temperature in Kelvin. It can be noted that equilibrium isotope fractionation is related to the changes in vibrational frequencies caused by the isotopic substitution of an element in a given system (Bigeleisen and Mayer, 1947; Urey, 1947). Thus, deriving the equilibrium isotope fractionation factor requires calculations of vibrational properties.

Because the differences in vibrational frequencies caused by isotope substitution ($\Delta u_i = u_{il} - u_{ih}$) are very small, following the analysis in previous works (Bigeleisen and Mayer, 1947; Dauphas et al., 2012; Kowalski et al., 2013a; W. Wang et al., 2021e), Eq. (1) can be written as:

$$\beta = 1 + \sum_{i=1}^{3N} \left(\frac{1}{2} - \frac{1}{u_i} + \frac{1}{exp(u_i)-1}\right) \Delta u_i \quad (7)$$

The Taylor expansion of the function enclosed by the summation sign is:

$$G(u_i) = \frac{1}{2} - \frac{1}{u_i} + \frac{1}{\exp(u_i)-1} = \frac{u_i}{12} - \frac{{u_i}^3}{720} + \frac{{u_i}^5}{30240} - \frac{{u_i}^7}{1209600} + \cdots \quad (8)$$

When only the first term of the Taylor expansion is considered, the β factor is:

$$\beta = 1 + \sum_{i=1}^{3N} \frac{u_i}{12} \Delta u_i = 1 + \sum_{i=1}^{3N} \frac{{u_{il}}^2 - {u_{ih}}^2}{24} \quad (9)$$

As we only consider changes in vibrational frequencies caused by the isotopic substitution of the element of interest, Eq. (9) can be expressed as:

$$\beta = 1 + \sum_{i=1}^{3N} \frac{{u_{il}}^2 - {u_{ih}}^2}{24} = 1 + \left(\frac{1}{m_l} - \frac{1}{m_h}\right) \frac{\hbar^2}{24 {k_B}^2 T^2} \sum_{i=1}^{3} A_i$$

$$= 1 + \left(\frac{1}{m_l} - \frac{1}{m_h}\right) \frac{\hbar^2}{8 {k_B}^2 T^2} < F > \quad (10)$$

$$10^3 ln\beta = \left(\frac{1}{m_l} - \frac{1}{m_h}\right) \frac{\hbar^2}{8 {k_B}^2 T^2} < F > \quad (11)$$

where m_l and m_h are the masses of light and heavy isotopes, respectively. A_i $(i = 1, 2, 3)$ are the force constants acting on the isotopic atom in the three perpendicular spatial directions, and <F> is the average force constant. The use of Eq. (11) requires that frequencies related to the element of interest ω_i (cm^{-1}) are ≤ 1.39 T (T is the temperature in Kelvin).

2.2 Quasi-harmonic approximation

In general, the $10^3 ln\beta$ and $10^3 ln\alpha$ calculation procedures for solids involve three steps: (1) optimizing the solid structures under a certain pressure under static conditions; (2) calculating the vibrational properties of the relaxed structures with different isotope masses; and (3) deriving $10^3 ln\beta$ and $10^3 ln\alpha$ using Eqs. (3) and (2). The $10^3 ln\beta$ obtained using the static method is volume- and temperature-dependent because vibrational

frequencies from first-principles calculations are a function of volume. In many published studies (Blanchard et al., 2017; Feng et al., 2014; Gao et al., 2018; Li et al., 2019a, 2019b; Méheut et al., 2009; Schauble, 2011; W. Wang et al., 2017a; Wang et al., 2020a, 2019b; W. Wang et al., 2021e, 2021b, 2017b), the temperature-dependent $10^3\ln\beta$ values calculated from the vibrational frequencies at static 0 GPa (called the "static method" thereafter) are typically used to derive $10^3\ln\alpha$ at 0 GPa and different temperatures, without considering the temperature effect on volume. In theory, the solid volume increases with temperature at a certain pressure, and the temperature-dependent $10^3\ln\beta$ values at static 0 GPa are not the values at realistic 0 GPa and different temperatures. To address this issue, it is necessary to express $10^3\ln\beta$ as a function of both pressure (*P*) and temperature (*T*). The transform requires the equation of state *P(V, T)*, which can be derived from the Helmholtz free energy (*F*). Within the quasi-harmonic approximation (QHA), the Helmholtz free energy is expressed as:

$$F(V,T) = U(V) + \frac{1}{2}\sum_{q,i}\hbar\omega_{q,i}(V) + k_B T \sum_{q,i} ln\,(1 - \exp\,(-\frac{\hbar\omega_{q,i}(V)}{k_B T})) \quad (5)$$

where *q* is the wave vector in the Brillouin zone, and *i* is the running index of phonon mode. The first, second, and third terms in Eq. (5) correspond to the static, zero-point, and vibrational energy contributions, respectively. The calculated Helmholtz free energy versus volume was fitted by the third-order Birch-Murnaghan finite strain equation of state and the pressure can be derived from:

$$P(V,T) = -(\frac{\partial F}{\partial V})_T \quad (6)$$

Thus, the pressure- and temperature-dependent $10^3\ln\beta$ can be transformed from its volume- and temperature-dependent form via *P(V, T)*. We call this approach "QHA method" in this study. It should be noted that calculating $10^3\ln\beta$ for each mineral using the static method only needs to calculate the vibrational frequencies of the relaxed structure at static 0 GPa, while the QHA method requires the vibrational frequencies at different equilibrium volumes to obtain the pressure- and temperature-dependent $10^3\ln\beta$. Because the phonon calculations are computationally expensive, the QHA method costs at least 5-10 times more computation time than the static method. We will

compare the results calculated using these two different methods in section 4.2.

2.3 First-principles calculations

All first-principles calculations were performed using the Quantum Espresso package (Giannozzi et al., 2009) based on DFT, plane waves, and pseudopotentials. In principle, the DFT is an exact theory, but the accurate functional form is still unknown, and approximations such as the local density approximation (LDA) and the generalized gradient approximation (GGA) are required to model the exchange–correlation potential. Here we adopted the local density approximation (LDA) for the exchange correlation function, because it works well for calculating phonon properties and thermodynamic properties of mantle minerals (Duan et al., 2019; Hao et al., 2019; Yi Hu et al., 2016; Huang et al., 2013; Qian et al., 2018; Shukla et al., 2016, 2015; Wang et al., 2020c, 2019a; W. Wang et al., 2021c, 2021d; Wang et al., 2020b; Wang and Wu, 2018; Wentzcovitch et al., 2010; Wu and Wang, 2016; Yang et al., 2017; Yang and Wu, 2014; Yu et al., 2011, 2007; Zou et al., 2018). The pseudopotential for magnesium (Mg) was generated by the von Barth and Car method with a cutoff radius of 2.5 Bohr for all channels using five valence configurations, $3s^2 3p^0$, $3s^1 3p^1$, $3s^1 3p^{0.5} 3d^{0.5}$, $3s^1 3p^{0.5}$, and $3s^1 3d^1$ with decreasing weights of 1.5, 0.6, 0.3, 0.3, and 0.2, respectively. The pseudopotentials for silicon (Si) and oxygen (O) were generated using the method in Troullier and Martins (1991), with a valence configuration of $3s^2 3p^4 3d^0$ and a cutoff radius of 1.47 Bohr for Si and a valence configuration $2s^2 2p^4$ and a cutoff radius of 1.45 Bohr for O. The pseudopotentials for calcium (Ca), iron (Fe), titanium (Ti), chromium (Cr), aluminum (Al), and carbon (C) were generated using the Vanderbilt method (Vanderbilt, 1990). The cutoff radius is 1.85 Bohr for Ca with a valence configuration of $3s^2 3p^6 4s^1$, 1.8 Bohr for Fe with a valence configuration of $3s^2 3p^6 3d^{6.5} 4s^1 4p^0$, 1.8 Bohr for Ti with a valence configuration of $3s^2 3p^6 4s^2 3d^2$, 1.65 Bohr for Cr with a valence configuration of $3s^2 3p^6 4s^1 3d^5$, 1.77 Bohr for Al with a valence configuration of $3s^2 3p^1$, and 1.3 Bohr for C with a valence configuration of $2s^2 2p^2$. Pseudopotentials for

all elements included in this study except for Cr were used to predict the equilibrium isotope fractionation factors in our previous studies (Feng et al., 2014; Huang et al., 2014, 2013; Qin et al., 2016; W. Wang et al., 2021b, 2017a, 2017b; Wang et al., 2020a; Wu et al., 2015). The energy cutoff for plane waves was 70 Ry.

Although LDA has successfully predicted various properties of mantle minerals, it cannot sufficiently describe the large on-site Coulomb interactions among the localized electrons in open shell configurations (Anisimov et al., 1991). For instance, LDA gives a metallic band structure for FeO, failing to predict the insulating ground state because LDA does not properly describe the large on-site Coulomb interactions among the Fe's 3d electrons (Anisimov et al., 1991). To address this issue, we introduced a Hubbard U correction to the LDA (LDA+U) for Fe, Ti, and Cr. The LDA+U method has also been widely used to successfully predict the physical and chemical properties of Fe-bearing bridgmanite and ferropericlase (Hsu et al., 2011; Shukla et al., 2016, 2015; Shukla and Wentzcovitch, 2016; W. Wang et al., 2021c, 2021b; Wu et al., 2013). The U values were nonempirically determined using the linear response method (Cococcioni and de Gironcoli, 2005). In geikielite-ilmenite solid solutions, the U values for Fe and Ti are 3.6 and 4.1 eV (W. Wang et al., 2021d; Wang et al., 2020a), respectively. In Mg-bearing magnesioferrite ($MgFe_2O_4$), the U values are 3.3 and 3.7 eV for Fe^{3+} in octahedral and tetrahedral sites, respectively. The U value for Cr is 2.5 eV in Cr-bearing spinel ($MgCrAlO_4$ and $MgCr_2O_4$).

Crystal structures of all minerals investigated in this study were optimized at variable pressures using variable cell shape molecular dynamics (Wentzcovitch, 1991). To compare the structural properties calculated using different exchange–correlation functional approximations, we also conducted GGA calculations for some minerals to obtain their relaxed structures at static 0 GPa (Table 1). The residual forces converge within 10^{-4} Ry/Bohr. Brillouin zone summations over electronic states were performed over different mesh grids that depend on the unit cells of materials (Table S1). Vibrational density of states (VDOS) was calculated using the density-functional

perturbation theory (DFPT) for the LDA calculations without *U* correction and the finite displacement method as implemented in the code PHONOPYT (Togo and Tanaka, 2015) for the LDA+*U* calculations. For each mineral, we conducted VDOS calculations for at least seven volumes (corresponding to seven static pressures) to accurately calculate the *F* as a function of volume and temperature (Eq. (5)) (Wentzcovitch et al., 2010). To check the effect of the number of volumes on the calculated $10^3 \ln\beta$, we did the LDA calculations at more static pressures for forsterite and found that the difference in $10^3 \ln\beta$ between the results using seven and ten volumes is negligible.

3. Results

3.1 Mineral volumes and vibrational frequencies

The cell parameters and volumes of all minerals investigated in this study are listed in Table 1 and compared with experimental measurements. Compared to the experimental data under ambient conditions, the static LDA calculations underestimate the mineral volumes at 0 GPa by 1.0-3.4%, with the largest difference of -3.4% in magnesite volume (Fig. 1a). Except for magnesite, the volumes of other minerals predicted by the static LDA calculations are 1.0-2.5% lower than the experimental results. In contrast, the static GGA calculations from this study and Schauble (2011) overestimate the mineral volumes by 1.7-4.0% (Fig. 1a). This is consistent with the general concept that the LDA underestimates but the GGA overestimates the volumes of silicate minerals (Wentzcovitch et al., 2010). The static calculations do not include the vibrational effect on the mineral volumes. Based on the QHA, the mineral volumes predicted by the LDA calculations increase by 1.2-2.5% after considering the zero-point motion and room-temperature effect (Table 1 and Fig. 1a). Accordingly, the volume differences between the LDA calculations and experimental measurements are smaller than 1.0% under ambient conditions, and in particular, the differences for our studies minerals except for spinel, magnesiochromite, magnesite, and periclase are smaller than 0.5% (Fig. 1a). Additionally, our previous studies demonstrated that the volumes of

forsterite, diopside, orthopyroxene, magnesite, geikielite-ilmenite solid solutions, pyrope, majorite, wadsleyite, ringwoodite, bridgmanite, and periclase also agree well (< 1.0%) with high-quality experimental data at high pressures (Yi Hu et al., 2016; Núñez-Valdez et al., 2013; Núñez Valdez et al., 2012; Qian et al., 2018; Shukla et al., 2016, 2015; W. Wang et al., 2021d; Wu et al., 2013; Wu and Wang, 2016; Yao et al., 2018; Yu et al., 2011; Zou et al., 2018). All of our previous works and this study use the same LDA pseudopotentials and similar calculation details and consequently predict similar properties of those minerals. However, when the vibrational effect is included in the GGA calculations, GGA calculations will give even larger mineral volumes under ambient conditions, and therefore, the differences between the GGA results and experiments will become larger than those under static conditions. This suggests that the LDA is preferred for predicting the structures of mantle minerals.

The vibrational properties are sensitive to mineral structures such as lattice parameters. The calculated vibrational frequencies using the LDA are compared with the experimental measurements in Fig. 2. All raw data are available in Table S2. Our LDA results agree well with the experimental data, with the slope between the calculated frequencies and measured frequencies being 0.999±0.002 (1σ, R^2 = 0.9985) (Fig. 2). In contrast, the vibrational frequencies of forsterite, diopside, orthopyroxene, magnesite, spinel, and periclase calculated using the GGA in Schauble (2011) are slightly lower than our LDA results, and the slope between those GGA results and experimental data is 0.968±0.001 (1σ, R^2 = 0.9998). This suggests that both LDA and GGA calculations based on the periodic boundary conditions can predict the vibrational properties of mantle minerals well, and the LDA works better than the GGA. According to the error analysis on the β factor derived from Eq. (1), a deviation of n% in vibrational frequencies would cause an error of n% at low temperatures and 2n% at high temperatures in $10^3\ln\beta$ (Méheut et al., 2009). Therefore, the $10^3\ln\beta$ and $10^3\ln\alpha$ calculated using LDA in this study have errors of 0.2% and 0.3% at high temperatures, respectively. In comparison, the relative uncertainties derived from the GGA

calculations (Schauble, 2011) are 3.2% for $10^3\ln\beta$ and 4.5% for $10^3\ln\alpha$ at high temperatures.

3.2 Mg-O bond lengths

The average Mg-O bond lengths predicted by the LDA and GGA calculations are listed in Table 2 and compared with the experimental results at 300 K. Mg is sixfold coordinated in forsterite, diopside, orthopyroxene, magnesite, geikielite-ilmenite solid solutions, $^{M}MgFe_2O_4$ magnesioferrite, wadsleyite, ringwoodite, and periclase, while it is fourfold coordinated in $^{T}MgFe_2O_4$ magnesioferrite and spinel-magnesiochromite solid solutions (Table 2). In pyrope and bridgmanite, the coordination number (CN) of Mg is 8. Specifically, majorite has a tetragonal structure with a chemical formula of $Mg_3(MgSi)(SiO_4)_3$, in which three Mg cations are eightfold coordinated and one Mg cation is sixfold coordinated. Thus, the average CN of Mg in majorite is 7.5. The average Mg-O bond lengths calculated using the LDA range from 1.9295 Å in $MgAl_2O_4$ spinel to 2.2641 Å in pyrope at static 0 GPa. It increases in the order of spinel ($MgAl_2O_4$) < spinel ($MgAlCrO_4$) < magnesiochromite ($MgCr_2O_4$) < magnesioferrite ($^{T}MgFe_2O_4$) < diopside ~ ringwoodite < magnesioferrite ($^{M}MgFe_2O_4$) < wadsleyite < magnesite < geikielite ($MgFeTi_2O_6$) ~ orthopyroxene ~ geikielite ($MgTiO_3$) ~ geikielite ($Mg_2Fe_4Ti_6O_{18}$) < forsterite ~ periclase < bridgmanite < majorite < pyrope. The static LDA calculations predict slightly shorter, by -1.3 – -0.3%, average Mg-O bond lengths than experiments for all studied minerals except for $MgAl_2O_4$ spinel. The calculated average Mg-O bond length in $MgAl_2O_4$ spinel is ~+0.2% longer than the experimental data (Fig. 1b and Table 2). In contrast, the static GGA calculations give longer, by +0.6% to +2.0%, average Mg-O bond lengths in all minerals than the experimental results (Fig. 1b).

Similar to the volume predictions, the static calculations of Mg-O bond length do not include the temperature effect. To account for this effect on the average Mg-O bond lengths, we first calculated the average Mg-O bond lengths at different equilibrium

volumes (corresponding to different hydrostatic pressures) for each mineral and found that they linearly increase with volumes (Fig. S1). Based on these linear relationships, we then used the calculated mineral volumes under ambient conditions (Table 1) to recalculate the Mg-O bond lengths at 300 K and 0 GPa. The calculated average Mg-O bond lengths under ambient conditions based on this LDA+QHA method agree well with the experimental results, and the differences are smaller than 0.4%, except for $MgAl_2O_4$ spinel (Fig. 1b). Because the average Mg-O bond length in $MgAl_2O_4$ spinel at static 0 GPa is already ~+0.2% longer than the experimental data, the difference between the LDA calculations and experiments increases to ~+0.9% for $MgAl_2O_4$ spinel at 300 K and 0 GPa (Fig. 1b). Such a difference is much smaller than those between the GGA calculations and experiments if the temperature correction is made. Collectively, the LDA calculations in this study can predict the mineral structures, vibrational properties, and bond lengths well, suggesting that the calculated $10^3\ln\beta$ and $10^3\ln\alpha$ are reliable and accurate.

3.3 Reduced partition function ratios of $^{26}Mg/^{24}Mg$

The $10^3\ln\beta$ of $^{26}Mg/^{24}Mg$ calculated based on the static LDA method are shown in Fig. 3a, and their polynomial fitting parameters of $10^3\ln\beta$ as a function of temperature are reported in Table 3. The $10^3\ln\alpha$ values between other minerals and forsterite are shown in Fig. 3b. The $10^3\ln\beta$ decreases in the order of spinel ($MgAl_2O_4$) > spinel ($MgAlCrO_4$) > ringwoodite > magnesiochromite ($MgCr_2O_4$) > wadsleyite > diopside ~ periclase > magnesioferrite ($^{T}MgFe_2O_4$) ~ magnesioferrite ($^{M}MgFe_2O_4$) ~ orthopyroxene > forsterite > bridgmanite > magnesite > geikielite ($MgTiO_3$) ~ geikielite ($MgFeTi_2O_6$) ~ geikielite ($Mg_2Fe_4Ti_6O_{18}$) > majorite > pyrope. At 1000 K, $10^3\ln\beta$ ranges from 3.51 ‰ for $MgAl_2O_4$ spinel to 1.58 ‰ for pyrope, suggesting that large Mg isotope fractionation can occur at high temperatures (Li et al., 2011; Schauble, 2011; Wang et al., 2012; Young et al., 2009). For instance, the calculated $10^3\ln\alpha$ values between forsterite and pyrope and between forsterite and $MgAl_2O_4$ spinel are +0.97 ‰

and -0.96 ‰ at 1000 K, respectively.

In spinel-magnesiochromite solid solutions, $10^3\ln\beta$ decreases with increasing Cr/(Al+Cr) ratio (called "Cr#"), indicating that Al-Cr substitution significantly affects $10^3\ln\alpha$ between spinel and other minerals, which has been confirmed by previous experiments (Tang et al., 2021). This is mainly because the replacement of Al by Cr significantly increases the volume and Mg-O bond lengths. For example, the relative differences in volume and average Mg-O bond length between $MgAlCrO_4$ and $MgAl_2O_4$ are +4.6% and +0.95%, respectively, leading to a difference in $10^3\ln\beta$ value of -0.39 ‰ at 1000 K and -3.65 ‰ at 300 K. However, Mg-Fe substitution in geikielite-ilmenite solid solutions does not substantially change the $10^3\ln\beta$ values, with differences of 0.05 ‰ and 0.39 ‰ between $MgTiO_3$ and $Mg_2Fe_4Ti_6O_{18}$ at 1000 K and 300 K, respectively. This is because Mg has a similar radius to Fe, and hence, the replacement of Mg by Fe does not significantly change the average Mg-O bond length in geikielite-ilmenite solid solutions. In comparison, previous studies (Feng et al., 2014; Li et al., 2019a; W. Wang et al., 2017b, 2017a) found that $10^3\ln\beta$ of $^{26}Mg/^{24}Mg$ for calcite-type carbonates, $10^3\ln\beta$ of $^{44}Ca/^{40}Ca$ for orthopyroxene, and $10^3\ln\beta$ of $^{41}K/^{39}K$ for feldspars are sensitive to carbonate Mg, orthopyroxene Ca, and feldspar K concentrations in wide ranges, respectively. The concentration effect on $10^3\ln\beta$ is due to the large difference in ionic radii between Mg and Ca and between K and Na. As such, Mg-Ca substitution in carbonates and orthopyroxene and K-Na substitution in feldspars result in large variations in the average Mg-O, Ca-O, and K-O bond lengths, respectively, and their $10^3\ln\beta$ values are negatively correlated with their average bond lengths (Feng et al., 2014; Li et al., 2019a; W. Wang et al., 2017b, 2017a). In summary, whether the concentration variation in solid solutions can affect their $10^3\ln\beta$ depends on the size difference between atoms or ions of interest. This observation is consistent with basic crystal chemistry in general if one treats the bond lengths as sums of ionic radii (Young et al., 2015).

In sections 3.1 and 3.2, we showed that using different exchange–correlation

potentials (LDA vs. GGA) in the DFT calculations can predict different structural and vibrational properties of mantle minerals. To check the effect of exchange–correlation potentials on the $10^3\ln\beta$ of $^{26}Mg/^{24}Mg$ and inter-mineral $10^3\ln\alpha$ values, we compare our static LDA results for forsterite, orthopyroxene, diopside, $MgAl_2O_4$ spinel, magnesite, and periclase with the static GGA calculations in Schauble (2011). Because the static GGA calculations predict larger mineral volumes and longer Mg-O bond lengths than the static LDA calculations (Tables 1 and 2, and Fig. 1), the $10^3\ln\beta$ of those minerals calculated using the GGA are smaller than our static LDA results. It is important to emphasize that the $10^3\ln\beta$ calculated based on different exchange–correlation potentials cannot be used to derive the $10^3\ln\alpha$ due to systematic offsets. However, in general, both LDA and GGA predict similar inter-mineral $10^3\ln\alpha$ values at 1000 K (Fig. 4), because the systematic offsets of $10^3\ln\beta$ are canceled out. For instance, based on the LDA calculations, we obtained $10^3\ln\alpha_{\text{orthopyroxene-forsterite}}$, $10^3\ln\alpha_{\text{diopside-forsterite}}$, and $10^3\ln\alpha_{\text{spinel-forsterite}}$ of +0.07 ‰, +0.20 ‰, and +0.97 ‰ at 1000 K, respectively, consistent with the values in Schauble (2011) who used GGA approach ($10^3\ln\alpha_{\text{orthopyroxene-forsterite}}$ = +0.08 ‰, $10^3\ln\alpha_{\text{diopside-forsterite}}$ = +0.13 ‰, and $10^3\ln\alpha_{\text{spinel-forsterite}}$ = +0.96 ‰). In detail, our LDA calculations give a $10^3\ln\alpha_{\text{magnesite-forsterite}}$ value of -0.14 ‰ at 1000 K, which has a smaller magnitude than the value of -0.33 ‰ given by Schauble (2011). Overall, the GGA is also a good approximation for the exchange-correlation potential for calculating the inter-mineral equilibrium isotope fractionation, but we prefer to use the LDA to predict the equilibrium isotope fractionation among mantle silicate minerals because of its reliability in predicting structural and vibrational properties (Figs. 1 and 2).

4. Discussion

4.1 Controlling factors on the $10^3\ln\beta$ of $^{26}Mg/^{24}Mg$

Mass-dependent equilibrium isotope fractionation factors are dominantly controlled by the relative bond stiffness (Bigeleisen and Mayer, 1947; Urey, 1947). In general, shorter chemical bonds are stiffer with higher vibrational frequencies, which

lead to enrichments of heavier isotopes relative to longer and weaker bonds (Hill and Schauble, 2008; Li et al., 2019b; Schauble et al., 2004; Schauble, 2011; Urey, 1947; Wang et al., 2020a). Thus, $10^3\ln\beta$ is mainly controlled by the bond length. This is supported by previous findings (Feng et al., 2014; Li et al., 2019a; W. Wang et al., 2017b, 2017a) that $10^3\ln\beta$ of $^{44}Ca/^{40}Ca$ for orthopyroxene, $10^3\ln\beta$ of $^{24}Mg/^{26}Mg$ for carbonates, and $10^3\ln\beta$ of $^{41}K/^{39}K$ for feldspars show a linear negative correlation with their average Ca-O, Mg-O, and K-O bond lengths, respectively. For all minerals investigated in this study, our static LDA results show that in general, $10^3\ln\beta$ of $^{24}Mg/^{26}Mg$ is negatively correlated with the average Mg-O bond length (Fig. 5a), but there is no good linear negative relation between them. This is because the bond stiffness is not only controlled by the bond length but also affected by other factors such as the CN and second-neighbor atoms (Huang et al., 2019; Li et al., 2019b; Rabin et al., 2021). In Ca-doped orthopyroxene, carbonates, and K-bearing feldspars, other structural properties, including the CNs for Ca, Mg, and K, are similar at different Ca, Mg, and K concentrations, so $10^3\ln\beta$ is dominantly controlled by the bond length and there is a linear negative relation between them (Feng et al., 2014; Li et al., 2019a; W. Wang et al., 2017b, 2017a). When different minerals are compared with each other, this study together with previous works on the $10^3\ln\beta$ of Ca, K, Fe, and Si isotopes for different minerals (Blanchard et al., 2017; Huang et al., 2019, 2014; Li et al., 2019b; Méheut et al., 2009; Qin et al., 2016; Rabin et al., 2021; W. Wang et al., 2021b) show that $10^3\ln\beta$ is affected by multiple structural factors including the bond length, CN, oxidation state, electronic configuration, and second-neighbor atoms, which jointly determine the bond stiffness.

Bond stiffness can be approximatively measured by the force constant (<F>) (Eq. (11)). Following Dauphas et al. (2012), the <F> of the atom of interest can be calculated from its projected partial phonon density of states (PDOS) using:

$$< F >= \frac{M}{\hbar^2}\int_0^{+\infty} E^2\, g(E)dE \quad (12)$$

where $g(E)$ is PDOS and M is the atomic mass. In experiments, the PDOS of some

isotopes such as ^{57}Fe, ^{83}Kr, and ^{119}Sn can be measured by the technique of nuclear resonant inelastic X-ray scattering (NRIXS) (Dauphas et al., 2018, 2014; Liu et al., 2017; Roskosz et al., 2020; Shahar et al., 2016; W. Wang et al., 2021b; Yang et al., 2019), while the VDOS calculations based on the DFT can give the <F> and PDOS of each atom in materials (see Methods). The average <F> of Mg in all investigated minerals calculated using LDA are reported in Table 2, ranging from 110.1 N/m in pyrope to 223.7 N/m $MgAl_2O_4$ in spinel. The 10^3lnβ of ^{24}Mg/^{26}Mg linearly increases with <F> (Fig. 5b), consistent with the basic tenants of the equilibrium isotope fractionation (Ducher et al., 2018; Li et al., 2019b; W. Wang et al., 2021e; Wang et al., 2020a, 2019b).

Although the calculated data and the theoretical analyses match well, it is not clear whether one can calculate the 10^3lnβ of ^{24}Mg/^{26}Mg from <F> using Eq. (11) because it is an approximation of the Urey equation (Eq. (3)). The criteria for using Eq. (11) requires frequencies related to the element of interest ω_i (cm^{-1}) to be ≤ 1.39 T. This is the case for Mg in our investigated minerals: the vibrational frequencies related to Mg in all investigated minerals, except for magnesite, are smaller than 1400 cm^{-1} (Fig. 2). Magnesite has two frequencies higher than 1400 cm^{-1} (Fig. 2), but they are related to the vibrational modes of the C-O complex. Our static LDA results show that 10^3lnβ calculated from <F> using Eq. (11) agree well with those calculated from vibrational frequencies using Eq. (3) at 1000 K, with differences of < 0.02 ‰ (Fig. 6b).

We also calculated the 10^3lnβ of forsterite, orthopyroxene, magnesite, and spinel as a function of the upper-limit frequency values used in Eq. (3), and the results show that 10^3lnβ at 1000 K remains almost constant when the frequencies are larger than 800 cm^{-1} (Fig. 6a), suggesting that the majority of frequencies related to Mg atoms in minerals do not exceed 800 cm^{-1}. These comparisons suggest that Eq. (11) can be used to calculate the 10^3lnβ of ^{24}Mg/^{26}Mg from <F> at high temperatures, but it will result in larger uncertainties at low temperatures (< 600 K). Because of this reason, Eq. (11) is also called "the high-temperature approximation" of the Urey equation.

Eq. (11) provides a convenient way to approximately calculate the $10^3 \ln\beta$ if the <F> of the element of interest is well-known. However, the <F> of most elements cannot be directly measured by experiments, although some can be obtained from the PDOS measured by the NRIXS technique. On the other hand, when a Born-Mayer type interionic potential was adopted, the <F> can be directly calculated from the interionic distance, which is referred as the "ionic model" (Young et al., 2015). Equilibrium isotope fractionation factors estimated from the ionic model are usually within a factor of ~2 or 3 of the DFT calculations, but this empirical model provides a straightforward framework for understanding how the crystal chemistry affects the equilibrium isotope fractionation (Young et al., 2015). Whether the ionic model can be used to accurately predict isotope fractionation factors depends on the reliability of Born-Mayer type interionic potential that mimics the realistic interatomic interaction.

4.2 Temperature and pressure dependences of equilibrium Mg isotope fractionation

The β factors in Eq. (3) are volume- and temperature-dependent because phonon frequencies from the DFT calculations are a function of volume. It is more practical to express $10^3 \ln\beta$ as a function of *P* and *T*. Here, we calculate the $10^3 \ln\beta$ of $^{24}Mg/^{26}Mg$ for all minerals at high pressures and temperatures based on the LDA+QHA method (see Methods), which are plotted in Fig. 7. The temperature and pressure dependences of $10^3 \ln\beta$ are fitted by a binary polynomial equation: $10^3 \ln\beta$ (‰) = $(a+b*P+c*P^2)*(10^6/T^2)+(d+e*P+f*P^2)*(10^6/T^2)^2+(g+h*P+l*P^2)*(10^6/T^2)^3$. The polynomial fitting parameters (a, b, c, d, e, f, g, h, and l) are reported in Table 4, and the $10^3 \ln\alpha$ values between other minerals and forsterite as a function of temperature at different pressures are shown in Fig. 8. It should be noted that the $10^3 \ln\beta$ values calculated based on the LDA+QHA method are lower than those predicted by the static LDA method at 0 GPa (Tables 3 and 4; Figs. 3 and 7). For example, the $10^3 \ln\beta$ of forsterite from the LDA+QHA calculations is 2.19 ‰ at 1000 K, significantly lower

than that (2.55 ‰, Table 3) given by the static LDA calculations. This is because the static method does not consider the volume change with temperature, and $10^3\ln\beta$ at different temperatures are calculated from the vibrational frequencies of the static structures at 0 GPa using Eq. (3). However, the inter-mineral $10^3\ln\alpha$ values calculated from the static LDA method generally agree well with those calculated from the LDA+QHA method at 0 GPa (Fig. 9). For instance, the $10^3\ln\alpha_{\text{orthopyroxene-forsterite}}$, $10^3\ln\alpha_{\text{diopside-forsterite}}$, and $10^3\ln\alpha_{\text{spinel-forsterite}}$ from the static LDA calculations are +0.07 ‰, +0.20 ‰, and +0.97 ‰ at 1000 K, respectively, consistent with the values predicted by the LDA+QHA method ($10^3\ln\alpha_{\text{orthopyroxene-forsterite}}$ = +0.13 ‰, $10^3\ln\alpha_{\text{diopside-forsterite}}$ = +0.17 ‰, and $10^3\ln\alpha_{\text{spinel-forsterite}}$ = +0.96 ‰). In theory, compared to the static method, it is more accurate and reliable to use the QHA method to calculate $10^3\ln\beta$ at different temperatures and 0 GPa, but this approach is more computationally expensive because the phonon frequencies at several different equilibrium volumes are required (see Methods). If the pressure effect is ignored, it is more convenient and less costly to use the static method to predict $10^3\ln\alpha$, and such a method has been widely used to predict equilibrium fractionation of various isotopes in previous studies (Feng et al., 2014; Fujii et al., 2014, 2011; Gao et al., 2018; Kowalski et al., 2013b; Kowalski and Jahn, 2011; Li and Liu, 2011; Li et al., 2019a, 2019b; Méheut et al., 2009; Qin et al., 2016; Schauble, 2011; W. Wang et al., 2017b, 2017a; Wang et al., 2020a, 2019b). It is noteworthy that two groups of $10^3\ln\beta$ calculated from the static and QHA methods cannot be compared with each other to obtain the $10^3\ln\alpha$ values due to systematic offsets. Combining this study with our previous studies (Huang et al., 2013; W. Wang et al., 2017b, 2017a), all of which use the same pseudopotentials and similar calculation details, we summarize two sets of $10^3\ln\beta$ for calculating the inter-mineral equilibrium Mg isotope fractionation calculated by the static LDA and LDA+QHA methods in Tables 3 and 4, respectively. The $10^3\ln\beta$ and $10^3\ln\alpha$ discussed hereafter are calculated based on the LDA+QHA method unless otherwise specified.

The $10^3\ln\beta$ of all minerals increase with pressure because increasing pressure will

decrease mineral volumes, and thus increase the strength and stiffness of Mg-O bonds. For instance, at 1000 K, the 10^3lnβ of forsterite and pyrope significantly increase from 2.19 ‰ and 1.30 ‰ at 0 GPa to 2.83 ‰ and 1.66 ‰ at 10 GPa (Table 4 and Fig. 7), respectively. The second pressure derivatives (fitting parameters c, f, and l) of 10^3lnβ are two orders of magnitude lower than the first pressure derivatives (fitting parameters b, e, and h) (Table 4), suggesting that 10^3lnβ linearly increases with pressure. However, different minerals have different first pressure derivatives, ranging from 0.028 ‰/GPa for pyrope to 0.082 ‰/GPa for diopside at 1000 K (Table 4). These various pressure slopes indicate that the inter-mineral 10^3lnα could be significantly affected by pressure. If 10^3lnβ of two minerals increase with similar magnitudes with increasing pressure, then the inter-mineral 10^3lnα will not be influenced by pressure. Otherwise, pressure will inevitably affect 10^3lnα.

Our results show that diopside, orthopyroxene, spinel, and magnesioferrite are enriched in heavy Mg isotopes compared with forsterite, while magnesite, pyrope and geikielite-ilmenite solid solutions are enriched in light Mg isotopes relative to forsterite (Fig. 8). Previous experiments found that Mg mainly occupies the octahedral site in $MgFe_2O_4$ magnesioferrite with the structural configurations of $^{T}(Mg_{0.16}Fe_{0.84})^{M}(Mg_{0.84}Fe_{1.16})O_4$ and $^{T}(Mg_{0.28}Fe_{0.72})^{M}(Mg_{0.72}Fe_{1.28})O_4$ at 873 K and 1300 K (O'Neill et al., 1992), respectively. Thus, the results for $MgFe_2O_4$ magnesioferrite with ~75% octahedral Mg and 25% tetrahedral Mg are used in our further discussion on high-temperature fractionation. The magnitude of $10^3\ln\alpha_{\text{pyrope-forsterite}}$ is significantly enhanced by pressure, but $10^3\ln\alpha_{\text{magnesioferrite-forsterite}}$ substantially decreases with pressure. For instance, at 1000 K, the magnitude of $10^3\ln\alpha_{\text{pyrope-forsterite}}$ increases from -0.88 ‰ at 0 GPa to -1.16 ‰ at 10 GPa due to the large difference in the pressure slopes of 10^3lnβ (Table 4), while the $10^3\ln\alpha_{\text{magnesioferrite-forsterite}}$ decreases from +0.29 ‰ at 0 GPa to +0.05 ‰ at 10 GPa. In comparison, the pressure effects on 10^3lnα between other minerals (diopside, orthopyroxene, magnesite, spinel, and geikielite-ilmenite solid solutions) and forsterite are less pronounced, with a variation

of < 0.13 ‰ in the range of 0-10 GPa at 1000 K. It can be inferred that the $10^3\ln\alpha$ between other minerals (such as diopside and orthopyroxene) and pyrope also significantly depend on pressure. Specifically, regardless of the magnitude of the pressure effect, both $10^3\ln\alpha_{\text{spinel-forsterite}}$ and $10^3\ln\alpha_{\text{magnesioferrite-forsterite}}$ decrease with pressure, because the $10^3\ln\beta$ of spinel and magnesioferrite increase more slowly with pressure than that of forsterite (Table 4). In contrast, the magnitudes of $10^3\ln\alpha$ between other minerals (diopside, orthopyroxene, magnesite, pyrope, and geikielite-ilmenite solid solutions) and forsterite are enhanced by pressure (Fig. 8).

4.3 Mg isotope fractionation caused by phase transitions

The Earth's upper mantle is mainly composed of ~60% olivine, 15% garnet, 15% clinopyroxene, and 10% orthopyroxene (Ringwood, 1962), which can reproduce the seismic velocity and density profiles of the upper mantle (Duan et al., 2019; Dziewonski and Anderson, 1981; Yi Hu et al., 2016; Kennett et al., 1995; Zou et al., 2018). Forsterite, pyrope, and diopside are the most important endmembers of olivine, garnet, and clinopyroxene in the upper mantle, respectively. With increasing depth, olivine transforms to wadsleyite at ~410 km, then to ringwoodite at ~520 km, and finally decomposes into bridgmanite and periclase (which is also called the "post-spinel transition") at ~660 km (Akaogi et al., 1989; Bina and Helffrich, 1994; Fei et al., 2004; Helffrich and Wood, 2001; Hirose, 2002; Inoue et al., 2006; Katsura et al., 2004; Katsura and Ito, 1989; Tsujino et al., 2019; Yu et al., 2008). It has been widely accepted that olivine-wadsleyite, wadsleyite-ringwoodite, and post-spinel phase transitions result in the seismic 410-km, 520-km, and 660-km discontinuities (e.g., Kind and Li, 2015 and references therein), respectively. Meanwhile, clinopyroxene and orthopyroxene are gradually dissolved into garnet with increasing depth to form majoritic garnet at the bottom of the upper mantle, and the volume fraction of majorite is up to 35% in the mantle transition zone (MTZ) (Ita and Stixrude, 1992; Ringwood, 1962). Under the conditions of the uppermost lower mantle, majorite transforms to

bridgmanite (Hirose, 2002; Yu et al., 2011), which is thought to be responsible for the multiple discontinuities at approximately 660 km detected by seismic studies (Ai and Zheng, 2003; Cottaar and Deuss, 2016; Deuss, 2009, 2006; Gao et al., 2010; Schultz and Gu, 2013). These phase transitions in the Earth's mantle lead to large differences in structural properties between minerals and hence likely cause Mg isotope fractionation.

Our results show that the enrichment of heavy Mg isotopes in Mg_2SiO_4 minerals follows the order of ringwoodite > wadsleyite > forsterite (Fig. 9 and Table 4) because ringwoodite and wadsleyite have shorter Mg-O bonds and hence larger <F> of Mg than forsterite (Table 2). The $10^3\ln\alpha_{wadsleyite\text{-}forsterite}$ and $10^3\ln\alpha_{ringwoodite\text{-}wadsleyite}$ are +0.08 ‰ under 410-km conditions (~14 GPa and 1700 K) and +0.05 ‰ under 520-km conditions (~18.5 GPa and 1830 K), respectively. The post-spinel transition will enrich bridgmanite and periclase with light Mg isotopes relative to ringwoodite, with a $10^3\ln\alpha_{bridgmanite\text{-}ringwoodite}$ value of -0.26 ‰ and a $10^3\ln\alpha_{periclase\text{-}ringwoodite}$ value of -0.13 ‰ at 660-km conditions (~23.5 GPa and 1890 K). Majorite is enriched in light Mg isotopes relative to clinopyroxene and orthopyroxene, consistent with a much longer average Mg-O bond length in majorite than those in clinopyroxene and orthopyroxene (Table 2). The $10^3\ln\alpha_{majorite\text{-}diopside}$ is -0.33 ‰ and the $10^3\ln\alpha_{majorite\text{-}orthopyroxene}$ is -0.28 ‰ under 410-km conditions (Table 4). In contrast, majorite ($^{VIII}Mg_3{}^{VI}(MgSi)(SiO_4)_3$) is enriched in heavy Mg isotopes relative to pyrope ($^{VIII}Mg_3{}^{VI}(Al_2)(SiO_4)_3$) with a $10^3\ln\alpha_{majorite\text{-}pyrope}$ of +0.20 ‰ at 14 GPa and 1700 K because a quarter of Mg in majorite occupies the octahedral site with a much shorter average Mg-O bond length (Table 2). For the majorite-bridgmanite transition, $10^3\ln\alpha_{bridgmanite\text{-}majorite}$ is +0.06 ‰ at 24 GPa and 1900 K (Table 4). Our calculations reveal that phase transitions in the Earth's mantle can induce significant inter-mineral Mg isotope fractionation under mantle *P-T* conditions. Similarly, Si isotopes can be fractionated among different mantle minerals (Huang et al., 2014; Wu et al., 2015).

The Mg_2SiO_4 and $MgSiO_3$ phase transitions may induce Mg isotope fractionation in the deep mantle if the primordial mantle has not been fully homogenized by mantle

615 convection. To constrain how the crystallization of different mantle layers from a hot
616 magma ocean fractionate Mg isotopes, we assume that no Mg isotope fractionation
617 occurs between olivine and melt at the temperature of magma ocean crystallization (>
618 3500 K). As such, the $10^3\ln\alpha_{mineral\text{-}melt}$ (minerals=wadsleyite, ringwoodite, majorite,
619 bridgmanite, and periclase) would be equal to $10^3\ln\alpha_{mineral\text{-}olivine}$., and the $10^3\ln\alpha_{wadsleyite\text{-}melt}$, $10^3\ln\alpha_{ringwoodite\text{-}melt}$, and $10^3\ln\alpha_{majorite\text{-}melt}$ will be smaller than +0.02 ‰, +0.03 ‰,
621 and -0.05 ‰, respectively. Considering the mineral proportions in the MTZ, the
622 $10^3\ln\alpha_{solid\text{-}melt}$ will be ~ -0.00 ‰ at 410-520 km and +0.01 ‰ at 520-660 km. Such small
623 fractionation factors cannot result in any resolvable Mg isotope fractionation between
624 minerals and residual melt, even if the primordial MTZ can be partially preserved or
625 isolated from mantle convection since its formation. For the lower mantle, the
626 magnitude of the estimated $10^3\ln\alpha_{solid\text{-}melt}$ will be smaller than -0.03 % at > 3500 K,
627 indicating no significant Mg isotope fractionation during the crystallization of lower-
628 mantle minerals. Therefore, the bulk Mg isotope composition of the primordial deep
629 mantle could be similar to that of the upper mantle. It should be noted that the
630 $10^3\ln\alpha_{olivine\text{-}melt}$ is assumed to be 0.00 ‰ at all pressures, which needs to be examined
631 by future studies especially at high pressures.
632
633 **4.4 Comparisons with experiments**
634 The three-isotope method has been used to investigate the high-temperature
635 fractionation factors for many isotopic systems including Fe, Ni, and Si isotopes (Lazar
636 et al., 2012; Shahar et al., 2011, 2009, 2008). This method was also applied to determine
637 the Mg isotope fractionation factors between forsterite and magnesite ($\Delta^{26}Mg_{forsterite\text{-}magnesite} = \delta^{26}Mg_{forsterite} - \delta^{26}Mg_{magnesite}$) and between spinel ($MgAl_2O_4$, $MgAlCrO_4$, and
639 $MgCr_2O_4$) and magnesite ($\Delta^{26}Mg_{spinel\text{-}magnesite}$) at 1 GPa and different temperatures, from
640 which the Mg isotope fractionation between spinel and forsterite can be derived
641 ($\Delta^{26}Mg_{spinel\text{-}forsterite} = \Delta^{26}Mg_{spinel\text{-}magnesite} - \Delta^{26}Mg_{forsterite\text{-}magnesite}$) (Macris et al., 2013; Tang
642 et al., 2021). The experimental results show that $\Delta^{26}Mg_{forsterite\text{-}magnesite}$ is +0.04 ± 0.04 ‰

643 at 1073 K, +0.11 ± 0.10 ‰ at 973 K, and 0.44 ± 0.10 ‰ 873 K (Macris et al., 2013).
644 Tang et al. (2021) recalculated the $\Delta^{26}Mg_{forsterite\text{-}magnesite}$ from the experiments of Macris
645 et al. (2013) for internal consistency using a slightly different data reduction method
646 for the three-isotope method, and found that $\Delta^{26}Mg_{forsterite\text{-}magnesite}$ is +0.08 ± 0.06 ‰,
647 +0.11 ± 0.17 ‰, and +0.32 ± 0.15 ‰ at 1073, 973, and 873 K, respectively. The
648 recalculated fractionation factors agree within uncertainty with those reported by in
649 Macris et al. (2013). Our results based on the LDA+QHA method show that the
650 $10^3ln\alpha_{forsterite\text{-}magnesite}$ is +0.18 ‰, +0.21 ‰, and +0.26 ‰ at 1 GPa and 1073, 973, and
651 873 K, respectively. Although the measured isotope fractionation factors are consistent
652 with our calculations within uncertainties at 973 and 873 K, the experimental result at
653 1073 K is slightly lower than our results (Fig. 10a). The measured $\Delta^{26}Mg_{forsterite\text{-}magnesite}$
654 is significantly lower than the calculated results based on the static GGA method
655 ($10^3ln\alpha_{forsterite\text{-}magnesite}$ = +0.30 ‰ at 1073 K) (Schauble, 2011), probably because the
656 static method does not take into account the pressure effect (see methods). On the other
657 hand, the measured $\Delta^{26}Mg_{forsterite\text{-}magnesite}$ at different temperatures does not follow a
658 proportional relationship with $1/T^2$ (Fig. 10a). In particular, Tang et al. (2021) derived
659 a negative $10^3ln\alpha_{forsterite\text{-}magnesite}$ from the $10^3ln\beta$ in our previous studies (Huang et al.,
660 2013; W. Wang et al., 2017a; Wu et al., 2015), which is contrast to the experimental
661 fractionation direction. However, it should be noted that the temperature- and pressure-
662 dependent $10^3ln\beta$ of minerals in Huang et al. (2013) and Wu et al. (2015) were
663 calculated based on the LDA+QHA method, while the $10^3ln\beta$ of magnesite in Wang et
664 al. (2017a) was calculated based on the static LDA method. The $10^3ln\beta$ values derived
665 from these two different methods cannot be directly compared with each other or used
666 to obtain the $10^3ln\alpha$ values, although those studies used the same details for the DFT
667 calculations (Huang et al., 2013; W. Wang et al., 2017a; Wu et al., 2015).
668 The measured $\Delta^{26}Mg_{spinel\text{-}magnesite}$ for $MgAl_2O_4$ is +0.90 ± 0.28 ‰, +1.10 ± 0.27 ‰,
669 and +1.73 ± 0.38 ‰ at 1 GPa and 1073 K, 973 K, and 873 K, respectively, consistent
670 with our calculations ($10^3ln\alpha_{MgAl2O4\text{-}magnesite}$ = +1.01 ‰ at 1073 K, +1.22 ‰ at 973 K,

and +1.51 ‰ at 873 K) within uncertainties (Fig. 10b). Notably, the experimentally determined $\Delta^{26}Mg_{spinel\text{-}magnesite}$ and the calculated $10^3ln\alpha_{spinel\text{-}magnesite}$ both decrease with Cr concentration (Cr/(Cr+Al) ratio) in spinel, because the substitution of Cr for Al increases the average Mg-O bond length and hence decreases the <F> of Mg (Table 2). The experimentally determined $\Delta^{26}Mg_{MgAlCrO4\text{-}magnesite}$ is +0.76 ± 0.37 ‰ at 1073 K, 0.95 ± 0.62 ‰ at 973 K, and 1.37 ± 0.37 ‰ at 873 K, while the $\Delta^{26}Mg_{MgCr2O4\text{-}magnesite}$ decreases to +0.47 ± 0.08 ‰ at 1073 K, +0.54 ± 0.22 ‰ at 973 K, and +0.90 ± 0.30 ‰ at 873 K (Tang et al., 2021). These results also agree with our predictions ($10^3ln\alpha_{MgAlCrO4\text{-}magnesite}$ = +0.71 ‰ at 1073 K, +0.86 ‰ at 973 K, and +1.06 ‰ at 873 K; $10^3ln\alpha_{MgCr2O4\text{-}magnesite}$ = +0.61 ‰ at 1073 K, +0.73 ‰ at 973 K, and +0.89 ‰ at 873 K) within experimental uncertainties (Fig. 10b and Table 4). Our results also show a nonlinear dependance of $10^3ln\alpha_{spinel\text{-}magnesite}$ on the Cr/(Cr+Al) ratio in spinel, with a $10^3ln\beta$ difference of 0.30 ‰ between $MgAl_2O_4$ and $MgAlCrO_4$ but a much smaller difference (0.10 ‰) between $MgAlCrO_4$ and $MgCr_2O_4$ at 1073 K. This is because the average Mg-O bond length and the <F> of Mg also nonlinearly depend on the Cr/(Cr+Al) ratio in spinel (Table 2). In contrast, the experimental data show a relatively smaller difference between $\Delta^{26}Mg_{MgAl2O4\text{-}magnesite}$ and $\Delta^{26}Mg_{MgAlCrO4\text{-}magnesite}$ than that between $\Delta^{26}Mg_{MgAlCrO4\text{-}magnesite}$ and $\Delta^{26}Mg_{MgCr2O4\text{-}magnesite}$ (Fig. 10b). This discrepancy between our calculations and previous experiments is probably due to the large experimental uncertainties that preclude the robust estimate of the Cr concentration effect on the $\Delta^{26}Mg_{spinel\text{-}magnesite}$. The $\Delta^{26}Mg_{spinel\text{-}forsterite}$ is derived from the $\Delta^{26}Mg_{forsterite\text{-}magnesite}$ and $\Delta^{26}Mg_{spinel\text{-}magnesite}$ and compared with our results in Fig. 10c. The experimentally determined $\Delta^{26}Mg_{MgAl2O4\text{-}forsterite}$ and $\Delta^{26}Mg_{MgCr2O4\text{-}forsterite}$ agree well with our predictions within experimental uncertainties.

5. Equilibrium or disequilibrium inter-mineral Mg isotope fractionation in natural rocks?

Previous studies have measured the Mg isotope compositions of constituent

699 minerals in a variety of mantle xenoliths, including olivine, pyroxenes, garnet, spinel,
700 and other minerals, and reported resolvable inter-mineral Mg isotope fractionation
701 (Chen et al., 2018; Handler et al., 2009; Hu et al., 2020; Yan Hu et al., 2016; Liu et al.,
702 2011; Stracke et al., 2018; Wang et al., 2015, 2012; Xiao et al., 2016, 2013; Young et
703 al., 2009). In particular, some studies found that spinel has higher $\delta^{26}Mg$ values relative
704 to those of coexisting olivine (Liu et al., 2011; Stracke et al., 2018; Xiao et al., 2013;
705 Young et al., 2009), whereas garnet exhibits lower $^{26}Mg/^{24}Mg$ ratios when compared to
706 coexisting clinopyroxene or olivine (Yan Hu et al., 2016; Wang et al., 2015, 2012). The
707 degree to which the observed inter-mineral fractionation in natural samples represents
708 equilibrium warrants examination.
709
710 **5.1 Pyroxenes vs. olivine**
711 Fig. 11 shows the measured Mg isotope fractionation between orthopyroxene and
712 olivine ($\Delta^{26}Mg_{orthopyroxene\text{-}olivine}$) and between clinopyroxene and olivine
713 ($\Delta^{26}Mg_{clinopyroxene\text{-}olivine}$) in natural rocks (Chen et al., 2018; Handler et al., 2009; Yan Hu
714 et al., 2016; Huang et al., 2011b; Liu et al., 2011; Stracke et al., 2018; Xiao et al., 2013;
715 Young et al., 2009) compared with the calculated results in this study. In general, these
716 studies found that the $\delta^{26}Mg$ values of orthopyroxene in most natural samples are
717 comparable to or relatively higher than those of coexisting olivine, with $\Delta^{26}Mg_{opx\text{-}ol}$
718 ranging from -0.05 ± 0.14 ‰ to 0.25 ± 0.14 ‰ (2SD), except for one of mantle
719 pyroxenite xenoliths (-0.32 ± 0.08 ‰) in Yan Hu et al. (2016) (Fig. 11). The
720 temperatures for these peridotites, pyroxenites, xenoliths, and layered mafic intrusions
721 were estimated to be approximately 1000-1500 K (Yan Hu et al., 2016; Huang et al.,
722 2011b; Liu et al., 2011; Stracke et al., 2018; Xiao et al., 2013; Zhang et al., 2012). For
723 comparison, at 0 GPa, our calculated $10^3\ln\alpha_{orthopyroxene\text{-}forsterite}$ ranges from +0.14 ‰ at
724 1000 K to +0.06 ‰ at 1500 K (Table 4 and Fig. 8). The pressure effect on
725 $10^3\ln\alpha_{orthopyroxene\text{-}forsterite}$ is insignificant at high temperatures, although the equilibrium
726 pressures of some garnet-bearing xenoliths are 1.5-2.0 GPa (Yan Hu et al., 2016).

Therefore, most of the observed $\Delta^{26}Mg_{opx\text{-}ol}$ in literature studies are consistent with the calculated $10^3ln\alpha_{orthopyroxene\text{-}forsterite}$ within uncertainties, indicating a general Mg isotopic equilibrium between orthopyroxene and olivine.

The $\Delta^{26}Mg_{clinopyroxene\text{-}olivine}$ observed in natural rocks vary in a wide range from -0.25 ± 0.07 ‰ in Yan Hu et al. (2016) to +0.42 ± 0.14 ‰ in Young et al. (2009). At 0 GPa, the $10^3ln\alpha_{diopside\text{-}forsterite}$ decreases from +0.17 ‰ at 1000 K to +0.08 ‰ at 1500 K (Table 4). Pressure can slightly enhance the magnitude of $10^3ln\alpha_{diopside\text{-}forsterite}$; at 1000 K, it increases from +0.17 ‰ at 0 GPa to +0.23 ‰ at 5 GPa. Most observed $\Delta^{26}Mg_{cpx\text{-}ol}$ data agree with the calculated $10^3ln\alpha_{diopside\text{-}forsterite}$ within uncertainties, reflecting Mg isotopic equilibrium between clinopyroxene and olivine. However, some published data from Young et al. (2009), Yan Hu et al. (2016), and Chen et al. (2018) fall outside the range of $10^3ln\alpha_{diopside\text{-}forsterite}$ (Fig. 11). Specifically, the observed $\Delta^{26}Mg_{cpx\text{-}ol}$ for San Carlos xenoliths in Young et al. (2009) is positive but larger than the calculated $10^3ln\alpha_{diopside\text{-}forsterite}$, whereas some data for Hannuoba pyroxenite xenoliths in Yan Hu et al. (2016) and Baima layered mafic intrusions in Chen et al. (2018) are negative, opposite to the direction of equilibrium fractionation. This implies that in some cases clinopyroxene and olivine are apparently not in Mg isotopic equilibrium, which may be the result of rapid and incomplete metasomatic reaction (Yan Hu et al., 2016) or chemical diffusion (Chen et al., 2018). Also, Macris et al. (2015) found Fe isotope disequilibrium in San Carlos xenoliths, which probably had experienced a complex petrologic history.

5.2 ilmenite vs. olivine/clinopyroxene

The isotopic disequilibrium between cumulus minerals in the Baima layered mafic intrusions was indicated by the measured ilmenite-olivine and ilmenite-clinopyroxene Mg isotope fractionation ($\Delta^{26}Mg_{ilmenite\text{-}olivine}$ and $\Delta^{26}Mg_{ilmenite\text{-}clinopyroxene}$) (Fig. 12). Chen et al. (2018) found that olivine and clinopyroxene have limited Mg isotope variations, with $\delta^{26}Mg$ ranging from -0.33 ± 0.05 ‰ to +0.05 ± 0.05 ‰ (2SD) for olivines and

from -0.29 ± 0.03 ‰ to -0.13 ± 0.04 ‰ for clinopyroxenes, similar to those of mantle xenoliths (Yan Hu et al., 2016; Huang et al., 2011b; Liu et al., 2011; Stracke et al., 2018; Xiao et al., 2013). In contrast, ilmenites display an extremely large Mg isotopic variation, with $\delta^{26}Mg$ ranging from -0.50 ± 0.05 ‰ to +1.90 ± 0.06 ‰ (2SD). As such, there is large inter-mineral Mg isotope fractionation between ilmenite and olivine and between ilmenite and clinopyroxene, with $\Delta^{26}Mg_{ilmenite\text{-}olivine}$ ranging from -0.22 ± 0.08 ‰ to +2.11 ± 0.09 ‰ (2SD) and $\Delta^{26}Mg_{ilmenite\text{-}clinopyroxene}$ from -0.30 ± 0.08 ‰ to +2.12 ± 0.07 ‰ (2SD). Our results show that ilmenite should be enriched in light Mg isotopes relative to forsterite and diopside at equilibrium (Fig. 8). When temperature increases from 1000 K to 1500 K at 0 GPa, $10^3ln\alpha_{ilmenite\text{-}forsterite}$ and $10^3ln\alpha_{ilmenite\text{-}diopside}$ range from -0.20 ‰ to -0.09 ‰ and from -0.37 ‰ to -0.16 ‰, respectively (Table 4). Although the MgO content in ilmenites varies from 1 to 4 wt% (Chen et al., 2018), the Mg concentration effects on the $10^3ln\alpha_{ilmenite\text{-}forsterite}$ and $10^3ln\alpha_{ilmenite\text{-}diopside}$ are negligible (< 0.04 ‰) (Table 4). The fractionation magnitudes can be enhanced by pressure. At 1000 K, the magnitude of $10^3ln\alpha_{ilmenite\text{-}forsterite}$ and $10^3ln\alpha_{ilmenite\text{-}diopside}$ increase by 0.06 ‰ and 0.11 ‰, respectively, when pressure increases from 0 to 5 GPa. Comparison of observed $\Delta^{26}Mg_{ilmenite\text{-}olivine}$ and $\Delta^{26}Mg_{ilmenite\text{-}clinopyroxene}$ with our results indicates disequilibrium Mg isotopic partitioning between most ilmenite and olivine/clinopyroxene pairs in layered mafic intrusions from SW, China (Fig. 12).

The isotopic disequilibrium between ilmenite and coexisting olivine/clinopyroxene in the Baima layered mafic intrusions is probably related to the kinetic fractionation caused by chemical diffusion (Chen et al., 2018). Previous experiments show that the MgO content in ilmenite decreases with temperature during crystallization (Toplis and Carroll, 1995). If ilmenite crystallized at high temperatures undergoes re-equilibration with surrounding silicate minerals (e.g., olivine and clinopyroxene) at relatively low temperatures, MgO would diffuse out of ilmenite and into olivine and clinopyroxene. This chemical exchange is further supported by the decreasing of MgO content from the core to the rim in most ilmenites in contact with

olivine and clinopyroxene (Chen et al., 2018). Given that light isotopes diffuse faster than heavy isotopes, the chemical diffusion would enrich ilmenites with heavy Mg isotopes and result in a negative correlation between Mg isotopes and MgO content, consistent with the observations (Chen et al., 2018). The chemical diffusion between ilmenites and ferromagnesian silicates in the Baima layered mafic intrusions at subsolidus temperatures has been also revealed by previous Fe isotopic evidence (Chen et al., 2014).

5.3 Garnet vs. olivine/pyroxenes

Several studies have measured the $\delta^{26}Mg$ of garnet and coexisting minerals in different samples and suggested various inter-mineral Mg isotope fractionation. Wang et al. (2012) and Wang et al. (2015) measured the $\delta^{26}Mg$ of garnet and clinopyroxene in cratonic eclogites from Kaalvallei and Bellsbank kimberlite, South Africa, and from Koidu kimberlite, West Africa. They found that the measured clinopyroxene-garnet Mg isotope fractionation ($\Delta^{26}Mg_{clinopyroxene\text{-}garnet}$) ranges from +0.38 ± 0.07 ‰ to +0.68 ± 0.08 ‰ for Kaalvallei and Bellsbank eclogites and from +0.43 ± 0.10 ‰ to +0.85 ± 0.10 ‰ for Koidu eclogites. The equilibrium temperatures estimated using the garnet-clinopyroxene Fe-Mg geothermometer are 1120-1670 K for these cratonic eclogites (Hills and Haggerty, 1989; Williams et al., 2009) and the pressures of equilibration are ~5 GPa (Hills and Haggerty, 1989; Huang et al., 2013). Li et al. (2011) also measured the $\delta^{26}Mg$ of garnet and omphacite in Bixiling eclogites and found large omphacite-garnet Mg isotope fractionation ($\Delta^{26}Mg_{omphacite\text{-}garnet}$ = +1.14 ± 0.04 ‰). The equilibrium temperatures estimated from the garnet-clinopyroxene Fe-Mg geothermometer are 814-997 K and the pressures of equilibration are ~3 GPa (Li et al., 2011). Stracke et al. (2018) analyzed the $\delta^{26}Mg$ values of clinopyroxene and coexisting garnet in Hawaiian garnet pyroxenites, which are interpreted as high-pressure (2-3 GPa) cumulates from melts erupted during the rejuvenated phase of volcanism (Bizimis et al., 2005). The measured $\Delta^{26}Mg_{clinopyroxene\text{-}garnet}$ ranges from +0.38 ± 0.14 ‰ to +0.46 ±

0.14 ‰, with the equilibrium temperatures estimated based on the Fe-Mg geothermometer varying from 1430 K to 1680 K (Bizimis et al., 2005). Yan Hu et al. (2016) reported the $\delta^{26}Mg$ of garnet, clinopyroxene, orthopyroxene, and olivine in garnet-bearing pyroxenites from Hannuoba, North China Craton, with $\Delta^{26}Mg_{clinopyroxene\text{-}garnet}$, $\Delta^{26}Mg_{orthopyroxene\text{-}garnet}$, and $\Delta^{26}Mg_{olivine\text{-}garnet}$ varying from +0.11 ± 0.06 ‰ to +0.65 ± 0.07 ‰, from +0.19 ± 0.06 ‰ to +0.76 ± 0.07 ‰, and from +0.16 ± 0.07 ‰ to +0.80 ± 0.07 ‰, respectively. For most garnet-bearing xenoliths, the temperatures and pressures of equilibration estimated based on equilibrium partitioning of Mg-Fe among clinopyroxene, orthopyroxene, and olivine are 1170-1310 K and 1.5-2.0 GPa (Yan Hu et al., 2016), respectively.

Our results show that at 0 GPa, the $10^3ln\alpha_{diopside\text{-}pyrope}$ ranges from +1.05 ‰ at 1000 K to +0.46 ‰ at 1500 K (Table 4). The magnitude of $10^3ln\alpha_{diopside\text{-}pyrope}$ is significantly enhanced by pressure. At 5 GPa, it increases to +1.26 ‰ at 1000 K and +0.55 ‰ at 1500 K. The observed $\Delta^{26}Mg_{clinopyroxene\text{-}garnet}$ values in cratonic eclogites and Hawaiian pyroxenites fall within the range of the calculated $10^3ln\alpha_{diopside\text{-}pyrope}$ (Fig. 13). For most data, the equilibrium temperatures estimated based on Mg isotopes are consistent with the values based on garnet-clinopyroxene Mg-Fe geothermometer, with a difference of < 100 K (Fig. 14). It should be noted that an uncertainty of ±0.14‰ on $\Delta^{26}Mg_{clinopyroxene\text{-}garnet}$ lead to an uncertainty in temperature of 100-200 K at 1200-1400 K. This suggests a general isotopic equilibrium between clinopyroxene and garnet in cratonic eclogites. For Bixiling eclogites, the $\Delta^{26}Mg_{omphacite\text{-}garnet}$ values of +1.14 ± 0.04 ‰ (Li et al., 2011) suggest an equilibrium temperature of ~1015 K based on the temperature dependence of $10^3ln\alpha_{diopside\text{-}pyrope}$ at 3 GPa. This value is slightly higher than the temperature range (822-887 K) estimated from garnet-clinopyroxene Mg-Fe geothermometer, but well consistent with the results of fresh eclogites (991-1030 K) reported (Xiao et al., 2000).

However, the observed $\Delta^{26}Mg_{clinopyroxene\text{-}garnet}$, $\Delta^{26}Mg_{orthopyroxene\text{-}garnet}$, and $\Delta^{26}Mg_{olivine\text{-}garnet}$ values in garnet-bearing lherzolites and pyroxenites from Yan Hu et al. (2016) are systematically lower than the calculated $10^3ln\alpha_{diopside\text{-}pyrope}$, $10^3ln\alpha_{orthopyroxene\text{-}}$

839 $_{pyrope}$, and $10^3\ln\alpha_{forsterite\text{-}pyrope}$, respectively, using the temperatures estimated based on
840 inter-mineral Mg-Fe geothermometer (Fig. 13). If the Mg isotopic partitioning reached
841 equilibrium between garnet and other silicate minerals, the temperatures estimated from
842 Mg isotope fractionation would be much higher than 1600 K (Fig. 14). Such high
843 temperatures seem unrealistic for Hannuoba mantle xenoliths and indicate that these
844 garnets are probably not in Mg isotopic equilibrium with coexisting pyroxenes and
845 olivine. The disequilibrium inter-mineral fractionation is likely caused by incomplete
846 melt-rock interaction that generated the garnets in lherzolites and
847 pyroxenites. Petrographic observations also reveal a clear metasomatic origin for these
848 garnets (Yan Hu et al., 2016), which were not the primary refractory phase in depleted
849 peridotites. Since garnets formed at the expense of coexisting minerals (e.g., spinel)
850 and partly inherited their heavy δ^{26}Mg values, the magnitude of inter-mineral Mg
851 isotope fractionation between garnet and coexisting minerals is smaller than that of
852 equilibrium fractionation (Yan Hu et al., 2016).
853
854 **5.4 Spinel vs. olivine**
855 Previous studies investigated the Mg isotope fractionation between spinel and
856 olivine ($\Delta^{26}Mg_{spinel\text{-}olivine}$) in natural peridotites and xenoliths (Liu et al., 2011; Stracke
857 et al., 2018; Xiao et al., 2013; Young et al., 2009), and found that spinel has higher
858 δ^{26}Mg values than coexisting olivine. The $\Delta^{26}Mg_{spinel\text{-}olivine}$ ranges from +0.17 ± 0.14 ‰
859 for north China craton peridotites in Xiao et al. (2013) to +0.87 ± 0.14 ‰ for San Carlos
860 xenoliths in Young et al. (2009) (Fig. 15). The estimated temperatures for these
861 peridotites and xenoliths are 1100-1500 K based on the clinopyroxene-orthopyroxene
862 Mg-Fe geothermometer (Liu et al., 2011; Stracke et al., 2018; Xiao et al., 2013) or
863 inversion parameter for Al-Mg ordering in spinel (Young et al., 2009). Our results also
864 show that spinel is enriched in heavy Mg isotopes relative to forsterite (Table 4 and Fig.
865 8). The $10^3\ln\alpha_{spinel\text{-}forsterite}$ is not only controlled by temperature but also affected by the
866 Cr# in spinel. In contrast, the fractionation magnitude is not significantly affected by

pressure (Fig. 8). When temperature increases from 1100 K to 1500 K, the $10^3\ln\alpha_{spinel\text{-}forsterite}$ decreases from +0.80 ‰ to +0.43 ‰ for $MgAl_2O_4$ and from +0.52 ‰ to +0.28 ‰ for $MgAlCrO_4$ (Fig. 8). The Cr# in spinel from these studies is lower than 0.5 (summarized in Stracke et al., 2018), and thus the observed $\Delta^{26}Mg_{spinel\text{-}olivine}$ values are expected to fall between the $10^3\ln\alpha_{spinel\text{-}forsterite}$ lines for $MgAl_2O_4$ and $MgAlCrO_4$.

The $\Delta^{26}Mg_{spinel\text{-}olivine}$ data from Young et al. (2009) fall on the calculated $10^3\ln\alpha_{spinel\text{-}forsterite}$ line for $MgAl_2O_4$ within uncertainties if the temperatures estimated based on the inversion parameter for Mg-Al ordering are adopted (Fig. 15), but these San Carlos spinels have Cr#s of ~ 0.38 (Young et al., 2009). This suggests an average equilibrium temperature of 960 ± 100 K (2SD) based on the temperature dependence of $10^3\ln\alpha_{spinel\text{-}forsterite}$ at Cr# ~ 0.38, which is consistent with the spinel inversion parameter closure temperature of 1080 ± 37 K (Uchida, 2005) but somewhat lower than the one estimated by Young et al. (2009) using the first-principles results in Schauble (2011). This is because the $10^3\ln\alpha_{spinel\text{-}forsterite}$ for $MgAl_2O_4$ was used and the effect of Cr# was ignored in Young et al. (2009). However, if the temperatures estimated from the clinopyroxene-orthopyroxene Mg-Fe geothermometer are used, the observed $\Delta^{26}Mg_{spinel\text{-}olivine}$ data from Liu et al. (2011), Xiao et al. (2013), and Stracke et al. (2018) with Cr# of 0-0.3 fall around or below the $10^3\ln\alpha_{spinel\text{-}forsterite}$ line for $MgAlCrO_4$, somewhat deviating from the expected results at Cr# ~ 0-0.3 (Fig. 15). To show the Cr# effect on the Mg isotope fractionation, we anchored the observed $\Delta^{26}Mg_{spinel\text{-}olivine}$ to the fractionation at 1000 K using $A_{spinel\text{-}olivine} = (\Delta^{26}Mg_{spinel\text{-}olivine})*T^2/10^6$, where T is temperature. In general, the $A_{spinel\text{-}olivine}$ estimated from $\Delta^{26}Mg_{spinel\text{-}olivine}$ show a decreasing trend with Cr#, consistent with our predicted results (Fig. 15b). Nonetheless, the magnitude is systematically smaller than our results, probably due to the Mg-Al substitution in spinel and/or reflecting the equilibrium temperature differences between Mg isotope exchange and Mg-Fe exchange if Mg isotopic equilibrium in natural samples had reached.

First, previous experiments found significant Mg-Al exchange in spinel at high

temperatures (e.g., Ma and Liu, 2019; Peterson et al., 1991), which may affect the equilibrium Mg isotope fractionation between spinel and other minerals. In a normal configuration for $MgAl_2O_4$ spinel, Mg^{2+} only occupies the tetrahedral sites with a CN of 4 for Mg-O bonds, while Al^{3+} only occupies the octahedral sites with a CN of 6 for Al-O bonds. At high temperatures, a fraction of Mg could occupy the octahedral sites to form a disordered $(Mg_{1-x}Al_x)(Mg_xAl_{2-x})O_4$ spinel, with x increasing from ~0.2 at 1000 K to ~0.3 at 1400 K (Ma and Liu, 2019). To check the effect of Mg-Al disorder effect on $10^3ln\alpha_{spinel\text{-}forsterite}$, we conducted first-principles calculations on $(Mg_7Al)(MgAl_{15})O_{32}$ spinel based on the LDA+QHA, corresponding to a value of 0.125 for x. The calculated results show that this disordered spinel has a slightly longer average Mg-O bond length for the tetrahedral Mg than the normal spinel, which, however, are both much shorter than the average Mg-O bond length for the octahedral six-fold Mg (Table 2). The $(Mg_7Al)(MgAl_{15})O_{32}$ spinel has an average <F> of Mg of 247.5 N/m, which is ~3 N/m lower than that of $MgAl_2O_4$ spinel (Table 2). Therefore, its $10^3ln\beta$ value decreases by ~0.04 ‰ at 1000 K compared with a normal spinel (Tables 3 and 4), and the $10^3ln\alpha$ between $(Mg_7Al)(MgAl_{15})O_{32}$ spinel and forsterite is ~0.04 ‰ lower than that between $MgAl_2O_4$ spinel and forsterite at 1000 K. If the difference is linearly correlated with the concentration of Mg in the octahedral site, one can infer that the $10^3ln\alpha_{spinel\text{-}forsterite}$ will decrease by ~0.08 ‰ at 1000 K when 25 mol% of Mg in spinel occupy the octahedral sites (Ma and Liu, 2019). Such a magnitude is smaller than the difference between our results and the observations from natural samples (Fig. 15b), and therefore, the Mg-Al disordered effect can only partly account for that discrepancy.

Second, the deviation of the other $\Delta^{26}Mg_{spinel\text{-}ol}$ data from our results may be caused by the differences in the closure temperatures of inter-mineral Mg isotopic equilibrium and inter-mineral cation equilibrium as suggested by Stracke et al. (2018) and Tang et al. (2021). It was proposed that the temperatures for xenoliths from north China craton could vary from 800 to 1500 K using different cation geothermometers (Wu et al., 2006), indicating that there are considerable temperature uncertainties for

reconciling the $\Delta^{26}Mg_{spinel\text{-}ol}$ data and the $10^3ln\alpha_{spinel\text{-}forsterite}$. If the $\Delta^{26}Mg_{spinel\text{-}ol}$ data from Liu et al. (2011), Xiao et al. (2013), and Stracke et al. (2018) reflect equilibrium fractionation, the temperatures estimated based on the temperature dependances of $10^3ln\alpha_{spinel\text{-}forsterite}$ at various Cr# are significantly higher than those from inter-mineral element geothermometers (Fig. 16), although the errors for temperatures from Mg isotopes could be up to ±400 K (2SD) due to the large uncertainties of $\Delta^{26}Mg_{spinel\text{-}ol}$ (±0.14 ‰, 2SD). The Mg isotope temperatures for most data are lower than 1500 K, with differences of < 300 K between Mg isotope and element geothermometers (Fig. 16). However, some samples require an extremely high temperatures for Mg isotopic equilibration due to the very small $\Delta^{26}Mg_{spinel\text{-}olivine}$ (Fig. 15), which are unrealistic for mantle xenoliths. In summary, the temperature difference between Mg isotope equilibrium and cation equilibrium probably could explain the deviation of some of $\Delta^{26}Mg_{spinel\text{-}olivine}$ data from our results.

Finally, the observed $\Delta^{26}Mg_{spinel\text{-}olivine}$ values may reflect the Mg isotopic disequilibrium induced by metasomatism (Liu et al., 2011; Stracke et al., 2018; Xiao et al., 2013). Most peridotites and xenoliths analyzed for Mg isotope ratios have experienced considerable post-melting metasomatism (Stracke et al., 2018). The only likely xenoliths that may undergo a simple petrogenetic history are peridotites from the North China Craton investigated by Liu et al. (2011), because these rocks preserve the expected correlation between Al_2O_3 (whole rock) or Cr# in spinel and Mg# in olivine. However, the rare earth element patterns in these peridotites also show variable metasomatic overprint (Wu et al., 2006). All other peridotite suites likely have experienced considerable metasomatism (Liu et al., 2011; Stracke et al., 2018; Xiao et al., 2013; Young et al., 2009). The melt-peridotite reaction gradually dissolves pyroxenes (clinopyroxene first) and forms olivine, spinel, and a modified melt. The later-formed spinel may have partly inherited the relatively light $\delta^{26}Mg$ values of pyroxenes, making the observed $\Delta^{26}Mg_{spinel\text{-}olivine}$ values lower than the equilibrium fractionation. The degree to which the observed $\Delta^{26}Mg_{spinel\text{-}olivine}$ have been overprinted

by post-melting metasomatism may vary in different samples. For instance, the equilibrium Mg isotope temperatures for peridotites in Liu et al. (2011) are ~200 K higher than those from the clinopyroxene-orthopyroxene Fe-Mg geothermometer, comparable to the uncertainties introduced by isotopic measurement uncertainty (Fig. 16). This indicates that spinel and olivine are nearly in Mg isotopic equilibrium in these peridotites that have probably not experienced strong metasomatism, supported by the correlation between Al_2O_3 (whole rock) or Cr# in spinel and Mg# in olivine (Liu et al., 2011). In contrast, the observed $\Delta^{26}Mg_{spinel\text{-}olivine}$ for Hawaiian peridotites in Stracke et al. (2018) are too small (~ +0.22 ‰) (Fig. 15), and therefore, the equilibrium temperatures estimated based on Mg isotopes are ~600 K higher than those from inter-mineral cation geothermometers (Fig. 16). These large differences likely reflect the Mg isotopic disequilibrium between spinel and coexisting olivine due to the considerable post-melting metasomatism (Stracke et al., 2018).

5.5. Mg isotope geothermometers

Comparison of the observed inter-mineral Mg isotope fractionation in mantle rocks reveals disequilibrium Mg isotope partitioning among some minerals, while some rocks likely preserve the equilibrium inter-mineral Mg isotope fractionation. The large $10^3\ln\alpha_{forsterite\text{-}pyrope}$, $10^3\ln\alpha_{clinopyroxene\text{-}pyrope}$, and $10^3\ln\alpha_{spinel\text{-}forsterite}$ at high temperatures suggest that the measured Mg isotope fractionation between these mineral pairs, if reflecting the equilibrium fractionation, could be used to estimate the equilibrium temperatures, when the equilibrium pressure can be obtained by other methods. The application of $10^3\ln\alpha_{spinel\text{-}forsterite}$ requires the knowledge of chemical composition in spinel, e.g., the Cr# and the Mg-Al disorder, because $10^3\ln\alpha_{spinel\text{-}forsterite}$ is not only controlled by temperature but also significantly affected by the Cr# (Fig. 10). In general, the temperatures of equilibration for mantle rocks were estimated using the inter-mineral cation geothermometers, e.g., the clinopyroxene-orthopyroxene and garnet-clinopyroxene Mg-Fe geothermometers, but the temperatures from different cation

geothermometers could vary in a wide range with differences of up to 300 K (Bizimis et al., 2005; Wu et al., 2006). The Mg isotope geothermometers can provide independent temperature estimates and check the reliability of temperatures from the inter-mineral cation geothermometers. For instance, most $\Delta^{26}Mg_{cpx\text{-}grt}$ values from cratonic eclogites and Hawaiian pyroxenites in Wang et al. (2012), Wang et al. (2015), and Stracke et al. (2018) reflect the equilibrium fractionation and the temperatures given by clinopyroxene-garnet Mg isotope geothermometer agree well with those from the garnet-clinopyroxene Mg-Fe geothermometer within 100 K (Fig. 14). However, for Bixiling eclogites in Li et al. (2011), the equilibrium temperature range estimated from garnet-clinopyroxene Mg-Fe geothermometer is 822-887 K, lower than the equilibrium temperature of ~1015 K from clinopyroxene-garnet Mg isotope geothermometer based on the $\Delta^{26}Mg_{omphacite\text{-}grt}$ values of +1.14 ± 0.04 ‰. It should be noted that the precision of Mg isotope geothermometers could be better than that of the traditional inter-mineral cation geothermometers. The uncertainties of ±0.10 ‰ on $\Delta^{26}Mg_{cpx\text{-}grt}$ and $\Delta^{26}M_{spinel\text{-}ol}$ translate into errors in temperature of ~70 and ~90 K at T ~ 1200 K, respectively. Therefore, Mg isotope geothermometers could provide a reliable and independent tool in estimating equilibrium temperatures of garnet-bearing and spinel-bearing mantle rocks if the Mg isotope exchange has reached equilibrium.

6. Implications for Mg isotope fractionation during late-stage basalt differentiation

In order to constrain the Mg isotope fractionation during magma differentiation, previous studies measured the $\delta^{26}Mg$ values of a set of well-characterized basalts from the Kilauea Iki lava lake, Hawaii, which have diverse chemical compositions (MgO content ranges from 2.4 to 26.9 wt%) as a result of magma differentiation (Teng et al., 2010a, 2007). They found no resolvable Mg isotopic variations among these basalt samples at the current levels of analytical precision, indicating no measurable Mg isotope fractionation during mineral crystallization. However, subsequent studies on a

suite of alkaline rocks show that samples containing > ~5 wt.% MgO have relatively uniform δ^{26}Mg values within uncertainties, whereas highly evolved rocks containing < ~5 wt.% MgO display large δ^{26}Mg variations (Wang et al., 2016, 2018; X.-J. Wang et al., 2021). This suggests that late-stage basalt differentiation may lead to detectable Mg isotope fractionation. As an example, we focus on the δ^{26}Mg variations in ocean island basalts (OIBs) from St. Helena Island investigated by X.-J. Wang et al. (2021). These OIBs vary from primitive nepheline-normative basalt to highly evolved trachyandesite with MgO contents decreasing from 15.7 wt.% to 0.8 wt.%, which include the crystallization history during late-stage differentiation. These samples have homogenous radiogenic isotopic compositions (Hanyu et al., 2014; Kawabata et al., 2011), implying that they may originate from a common mantle source and their parental magmas may have the same δ^{26}Mg.

X.-J. Wang et al. (2021) found that the basalts which only experienced crystallization of olivine and clinopyroxene have δ^{26}Mg values similar to that of the peridotitic mantle (δ^{26}Mg = -0.25 ± 0.04 ‰) within uncertainties, while three out of four highly evolved rocks with MgO content < 4 wt% have lower δ^{26}Mg values (-0.36 ± 0.04 ‰) than the mantle value. The chemical variations in the highly evolved samples with < 4 wt% MgO were caused by the crystallization of a variety of minerals including olivine, clinopyroxene, plagioclase, apatite, and magnetite (X.-J. Wang et al., 2021). Considering the low MgO contents in plagioclase and apatite (Kawabata et al., 2011; Luhr et al., 1984), the removal of these two phases does not significantly affect the δ^{26}Mg of the residual melt. On the other hand, the δ^{26}Mg values of highly evolved rocks with < 4 wt% MgO show a decreasing correlation with the decreasing of TiO_2 content, suggesting that magnetite likely plays an important role in producing the δ^{26}Mg variations in these samples (X.-J. Wang et al., 2021). To model the Mg isotope fractionation during mineral crystallization, X.-J. Wang et al. (2021) investigated the proportions and chemical compositions of segregated minerals and residual melts during St. Helena lavas differentiation using MELTS. Combining the Mg abundances

in different phases with the Mg isotope fractionation between olivine and melt ($\Delta^{26}Mg_{olivine\text{-}melt}$) and between clinopyroxene and melt ($\Delta^{26}Mg_{clinopyroxene\text{-}melt}$), which were assumed as -0.04 and -0.02 ‰, respectively, they suggested that an Mg isotope fractionation factor between magnetite and melt ($\Delta^{26}Mg_{magnetite\text{-}melt}$) of ~ +0.6 ‰ is required to explain the lower $\delta^{26}Mg$ values in highly evolved rocks. This is because magnetite has a low Mg content, and a large $\Delta^{26}Mg_{magnetite\text{-}melt}$ value is required to drive the $\delta^{26}Mg$ of the residual melt to a more negative value as $\Delta^{26}Mg_{olivine\text{-}melt}$ = -0.04 ‰ and $\Delta^{26}Mg_{clinopyroxene\text{-}melt}$ = -0.02 ‰.

Our calculated results show that magnetite (represented by magnesioferrite) is enriched in heavy Mg isotopes relative to olivine, with $10^3ln\alpha_{magnetite\text{-}forsterite}$ varying from +0.30 ‰ for the octahedral Mg (six-fold) to +0.10 ‰ for the tetrahedral Mg (four-fold) at 1000 K and 0 GPa (Table 4 and Fig. 8). Previous experiments suggested that Mg can occupy both the octahedral and tetrahedral sites in magnetite, and the fraction of tetrahedral Mg is ~ 25% at high temperatures (O'Neill et al., 1992). Thus, the $10^3ln\alpha_{magnetite\text{-}forsterite}$ can be calculated from the contribution from these two types of Mg, which is expressed as $10^3ln\alpha_{magnetite\text{-}forsterite} = 0.32*10^6/T^2\text{-}0.080*(10^6/T^2)^2$, T is the temperature in Kelvin. Given that there is no resolvable Mg isotope fractionation between olivine and melt, the crystallization of magnetite will enrich the residual melt in light Mg isotopes, consistent with the observations for St. Helena highly evolved rocks. However, the magnitude of $10^3ln\alpha_{magnetite\text{-}forsterite}$ or $10^3ln\alpha_{magnetite\text{-}melt}$ is much smaller than the required value ($\Delta^{26}Mg_{mgt\text{-}melt}$ = ~ +0.6 ‰) in X.-J. Wang et al. (2021). The discrepancy is probably related to the unjustified values for $\Delta^{26}Mg_{olivine\text{-}melt}$ and $\Delta^{26}Mg_{clinopyroxene\text{-}melt}$ used by X.-J. Wang et al. (2021). Here we combine chemical evolution history calculated by X.-J. Wang et al. (2021) using MELTS and the fractionation data ($10^3ln\alpha_{clinopyroxene\text{-}forsterite}$ and $10^3ln\alpha_{magnetite\text{-}forsterite}$) in this study to model the $\delta^{26}Mg$ evolution in the residual melt during St. Helena lava differentiation (Fig. 17). The $\Delta^{26}Mg_{olivine\text{-}melt}$ value is taken as 0.00 ± 0.04 ‰ as constrained by measurements on Kilauea Iki lavas (Teng et al., 2010a), and therefore, $\Delta^{26}Mg_{clinopyroxene\text{-}}$

$_{melt}$ and $\Delta^{26}Mg_{magnetite\text{-}melt}$ can be derived from the calculated $10^3ln\alpha_{clinopyroxne\text{-}forsterite}$ and $10^3ln\alpha_{magnetite\text{-}forsterite}$. The $\delta^{26}Mg$ value of primary melt is assumed as the peridotitic mantle value (-0.25 ± 0.04 ‰; Teng, 2017). Our model results show that the residual melts at MgO < 5 wt.% have relatively lower $\delta^{26}Mg$ values than the primary melt because clinopyroxene and magnetite are enriched in heavy Mg isotopes relative to the melt. Clinopyroxene and magnetite both play a key role in fractionating Mg isotopes during late-stage differentiation. The modeling results based on the fractionation data in this study can reproduce the negative $\delta^{26}Mg$ values observed in highly evolved basalts from St. Helena. The $\delta^{26}Mg$ of melt displays a wide range due to the uncertainties of $\Delta^{26}Mg_{olivine\text{-}melt}$ and $\delta^{26}Mg$ of primary melt. Overall, Mg isotopes could be significantly fractionated due to the fractional crystallization of some minerals such as magnetite and clinopyroxene during late-stage basalt differentiation.

A recent study reported a more negative $\Delta^{26}Mg_{olivine\text{-}melt}$ value of -0.071 ± 0.010 ‰ at ~1438 K by measuring the $\delta^{26}Mg$ of equilibrated olivine-glass pairs from ocean island and mid-ocean ridge basalts (Liu et al., 2022). The fractionation factor can be expressed as a function of temperature as $\Delta^{26}Mg_{olivine\text{-}melt} = (-0.146 \pm 0.026)\times10^6/T^2$ (‰). If this value is used, the $\Delta^{26}M_{clinopyroxene\text{-}melt}$ is negligible (~ +0.01 ‰) and the $\Delta^{26}Mg_{magnetite\text{-}melt}$ is only +0.08 ‰ at the crystallization temperature of magnetite. The modeling shows that the residual melt will gradually become enriched in heavy Mg isotopes with differentiation, contrary to the fractionation direction with a $\Delta^{26}Mg_{olivine\text{-}melt}$ value of 0.00 ± 0.04 ‰ (Fig. 17). This comparison highlights the importance of accurately determining the $\Delta^{26}Mg_{olivine\text{-}melt}$ by experiments or DFT calculations, especially when the chemical composition of melt changes. More future studies are needed to solve this key problem.

7. Conclusions

In this study, we compile previous first-principles results and new calculations based on DFT to present the $10^3ln\alpha$ among a variety of mantle minerals. The LDA and

GGA are generally adopted to model the exchange-correlation potential in the DFT calculations, and the static and QHA methods are used to calculate the $10^3\ln\beta$. We find that the volumes and average Mg-O bond lengths of mantle minerals predicted by the LDA calculations agree well with experimental results at ambient conditions, while the GGA calculations overestimate those structural properties. Both LDA and GGA calculations based on the periodic boundary conditions can predict the vibrational properties of mantle minerals well, and the LDA is better than the GGA. Due to the differences in predicted structural properties between the LDA and the GGA, the $10^3\ln\beta$ of mantle minerals from the static GGA calculations are smaller than the static LDA results. Therefore, the $10^3\ln\beta$ calculated based on different exchange-correlation potentials cannot be used to derive the $10^3\ln\alpha$. In general, both LDA and GGA predict similar inter-mineral $10^3\ln\alpha$ values at high temperatures because the systematic offsets of $10^3\ln\beta$ are canceled out.

We also compare the $10^3\ln\alpha$ values calculated by the static LDA method and the LDA+QHA method. The QHA method can derive the pressure- and temperature-dependent $10^3\ln\beta$ from its volume- and temperature-dependent form via the equation of states. The results show that the inter-mineral $10^3\ln\alpha$ values calculated from the static LDA method generally agree with those calculated from the LDA+QHA method at 0 GPa. If the pressure effect is ignored, it is more convenient and less computational expensive to use the static method to predict $10^3\ln\alpha$. Two sets of inter-mineral $10^3\ln\alpha$ values of $^{26}Mg/^{24}Mg$ calculated by the static LDA method and QHA+LDA method are provided in this work.

The theoretical results show that the $10^3\ln\beta$ of $^{24}Mg/^{26}Mg$ decreases in the order of spinel ($MgAl_2O_4$) > spinel ($MgAlCrO_4$) > ringwoodite > magnesiochromite ($MgCr_2O_4$) > wadsleyite > diopside ~ periclase > magnesioferrite ($^{T}MgFe_2O_4$) ~ magnesioferrite ($^{M}MgFe_2O_4$) ~ orthopyroxene > forsterite > bridgmanite > magnesite > geikielite ($MgTiO_3$) ~ geikielite ($MgFeTi_2O_6$) ~ geikielite ($Mg_2Fe_4Ti_6O_{18}$) > majorite > pyrope. The $10^3\ln\beta$ is dominantly controlled by the force constant of Mg in these

minerals, which is affected by structural properties such as the Mg-O bond lengths and the CNs. Inter-mineral $10^3\ln\alpha$ values could be significantly affected by pressure due to the large difference in the pressure slopes of $10^3\ln\beta$. The $\Delta^{26}Mg_{forsterite\text{-}magnesite}$, $\Delta^{26}Mg_{spinel\text{-}magnesite}$, and $\Delta^{26}Mg_{spinel\text{-}forsterite}$ measured by previous experiments using the three-isotope method are consistent with the calculated results within uncertainties. We further use the calculated data to examine the degree to which the observed inter-mineral Mg isotope fractionation in natural rocks represents equilibrium. We also model the Mg isotope fractionation during late-stage basalt differentiation and find that the fractional crystallization of some minerals such as magnetite and clinopyroxene during late-stage basalt differentiation may enrich the residual melt in light Mg isotopes.

Acknowledgements

W.W. acknowledges the support the support from CAS Hundred Talents Programme and from the UCL-Carnegie Postdoctoral Scholarship. Part of the calculations were conducted at the Supercomputing Center of the University of Science and Technology of China.

References

Ai, Y., Zheng, T., 2003. The upper mantle discontinuity structure beneath eastern China. Geophys. Res. Lett. 30, 2089. doi:10.1029/2003GL017678

Akaogi, M., Ito, E., Navrotsky, A., 1989. Olivine-modified spinel-spinel transitions in the system Mg 2 SiO 4 -Fe 2 SiO 4 : Calorimetric measurements, thermochemical calculation, and geophysical application. J. Geophys. Res. Solid Earth 94, 15671–15685. doi:10.1029/JB094iB11p15671

Angel, R.J., Finger, L.W., Hazen, R.M., Kanzaki, M., Weidner, D.J., Liebermann, R.C., Veblen, D.R., 1989. Structure and twinning of single-crystal MgSiO3 garnet synthesized at 17 GPa and 1800 °C. Am. Mineral. 74, 509–512.

Anisimov, V.I., Zaanen, J., Andersen, O.K., 1991. Band theory and Mott insulators: Hubbard U instead of Stoner I. Phys. Rev. B 44, 943–954. doi:10.1103/PhysRevB.44.943

Bigeleisen, J., Mayer, M.G., 1947. Calculation of Equilibrium Constants for Isotopic Exchange Reactions. J. Chem. Phys. 15, 261. doi:10.1063/1.1746492

Bina, C.R., Helffrich, G., 1994. Phase transition Clapeyron slopes and transition zone seismic discontinuity topography. J. Geophys. Res. 99, 15853. doi:10.1029/94JB00462

Bizimis, M., Sen, G., Salters, V.J.M., Keshav, S., 2005. Hf-Nd-Sr isotope systematics of garnet pyroxenites from Salt Lake Crater, Oahu, Hawaii: Evidence for a depleted component in Hawaiian volcanism. Geochim. Cosmochim. Acta 69, 2629–2646. doi:10.1016/j.gca.2005.01.005

Blanchard, M., Balan, E., Schauble, E.A., 2017. Equilibrium Fractionation of Non-traditional Isotopes: a Molecular Modeling Perspective. Rev. Mineral. Geochemistry 82, 27–63. doi:10.2138/rmg.2017.82.2

Brewer, A., Teng, F.-Z., Dethier, D., 2018. Magnesium isotope fractionation during granite weathering. Chem. Geol. 501, 95–103. doi:10.1016/j.chemgeo.2018.10.013

Cameron, M., Sueno, S., Prewitt, C.T., Papike, J.J., 1973. High-Temperature Crystal Chemistry of Acmite, Diopside, Hedenbergite Jadeite, Spodumene and Ureyite. Am. Mineral. 58, 594–618.

Chen, L.-M., Song, X.-Y., Zhu, X.-K., Zhang, X.-Q., Yu, S.-Y., Yi, J.-N., 2014. Iron isotope fractionation during crystallization and sub-solidus re-equilibration: Constraints from the Baima mafic layered intrusion, SW China. Chem. Geol. 380, 97–109. doi:10.1016/j.chemgeo.2014.04.020

Chen, L.-M., Teng, F.-Z., Song, X.-Y., Hu, R.-Z., Yu, S.-Y., Zhu, D., Kang, J., 2018. Magnesium isotopic evidence for chemical disequilibrium among cumulus minerals in layered mafic intrusion. Earth Planet. Sci. Lett. 487, 74–83. doi:10.1016/j.epsl.2018.01.036

Cococcioni, M., de Gironcoli, S., 2005. Linear response approach to the calculation of the effective interaction parameters in the LDA+U method. Phys. Rev. B 71, 035105. doi:10.1103/PhysRevB.71.035105

Cottaar, S., Deuss, A., 2016. Large-scale mantle discontinuity topography beneath Europe: Signature of akimotoite in subducting slabs. J. Geophys. Res. Solid Earth 121, 279–292. doi:10.1002/2015JB012452

Cuozzo, N., Sletten, R.S., Hu, Y., Liu, L., Teng, F.-Z., Hagedorn, B., 2020. Silicate weathering in antarctic ice-rich permafrost: Insights using magnesium isotopes. Geochim. Cosmochim. Acta 278, 244–260. doi:10.1016/j.gca.2019.07.031

Dauphas, N., Hu, M.Y., Baker, E.M., Hu, J., Tissot, F.L.H., Alp, E.E., Roskosz, M., Zhao, J., Bi, W., Liu, J., Lin, J.-F., Nie, N.X., Heard, A., 2018. SciPhon: a data analysis software for nuclear resonant inelastic X-ray scattering with applications to Fe, Kr, Sn, Eu and Dy. J. Synchrotron Radiat. 25, 1581–1599. doi:10.1107/S1600577518009487

Dauphas, N., Roskosz, M., Alp, E.E., Golden, D.C., Sio, C.K., Tissot, F.L.H., Hu, M.Y., Zhao, J., Gao, L., Morris, R.V., 2012. A general moment NRIXS approach to the determination of equilibrium Fe isotopic fractionation factors: Application to goethite and jarosite. Geochim. Cosmochim. Acta 94, 254–275. doi:10.1016/j.gca.2012.06.013

Dauphas, N., Roskosz, M., Alp, E.E., Neuville, D.R., Hu, M.Y., Sio, C.K., Tissot, F.L.H., Zhao, J., Tissandier, L., Médard, E., Cordier, C., 2014. Magma redox and structural controls on iron isotope variations in Earth's mantle and crust. Earth Planet. Sci. Lett. 398, 127–140. doi:10.1016/j.epsl.2014.04.033

Deuss, A., 2009. Global Observations of Mantle Discontinuities Using SS and PP Precursors. Surv. Geophys. 30, 301–326. doi:10.1007/s10712-009-9078-y

Deuss, A., 2006. The Nature of the 660-Kilometer Discontinuity in Earth's Mantle from Global Seismic Observations of PP Precursors. Science (80-.). 311, 198–201. doi:10.1126/science.1120020

Dewaele, A., Fiquet, G., Andrault, D., Hausermann, D., 2000. P-V-T equation of state of periclase from synchrotron radiation measurements. J. Geophys. Res. Solid Earth 105, 2869–2877. doi:10.1029/1999JB900364

Duan, L., Wang, W., Wu, Z., Qian, W., 2019. Thermodynamic and Elastic Properties of Grossular at High Pressures and High Temperatures: A First-Principles Study. J. Geophys. Res. Solid Earth 124, 7792–7805. doi:10.1029/2019JB017439

Ducher, M., Blanchard, M., Balan, E., 2018. Equilibrium isotopic fractionation between aqueous Zn and minerals from first-principles calculations. Chem. Geol. 1–9. doi:10.1016/j.chemgeo.2018.02.040

Dziewonski, A.M., Anderson, D.L., 1981. Preliminary reference Earth model. Phys. Earth Planet. Inter. 25, 297–356. doi:10.1016/0031-9201(81)90046-7

Fei, Y., Van Orman, J., Li, J., van Westrenen, W., Sanloup, C., Minarik, W., Hirose, K., Komabayashi, T., Walter, M., Funakoshi, K., 2004. Experimentally determined postspinel transformation boundary in Mg 2 SiO 4 using MgO as an internal pressure standard and its geophysical implications. J. Geophys. Res. Solid Earth 109, 1–8. doi:10.1029/2003JB002562

Feng, C., Qin, T., Huang, S., Wu, Z., Huang, F., 2014. First-principles investigations

of equilibrium calcium isotope fractionation between clinopyroxene and Ca-doped orthopyroxene. Geochim. Cosmochim. Acta 143, 132–142. doi:10.1016/j.gca.2014.06.002

Fujii, T., Moynier, F., Blichert-Toft, J., Albarède, F., 2014. Density functional theory estimation of isotope fractionation of Fe, Ni, Cu, and Zn among species relevant to geochemical and biological environments. Geochim. Cosmochim. Acta 140, 553–576. doi:10.1016/j.gca.2014.05.051

Fujii, T., Moynier, F., Pons, M.-L., Albarède, F., 2011. The origin of Zn isotope fractionation in sulfides. Geochim. Cosmochim. Acta 75, 7632–7643. doi:10.1016/j.gca.2011.09.036

Gao, C., Cao, X., Liu, Q., Yang, Y., Zhang, S., He, Y., Tang, M., Liu, Y., 2018. Theoretical calculation of equilibrium Mg isotope fractionations between minerals and aqueous solutions. Chem. Geol. #pagerange#. doi:10.1016/j.chemgeo.2018.04.005

Gao, Y., Suetsugu, D., Fukao, Y., Obayashi, M., Shi, Y., Liu, R., 2010. Seismic discontinuities in the mantle transition zone and at the top of the lower mantle beneath eastern China and Korea: Influence of the stagnant Pacific slab. Phys. Earth Planet. Inter. 183, 288–295. doi:10.1016/j.pepi.2010.03.009

Giannozzi, P., Baroni, S., Bonini, N., Calandra, M., Car, R., Cavazzoni, C., Ceresoli, D., Chiarotti, G.L., Cococcioni, M., Dabo, I., Dal Corso, A., de Gironcoli, S., Fabris, S., Fratesi, G., Gebauer, R., Gerstmann, U., Gougoussis, C., Kokalj, A., Lazzeri, M., Martin-Samos, L., Marzari, N., Mauri, F., Mazzarello, R., Paolini, S., Pasquarello, A., Paulatto, L., Sbraccia, C., Scandolo, S., Sclauzero, G., Seitsonen, A.P., Smogunov, A., Umari, P., Wentzcovitch, R.M., 2009. QUANTUM ESPRESSO: a modular and open-source software project for quantum simulations of materials. J. Phys. Condens. Matter 21, 395502. doi:10.1088/0953-8984/21/39/395502

Handler, M.R., Baker, J.A., Schiller, M., Bennett, V.C., Yaxley, G.M., 2009. Magnesium stable isotope composition of Earth's upper mantle. Earth Planet. Sci. Lett. 282, 306–313. doi:10.1016/j.epsl.2009.03.031

Hanyu, T., Kawabata, H., Tatsumi, Y., Kimura, J.-I., Hyodo, H., Sato, K., Miyazaki, T., Chang, Q., Hirahara, Y., Takahashi, T., Senda, R., Nakai, S., 2014. Isotope evolution in the HIMU reservoir beneath St. Helena: Implications for the mantle recycling of U and Th. Geochim. Cosmochim. Acta 143, 232–252. doi:10.1016/j.gca.2014.03.016

Hao, S., Wang, W., Qian, W., Wu, Z., 2019. Elasticity of akimotoite under the mantle conditions: Implications for multiple discontinuities and seismic anisotropies at the depth of ~600–750 km in subduction zones. Earth Planet. Sci. Lett. 528, 115830. doi:10.1016/j.epsl.2019.115830

Hazen, R.M., Weinberger, M.B., Yang, H., Prewitt, C.T., 2000. Comparative high-pressure crystal chemistry of wadsleyite, β-(Mg 1– x Fe x) 2 SiO 4 , with x = 0 and 0.25. Am. Mineral. 85, 770–777. doi:10.2138/am-2000-5-617

1260 Helffrich, G.R., Wood, B.J., 2001. The Earth's mantle. Nature 412, 501–507.
1261 doi:10.1038/35087500
1262 Hill, P.S., Schauble, E.A., 2008. Modeling the effects of bond environment on
1263 equilibrium iron isotope fractionation in ferric aquo-chloro complexes. Geochim.
1264 Cosmochim. Acta 72, 1939–1958. doi:10.1016/j.gca.2007.12.023
1265 Hills, D. V., Haggerty, S.E., 1989. Petrochemistry of eclogites from the Koidu
1266 Kimberlite Complex, Sierra Leone. Contrib. to Mineral. Petrol. 103, 397–422.
1267 doi:10.1007/BF01041749
1268 Hin, R.C., Coath, C.D., Carter, P.J., Nimmo, F., Lai, Y.J., Pogge von Strandmann,
1269 P.A.E., Willbold, M., Leinhardt, Z.M., Walter, M.J., Elliott, T., 2017.
1270 Magnesium isotope evidence that accretional vapour loss shapes planetary
1271 compositions. Nature 549, 511–527. doi:10.1038/nature23899
1272 Hirose, K., 2002. Phase transitions in pyrolitic mantle around 670-km depth:
1273 Implications for upwelling of plumes from the lower mantle. J. Geophys. Res.
1274 Solid Earth 107, ECV 3-1-ECV 3-13. doi:10.1029/2001JB000597
1275 Hsu, H., Blaha, P., Cococcioni, M., Wentzcovitch, R.M., 2011. Spin-State Crossover
1276 and Hyperfine Interactions of Ferric Iron in MgSiO3 Perovskite. Phys. Rev. Lett.
1277 106, 118501. doi:10.1103/PhysRevLett.106.118501
1278 Hu, Y., Teng, F.-Z., Ionov, D.A., 2020. Magnesium isotopic composition of
1279 metasomatized upper sub-arc mantle and its implications to Mg cycling in
1280 subduction zones. Geochim. Cosmochim. Acta 278, 219–234.
1281 doi:10.1016/j.gca.2019.09.030
1282 Hu, Y., Teng, F.-Z., Plank, T., Huang, K.-J., 2017. Magnesium isotopic composition
1283 of subducting marine sediments. Chem. Geol. 466, 15–31.
1284 doi:10.1016/j.chemgeo.2017.06.010
1285 Hu, Yan, Teng, F.-Z., Zhang, H.-F., Xiao, Y., Su, B.-X., 2016. Metasomatism-
1286 induced mantle magnesium isotopic heterogeneity: Evidence from pyroxenites.
1287 Geochim. Cosmochim. Acta 185, 88–111. doi:10.1016/j.gca.2015.11.001
1288 Hu, Yi, Wu, Z., Dera, P., Bina, C., 2016. Thermodynamic and elastic properties of
1289 pyrope at high pressure and high temperature by first-principles calculations. J.
1290 Geophys. Res. 1–15. doi:10.1002/2016JB013026.Received
1291 Huang, F., Chen, L., Wu, Z., Wang, W., 2013. First-principles calculations of
1292 equilibrium Mg isotope fractionations between garnet, clinopyroxene,
1293 orthopyroxene, and olivine: Implications for Mg isotope thermometry. Earth
1294 Planet. Sci. Lett. 367, 61–70. doi:10.1016/j.epsl.2013.02.025
1295 Huang, F., Wu, Z., Huang, S., Wu, F., 2014. First-principles calculations of
1296 equilibrium silicon isotope fractionation among mantle minerals. Geochim.
1297 Cosmochim. Acta 140, 509–520. doi:10.1016/j.gca.2014.05.035
1298 Huang, F., Zhang, Z., Lundstrom, C.C., Zhi, X., 2011a. Iron and magnesium isotopic
1299 compositions of peridotite xenoliths from Eastern China. Geochim. Cosmochim.
1300 Acta 75, 3318–3334. doi:10.1016/j.gca.2011.03.036
1301 Huang, F., Zhang, Z., Lundstrom, C.C., Zhi, X., 2011b. Iron and magnesium isotopic

compositions of peridotite xenoliths from Eastern China. Geochim. Cosmochim. Acta 75, 3318–3334. doi:10.1016/j.gca.2011.03.036
Huang, F., Zhou, C., Wang, W., Kang, J., Wu, Z., 2019. First-principles calculations of equilibrium Ca isotope fractionation: Implications for oldhamite formation and evolution of lunar magma ocean. Earth Planet. Sci. Lett. 510, 153–160. doi:10.1016/j.epsl.2018.12.034
Huang, J., Li, S.-G., Xiao, Y., Ke, S., Li, W.-Y., Tian, Y., 2015. Origin of low δ26Mg Cenozoic basalts from South China Block and their geodynamic implications. Geochim. Cosmochim. Acta 164, 298–317. doi:10.1016/j.gca.2015.04.054
Huang, K.-J., Teng, F.-Z., Plank, T., Staudigel, H., Hu, Y., Bao, Z.-Y., 2018. Magnesium isotopic composition of altered oceanic crust and the global Mg cycle. Geochim. Cosmochim. Acta 238, 357–373. doi:10.1016/j.gca.2018.07.011
Huang, K.-J., Teng, F.-Z., Shen, B., Xiao, S., Lang, X., Ma, H.-R., Fu, Y., Peng, Y., 2016. Episode of intense chemical weathering during the termination of the 635 Ma Marinoan glaciation. Proc. Natl. Acad. Sci. 113, 14904–14909. doi:10.1073/pnas.1607712113
Huang, K.-J., Teng, F.-Z., Wei, G.-J., Ma, J.-L., Bao, Z.-Y., 2012. Adsorption- and desorption-controlled magnesium isotope fractionation during extreme weathering of basalt in Hainan Island, China. Earth Planet. Sci. Lett. 359–360, 73–83. doi:10.1016/j.epsl.2012.10.007
Inoue, T., Irifune, T., Higo, Y., Sanehira, T., Sueda, Y., Yamada, A., Shinmei, T., Yamazaki, D., Ando, J., Funakoshi, K., Utsumi, W., 2006. The phase boundary between wadsleyite and ringwoodite in Mg2SiO4 determined by in situ X-ray diffraction. Phys. Chem. Miner. 33, 106–114. doi:10.1007/s00269-005-0053-y
Ita, J., Stixrude, L., 1992. Petrology, elasticity, and composition of the mantle transition zone. J. Geophys. Res. 97, 6849. doi:10.1029/92JB00068
Katsura, T., Ito, E., 1989. The system Mg 2 SiO 4 -Fe 2 SiO 4 at high pressures and temperatures: Precise determination of stabilities of olivine, modified spinel, and spinel. J. Geophys. Res. Solid Earth 94, 15663–15670. doi:10.1029/JB094iB11p15663
Katsura, T., Yamada, H., Nishikawa, O., Song, M., Kubo, A., Shinmei, T., Yokoshi, S., Aizawa, Y., Yoshino, T., Walter, M.J., Ito, E., Funakoshi, K., 2004. Olivine-wadsleyite transition in the system (Mg,Fe) 2 SiO 4. J. Geophys. Res. Solid Earth 109, n/a–n/a. doi:10.1029/2003JB002438
Kawabata, H., Hanyu, T., Chang, Q., Kimura, J.-I., Nichols, A.R.L., Tatsumi, Y., 2011. The Petrology and Geochemistry of St. Helena Alkali Basalts: Evaluation of the Oceanic Crust-recycling Model for HIMU OIB. J. Petrol. 52, 791–838. doi:10.1093/petrology/egr003
Kennett, B.L.N., Engdahl, E.R., Buland, R., 1995. Constraints on seismic velocities in the Earth from traveltimes. Geophys. J. Int. 122, 108–124. doi:10.1111/j.1365-246X.1995.tb03540.x
Kind, R., Li, X., 2015. Deep Earth Structure - Transition Zone and Mantle

Discontinuities, in: Treatise on Geophysics. Elsevier, pp. 655–682. doi:10.1016/B978-0-444-53802-4.00017-8
Kirfel, A., Lippmann, T., Blaha, P., Schwarz, K., Cox, D.F., Rosso, K.M., Gibbs, G. V., 2005. Electron density distribution and bond critical point properties for forsterite, Mg2 SiO4, determined with synchrotron single crystal X-ray diffraction data. Phys. Chem. Miner. 32, 301–313. doi:10.1007/s00269-005-0468-5
Kowalski, P.M., Jahn, S., 2011. Prediction of equilibrium Li isotope fractionation between minerals and aqueous solutions at high P and T: An efficient ab initio approach. Geochim. Cosmochim. Acta 75, 6112–6123. doi:10.1016/j.gca.2011.07.039
Kowalski, P.M., Wunder, B., Jahn, S., 2013a. Ab initio prediction of equilibrium boron isotope fractionation between minerals and aqueous fluids at high P and T. Geochim. Cosmochim. Acta 101, 285–301. doi:10.1016/j.gca.2012.10.007
Kowalski, P.M., Wunder, B., Jahn, S., 2013b. Ab initio prediction of equilibrium boron isotope fractionation between minerals and aqueous fluids at high P and T. Geochim. Cosmochim. Acta 101, 285–301. doi:10.1016/j.gca.2012.10.007
Lazar, C., Young, E.D., Manning, C.E., 2012. Experimental determination of equilibrium nickel isotope fractionation between metal and silicate from 500°C to 950°C. Geochim. Cosmochim. Acta 86, 276–295. doi:10.1016/j.gca.2012.02.024
Li, S.-G., Yang, W., Ke, S., Meng, X., Tian, H., Xu, L., He, Y., Huang, J., Wang, X.-C., Xia, Q., Sun, W., Yang, X., Ren, Z.-Y., Wei, H., Liu, Y., Meng, F., Yan, J., 2016. Deep carbon cycles constrained by a large-scale mantle Mg isotope anomaly in eastern China. Natl. Sci. Rev. 4, nww070. doi:10.1093/nsr/nww070
Li, W.-Y., Teng, F.-Z., Halama, R., Keller, J., Klaudius, J., 2016. Magnesium isotope fractionation during carbonatite magmatism at Oldoinyo Lengai, Tanzania. Earth Planet. Sci. Lett. 444, 26–33. doi:10.1016/j.epsl.2016.03.034
Li, W.-Y., Teng, F.-Z., Ke, S., Rudnick, R.L., Gao, S., Wu, F.-Y., Chappell, B.W., 2010. Heterogeneous magnesium isotopic composition of the upper continental crust. Geochim. Cosmochim. Acta 74, 6867–6884. doi:10.1016/j.gca.2010.08.030
Li, W.-Y., Teng, F.-Z., Xiao, Y., Huang, J., 2011. High-temperature inter-mineral magnesium isotope fractionation in eclogite from the Dabie orogen, China. Earth Planet. Sci. Lett. 304, 224–230. doi:10.1016/j.epsl.2011.01.035
Li, X., Liu, Y., 2011. Equilibrium Se isotope fractionation parameters: A first-principles study. Earth Planet. Sci. Lett. 304, 113–120. doi:10.1016/j.epsl.2011.01.022
Li, Y., Wang, W., Huang, S., Wang, K., Wu, Z., 2019a. First-principles investigation of the concentration effect on equilibrium fractionation of K isotopes in feldspars. Geochim. Cosmochim. Acta 245, 374–384. doi:10.1016/j.gca.2018.11.006

Li, Y., Wang, W., Wu, Z., Huang, S., 2019b. First-principles investigation of equilibrium K isotope fractionation among K-bearing minerals. Geochim. Cosmochim. Acta 264, 30–42. doi:10.1016/j.gca.2019.07.038

Liu, J., Dauphas, N., Roskosz, M., Hu, M.Y., Yang, H., Bi, W., Zhao, J., Alp, E.E., Hu, J.Y., Lin, J.F., 2017. Iron isotopic fractionation between silicate mantle and metallic core at high pressure. Nat. Commun. 8, ncomms14377. doi:10.1038/ncomms14377

Liu, S.-A., Teng, F.-Z., He, Y., Ke, S., Li, S., 2010. Investigation of magnesium isotope fractionation during granite differentiation: Implication for Mg isotopic composition of the continental crust. Earth Planet. Sci. Lett. 297, 646–654. doi:10.1016/j.epsl.2010.07.019

Liu, S.-A., Teng, F.-Z., Yang, W., Wu, F.-Y., 2011. High-temperature inter-mineral magnesium isotope fractionation in mantle xenoliths from the North China craton. Earth Planet. Sci. Lett. 308, 131–140. doi:10.1016/j.epsl.2011.05.047

Liu, X.-N., Hin, R.C., Coath, C.D., van Soest, M., Melekhova, E., Elliott, T., 2022. Equilibrium olivine-melt Mg isotopic fractionation explains high δ26Mg values in arc lavas. Geochemical Perspect. Lett. 22, 42–47. doi:10.7185/geochemlet.2226

Liu, X.M., Teng, F.Z., Rudnick, R.L., McDonough, W.F., Cummings, M.L., 2014. Massive magnesium depletion and isotope fractionation in weathered basalts. Geochim. Cosmochim. Acta 135, 336–349. doi:10.1016/j.gca.2014.03.028

Luhr, J.F., Carmichael, I.S.E., Varekamp, J.C., 1984. The 1982 eruptions of El Chichón Volcano, Chiapas, Mexico: Mineralogy and petrology of the anhydritebearing pumices. J. Volcanol. Geotherm. Res. 23, 69–108. doi:10.1016/0377-0273(84)90057-X

Ma, Y., Liu, X., 2019. Kinetics and Thermodynamics of Mg-Al Disorder in MgAl2O4-Spinel: A Review. Molecules 24, 1704. doi:10.3390/molecules24091704

Macris, C.A., Manning, C.E., Young, E.D., 2015. Crystal chemical constraints on inter-mineral Fe isotope fractionation and implications for Fe isotope disequilibrium in San Carlos mantle xenoliths. Geochim. Cosmochim. Acta 154, 168–185. doi:10.1016/j.gca.2015.01.024

Macris, C.A., Young, E.D., Manning, C.E., 2013. Experimental determination of equilibrium magnesium isotope fractionation between spinel, forsterite, and magnesite from 600 to 800 °C. Geochim. Cosmochim. Acta 118, 18–32. doi:10.1016/j.gca.2013.05.008

McDonough, W.F., Sun, S. -s., 1995. The composition of the Earth. Chem. Geol. 120, 223–253. doi:10.1016/0009-2541(94)00140-4

Méheut, M., Lazzeri, M., Balan, E., Mauri, F., 2009. Structural control over equilibrium silicon and oxygen isotopic fractionation: A first-principles density-functional theory study. Chem. Geol. 258, 28–37. doi:10.1016/j.chemgeo.2008.06.051

Meng, Y., Fei, Y., Weidner, D.J., Gwanmesia, G.D., Hu, J., 1994. Hydrostatic compression of ?-Mg2SiO4 to mantle pressures and 700 K: Thermal equation of state and related thermoelastic properties. Phys. Chem. Miner. 21, 407–412. doi:10.1007/BF00203299

Núñez-Valdez, M., Wu, Z., Yu, Y.G., Wentzcovitch, R.M., 2013. Thermal elasticity of (Fe x ,Mg 1− x) 2 SiO 4 olivine and wadsleyite. Geophys. Res. Lett. 40, 290–294. doi:10.1002/grl.50131

Núñez Valdez, M., Wu, Z., Yu, Y.G., Revenaugh, J., Wentzcovitch, R.M., 2012. Thermoelastic properties of ringwoodite (Fex,Mg1−x)2SiO4: Its relationship to the 520km seismic discontinuity. Earth Planet. Sci. Lett. 351–352, 115–122. doi:10.1016/j.epsl.2012.07.024

O'Neill, H.S.C., Annersten, H., Virgo, D., 1992. The temperature dependence of the cation distribution in magnesioferrite (MgFe2O4) from powder XRD structural refinements and Mössbauer spectroscopy. Am. Mineral. 77, 725–740.

O'Neill, H.S.C., Dollase, W.A., 1994. Crystal structures and cation distributions in simple spinels from powder XRD structural refinements: MgCr2O4, ZnCr2O4, Fe3O4 and the temperature dependence of the cation distribution in ZnAl2O4. Phys. Chem. Miner. 20, 541–555. doi:10.1007/BF00211850

Pavese, A., Artioli, G., Prencipe, M., 1995. X-ray single-crystal diffraction study of pyrope in the temperature range 30-973 K. Am. Mineral. 80, 457–464. doi:10.2138/am-1995-5-606

Peterson, R.C., Lager, G.A., Hitterman, R.L., 1991. A time-of-flight neutron powder diffraction study of MgAl2O4 at temperatures up to 1273 K. Am. Mineral. 76, 1455–1458.

Qian, W., Wang, W., Zou, F., Wu, Z., 2018. Elasticity of Orthoenstatite at High Pressure and Temperature: Implications for the Origin of Low V P / V S Zones in the Mantle Wedge. Geophys. Res. Lett. 45, 665–673. doi:10.1002/2017GL075647

Qin, T., Wu, F., Wu, Z., Huang, F., 2016. First-principles calculations of equilibrium fractionation of O and Si isotopes in quartz, albite, anorthite, and zircon. Contrib. to Mineral. Petrol. 171, 91. doi:10.1007/s00410-016-1303-3

Rabin, S., Blanchard, M., Pinilla, C., Poitrasson, F., Gregoire, M., 2021. First-principles calculation of iron and silicon isotope fractionation between Fe-bearing minerals at magmatic temperatures: The importance of second atomic neighbors. Geochim. Cosmochim. Acta 304, 101–118. doi:10.1016/j.gca.2021.03.028

Richet, P., Bottinga, Y., Javoy, M., 1977. A Review of Hydrogen, Carbon, Nitrogen, Oxygen, Sulphur, and Chlorine Stable Isotope Fractionation Among Gaseous Molecules. Annu. Rev. Earth Planet. Sci. 5, 65–110. doi:10.1146/annurev.ea.05.050177.000433

Ringwood, A.E., 1962. A model for the upper mantle. J. Geophys. Res. 67, 857–867. doi:10.1029/JZ067i002p00857

1470 Roskosz, M., Amet, Q., Fitoussi, C., Dauphas, N., Bourdon, B., Tissandier, L., Hu,
1471 M.Y., Said, A., Alatas, A., Alp, E.E., 2020. Redox and structural controls on tin
1472 isotopic fractionations among magmas. Geochim. Cosmochim. Acta 268, 42–55.
1473 doi:10.1016/j.gca.2019.09.036
1474 Ross, N.L., 1997. The equation of state and high-pressure behavior of magnesite. Am.
1475 Mineral. 82, 682–688. doi:10.2138/am-1997-7-805
1476 Rudnick, R.L., Gao, S., 2014. Composition of the Continental Crust, in: Treatise on
1477 Geochemistry. Elsevier, pp. 1–51. doi:10.1016/B978-0-08-095975-7.00301-6
1478 Schauble, E., Rossman, G.R., Taylor, H.P., 2004. Theoretical estimates of equilibrium
1479 chromium-isotope fractionations. Chem. Geol. 205, 99–114.
1480 doi:10.1016/j.chemgeo.2003.12.015
1481 Schauble, E.A., 2011. First-principles estimates of equilibrium magnesium isotope
1482 fractionation in silicate, oxide, carbonate and hexaaquamagnesium(2+) crystals.
1483 Geochim. Cosmochim. Acta 75, 844–869. doi:10.1016/j.gca.2010.09.044
1484 Schultz, R., Gu, Y.J., 2013. Multiresolution imaging of mantle reflectivity structure
1485 using SS and P'P' precursors. Geophys. J. Int. 195, 668–683.
1486 doi:10.1093/gji/ggt266
1487 Shahar, A., Hillgren, V.J., Young, E.D., Fei, Y., Macris, C.A., Deng, L., 2011. High-
1488 temperature Si isotope fractionation between iron metal and silicate. Geochim.
1489 Cosmochim. Acta 75, 7688–7697. doi:10.1016/j.gca.2011.09.038
1490 Shahar, A., Schauble, E.A., Caracas, R., Gleason, A.E., Reagan, M.M., Xiao, Y., Shu,
1491 J., Mao, W., 2016. Pressure-dependent isotopic composition of iron alloys.
1492 Science (80-.). 352, 580–582. doi:10.1126/science.aad9945
1493 Shahar, A., Young, E.D., Manning, C.E., 2008. Equilibrium high-temperature Fe
1494 isotope fractionation between fayalite and magnetite: An experimental
1495 calibration. Earth Planet. Sci. Lett. 268, 330–338. doi:10.1016/j.epsl.2008.01.026
1496 Shahar, A., Ziegler, K., Young, E.D., Ricolleau, A., Schauble, E.A., Fei, Y., 2009.
1497 Experimentally determined Si isotope fractionation between silicate and Fe metal
1498 and implications for Earth's core formation. Earth Planet. Sci. Lett. 288, 228–
1499 234. doi:10.1016/j.epsl.2009.09.025
1500 Shukla, G., Cococcioni, M., Wentzcovitch, R.M., 2016. Thermoelasticity of Fe 3+ -
1501 and Al-bearing bridgmanite. Geophys. Res. Lett. doi:10.1002/2016GL069332
1502 Shukla, G., Wentzcovitch, R.M., 2016. Spin crossover in
1503 (Mg,Fe3+)(Si,Fe3+)O3bridgmanite: Effects of disorder, iron concentration, and
1504 temperature. Phys. Earth Planet. Inter. 260, 53–61.
1505 doi:10.1016/j.pepi.2016.09.003
1506 Shukla, G., Wu, Z., Hsu, H., Floris, A., Cococcioni, M., Wentzcovitch, R.M., 2015.
1507 Thermoelasticity of Fe 2+ -bearing bridgmanite. Geophys. Res. Lett. 42, 1741–
1508 1749. doi:10.1002/2014GL062888
1509 Stracke, A., Tipper, E.T., Klemme, S., Bizimis, M., 2018. Mg isotope systematics
1510 during magmatic processes: Inter-mineral fractionation in mafic to ultramafic
1511 Hawaiian xenoliths. Geochim. Cosmochim. Acta 226, 192–205.

1512 doi:10.1016/j.gca.2018.02.002
1513 Sugahara, M., Yoshiasa, A., Komatsu, Y., Yamanaka, T., Bolfan-Casanova, N.,
1514 Nakatsuka, A., Sasaki, S., Tanaka, M., 2006. Reinvestigation of the MgSiO3
1515 perovskite structure at high pressure. Am. Mineral. 91, 533–536.
1516 doi:10.2138/am.2006.1980
1517 Tang, H., Szumila, I., Trail, D., Young, E.D., 2021. Experimental determination of the
1518 effect of Cr on Mg isotope fractionation between spinel and forsterite. Geochim.
1519 Cosmochim. Acta 296, 152–169. doi:10.1016/j.gca.2020.12.028
1520 Teng, F.-Z., 2017. Magnesium Isotope Geochemistry. Rev. Mineral. Geochemistry
1521 82, 219–287. doi:10.2138/rmg.2017.82.7
1522 Teng, F.-Z., Li, W.-Y., Ke, S., Marty, B., Dauphas, N., Huang, S., Wu, F.-Y.,
1523 Pourmand, A., 2010a. Magnesium isotopic composition of the Earth and
1524 chondrites. Geochim. Cosmochim. Acta 74, 4150–4166.
1525 doi:10.1016/j.gca.2010.04.019
1526 Teng, F.-Z., Li, W.-Y., Rudnick, R.L., Gardner, L.R., 2010b. Contrasting lithium and
1527 magnesium isotope fractionation during continental weathering. Earth Planet.
1528 Sci. Lett. 300, 63–71. doi:10.1016/j.epsl.2010.09.036
1529 Teng, F.-Z., Wadhwa, M., Helz, R.T., 2007. Investigation of magnesium isotope
1530 fractionation during basalt differentiation: Implications for a chondritic
1531 composition of the terrestrial mantle. Earth Planet. Sci. Lett. 261, 84–92.
1532 doi:10.1016/j.epsl.2007.06.004
1533 Togo, A., Tanaka, I., 2015. First principles phonon calculations in materials science.
1534 Scr. Mater. 108, 1–5. doi:10.1016/j.scriptamat.2015.07.021
1535 Toplis, M.J., Carroll, M.R., 1995. An Experimental Study of the Influence of Oxygen
1536 Fugacity on Fe-Ti Oxide Stability, Phase Relations, and Mineral--Melt Equilibria
1537 in Ferro-Basaltic Systems. J. Petrol. 36, 1137–1170.
1538 doi:10.1093/petrology/36.5.1137
1539 Troullier, N., Martins, J.L., 1991. Efficient pseudopotentials for plane-wave
1540 calculations. II. Operators for fast iterative diagonalization. Phys. Rev. B 43,
1541 8861–8869. doi:10.1103/PhysRevB.43.8861
1542 Tsujino, N., Yoshino, T., Yamazaki, D., Sakurai, M., Sun, W., Xu, F., Tange, Y.,
1543 Higo, Y., 2019. Phase transition of wadsleyite-ringwoodite in the Mg2SiO4-
1544 Fe2SiO4 system. Am. Mineral. 104, 588–594. doi:10.2138/am-2019-6823
1545 Uchida, H., 2005. Single-crystal X-ray diffraction of spinels from the San Carlos
1546 Volcanic Field, Arizona: Spinel as a geothermometer. Am. Mineral. 90, 1900–
1547 1908. doi:10.2138/am.2005.1795
1548 Urey, H.C., 1947. The thermodynamic properties of isotopic substances. J. Chem.
1549 Soc. 562. doi:10.1039/jr9470000562
1550 Vanderbilt, D., 1990. Soft self-consistent pseudopotentials in a generalized eigenvalue
1551 formalism. Phys. Rev. B 41, 7892–7895. doi:10.1103/PhysRevB.41.7892
1552 Wang, S.-J., Teng, F.-Z., Li, S.-G., 2014. Tracing carbonate–silicate interaction
1553 during subduction using magnesium and oxygen isotopes. Nat. Commun. 5,

5328. doi:10.1038/ncomms6328
Wang, S.-J., Teng, F.-Z., Rudnick, R.L., Li, S.-G., 2015. Magnesium isotope evidence for a recycled origin of cratonic eclogites. Geology 43, G37259.1. doi:10.1130/G37259.1
Wang, S.-J., Teng, F.-Z., Scott, J.M., 2016. Tracing the origin of continental HIMU-like intraplate volcanism using magnesium isotope systematics. Geochim. Cosmochim. Acta 185, 78–87. doi:10.1016/j.gca.2016.01.007
Wang, S.-J., Teng, F.-Z., Williams, H.M., Li, S.-G., 2012. Magnesium isotopic variations in cratonic eclogites: Origins and implications. Earth Planet. Sci. Lett. 359–360, 219–226. doi:10.1016/j.epsl.2012.10.016
Wang, W., Huang, S., Huang, F., Zhao, X., Wu, Z., 2020a. Equilibrium inter-mineral titanium isotope fractionation: Implication for high-temperature titanium isotope geochemistry. Geochim. Cosmochim. Acta 269, 540–553. doi:10.1016/j.gca.2019.11.008
Wang, W., Li, C.H., Brodholt, J.P., Huang, S., Walter, M.J., Li, M., Wu, Z., Huang, F., Wang, S.J., 2021a. Sulfur isotopic signature of Earth established by planetesimal volatile evaporation. Nat. Geosci. 14, 806–811. doi:10.1038/s41561-021-00838-6
Wang, W., Liu, J., Yang, H., Dorfman, S.M., Lv, M., Li, J., Zhu, F., Zhao, J., Hu, M.Y., Bi, W., Alp, E.E., Xiao, Y., Wu, Z., Lin, J., 2021b. Iron force constants of bridgmanite at high pressure: Implications for iron isotope fractionation in the deep mantle. Geochim. Cosmochim. Acta 294, 215–231. doi:10.1016/j.gca.2020.11.025
Wang, W., Liu, J., Zhu, F., Li, M., Dorfman, S.M., Li, J., Wu, Z., 2021c. Formation of large low shear velocity provinces through the decomposition of oxidized mantle. Nat. Commun. 12, 1911. doi:10.1038/s41467-021-22185-1
Wang, W., Qin, T., Zhou, C., Huang, S., Wu, Z., Huang, F., 2017a. Concentration effect on equilibrium fractionation of Mg-Ca isotopes in carbonate minerals: Insights from first-principles calculations. Geochim. Cosmochim. Acta 208, 185–197. doi:10.1016/j.gca.2017.03.023
Wang, W., Tschauner, O., Huang, S., Wu, Z., Meng, Y., Bechtel, H., Mao, H., 2021d. Coupled deep mantle carbon-water cycle: Evidence from lower-mantle diamonds. Innov. 2, 100117. doi:10.1016/j.xinn.2021.100117
Wang, W., Walter, M.J., Peng, Y., Redfern, S., Wu, Z., 2019a. Constraining olivine abundance and water content of the mantle at the 410-km discontinuity from the elasticity of olivine and wadsleyite. Earth Planet. Sci. Lett. 519, 1–11. doi:10.1016/j.epsl.2019.04.018
Wang, W., Wu, Z., 2018. Elasticity of Corundum at High Pressures and Temperatures: Implications for Pyrope Decomposition and Al-Content Effect on Elastic Properties of Bridgmanite. J. Geophys. Res. Solid Earth 123, 1201–1216. doi:10.1002/2017JB015088
Wang, W., Wu, Z., Huang, F., 2021e. Equilibrium barium isotope fractionation

between minerals and aqueous solution from first-principles calculations. Geochim. Cosmochim. Acta 292, 64–77. doi:10.1016/j.gca.2020.09.021
Wang, W., Xu, Y., Sun, D., Ni, S., Wentzcovitch, R., Wu, Z., 2020b. Velocity and density characteristics of subducted oceanic crust and the origin of lower-mantle heterogeneities. Nat. Commun. 11, 64. doi:10.1038/s41467-019-13720-2
Wang, W., Zhang, H., Brodholt, J.P., Wu, Z., 2020c. Elasticity of hydrous ringwoodite at mantle conditions: Implication for water distribution in the lowermost mantle transition zone. Earth Planet. Sci. Lett. 554, 116626. doi:10.1016/j.epsl.2020.116626
Wang, W., Zhou, C., Liu, Y., Wu, Z., Huang, F., 2019b. Equilibrium Mg isotope fractionation among aqueous Mg2+, carbonates, brucite and lizardite: Insights from first-principles molecular dynamics simulations. Geochim. Cosmochim. Acta 250, 117–129. doi:10.1016/j.gca.2019.01.042
Wang, W., Zhou, C., Qin, T., Kang, J., Huang, S., Wu, Z., Huang, F., 2017b. Effect of Ca content on equilibrium Ca isotope fractionation between orthopyroxene and clinopyroxene. Geochim. Cosmochim. Acta 219, 44–56. doi:10.1016/j.gca.2017.09.022
Wang, X.-J., Chen, L.-H., Hanyu, T., Zhong, Y., Shi, J.-H., Liu, X.-W., Kawabata, H., Zeng, G., Xie, L.-W., 2021. Magnesium isotopic fractionation during basalt differentiation as recorded by evolved magmas. Earth Planet. Sci. Lett. 565, 116954. doi:10.1016/j.epsl.2021.116954
Wang, X.-J., Chen, L.-H., Hofmann, A.W., Hanyu, T., Kawabata, H., Zhong, Y., Xie, L.-W., Shi, J.-H., Miyazaki, T., Hirahara, Y., Takahashi, T., Senda, R., Chang, Q., Vaglarov, B.S., Kimura, J.-I., 2018. Recycled ancient ghost carbonate in the Pitcairn mantle plume. Proc. Natl. Acad. Sci. U. S. A. 115, 8682–8687. doi:10.1073/pnas.1719570115
Wang, X.-J., Chen, L.-H., Hofmann, A.W., Mao, F.-G., Liu, J.-Q., Zhong, Y., Xie, L.-W., Yang, Y.-H., 2017. Mantle transition zone-derived EM1 component beneath NE China: Geochemical evidence from Cenozoic potassic basalts. Earth Planet. Sci. Lett. 465, 16–28. doi:10.1016/j.epsl.2017.02.028
Wechsler, B.A., Lindsley, D.H., Prewitt, C.T., 1984. Crystal structure and cation distribution in titanomagnetites (Fe3-xTixO4). Am. Mineral. 69, 754–770.
Wentzcovitch, R.M., 1991. Invariant molecular-dynamics approach to structural phase transitions. Phys. Rev. B 44, 2358–2361. doi:10.1103/PhysRevB.44.2358
Wentzcovitch, R.M., Yu, Y.G., Wu, Z., 2010. Thermodynamic Properties and Phase Relations in Mantle Minerals Investigated by First Principles Quasiharmonic Theory. Rev. Mineral. Geochemistry 71, 59–98. doi:10.2138/rmg.2010.71.4
Williams, H.M., Nielsen, S.G., Renac, C., Griffin, W.L., O'Reilly, S.Y., McCammon, C.A., Pearson, N., Viljoen, F., Alt, J.C., Halliday, A.N., 2009. Fractionation of oxygen and iron isotopes by partial melting processes: Implications for the interpretation of stable isotope signatures in mafic rocks. Earth Planet. Sci. Lett. 283, 156–166. doi:10.1016/j.epsl.2009.04.011

Wu, F.-Y., Walker, R.J., Yang, Y.-H., Yuan, H.-L., Yang, J.-H., 2006. The chemical-temporal evolution of lithospheric mantle underlying the North China Craton. Geochim. Cosmochim. Acta 70, 5013–5034. doi:10.1016/j.gca.2006.07.014

Wu, Z., Huang, F., Huang, S., 2015. Isotope fractionation induced by phase transformation: First-principles investigation for Mg2SiO4. Earth Planet. Sci. Lett. 409, 339–347. doi:10.1016/j.epsl.2014.11.004

Wu, Z., Justo, J.F., Wentzcovitch, R.M., 2013. Elastic Anomalies in a Spin-Crossover System: Ferropericlase at Lower Mantle Conditions. Phys. Rev. Lett. 110, 228501. doi:10.1103/PhysRevLett.110.228501

Wu, Z., Wang, W., 2016. First-principles calculations of elasticity of minerals at high temperature and pressure. Sci. China Earth Sci. 59, 1107–1137. doi:10.1007/s11430-016-5296-6

Xiao, Y., Hoefs, J., van den Kerkhof, A.M., Fiebig, J., Zheng, Y., 2000. Fluid history of UHP metamorphism in Dabie Shan, China: a fluid inclusion and oxygen isotope study on the coesite-bearing eclogite from Bixiling. Contrib. to Mineral. Petrol. 139, 1–16. doi:10.1007/s004100050570

Xiao, Y., Teng, F.-Z., Zhang, H.-F., Yang, W., 2013. Large magnesium isotope fractionation in peridotite xenoliths from eastern North China craton: Product of melt–rock interaction. Geochim. Cosmochim. Acta 115, 241–261. doi:10.1016/j.gca.2013.04.011

Xiao, Y., Teng, F., Su, B., Hu, Y., Zhou, M., Zhu, B., Shi, R., Huang, Q., Gong, X., He, Y., 2016. Iron and magnesium isotopic constraints on the origin of chemical heterogeneity in podiform chromitite from the Luobusa ophiolite, Tibet. Geochemistry, Geophys. Geosystems 17, 940–953. doi:10.1002/2015GC006223

Yamanaka, T., Komatsu, Y., Sugahara, M., Nagai, T., 2005. Structure change of MgSiO3, MgGeO3, and MgTiO3 ilmenites under compression. Am. Mineral. 90, 1301–1307. doi:10.2138/am.2005.1621

Yang, D., Wang, W., Wu, Z., 2017. Elasticity of superhydrous phase B at the mantle temperatures and pressures: Implications for 800 km discontinuity and water flow into the lower mantle. J. Geophys. Res. Solid Earth 122, 5026–5037. doi:10.1002/2017JB014319

Yang, H., Ghose, S., 1995. High temperature single crystal X-ray diffraction studies of the ortho-proto phase transition in enstatite, Mg2Si2O6 at 1360 K. Phys. Chem. Miner. 22, 300–310. doi:10.1007/BF00202770

Yang, H., Lin, J.F., Hu, M.Y., Roskosz, M., Bi, W., Zhao, J., Alp, E.E., Liu, Jin, Liu, Jiachao, Wentzowitch, R.M., Okuchi, T., Dauphas, N., 2019. Iron isotopic fractionation in mineral phases from Earth's lower mantle: Did terrestrial magma ocean crystallization fractionate iron isotopes? Earth Planet. Sci. Lett. 506, 113–122. doi:10.1016/j.epsl.2018.10.034

Yang, R., Wu, Z., 2014. Elastic properties of stishovite and the CaCl2-type silica at the mantle temperature and pressure: An ab initio investigation. Earth Planet. Sci. Lett. 404, 14–21. doi:10.1016/j.epsl.2014.07.020

Yang, W., Teng, F.-Z., Zhang, H.-F., Li, S.-G., 2012. Magnesium isotopic systematics of continental basalts from the North China craton: Implications for tracing subducted carbonate in the mantle. Chem. Geol. 328, 185–194. doi:10.1016/j.chemgeo.2012.05.018

Yao, C., Wu, Z., Zou, F., Sun, W., 2018. Thermodynamic and Elastic Properties of Magnesite at Mantle Conditions: First-Principles Calculations. Geochemistry, Geophys. Geosystems 19, 2719–2731. doi:10.1029/2017GC007396

Young, E.D., Galy, A., 2004. The Isotope Geochemistry and Cosmochemistry of Magnesium. Rev. Mineral. Geochemistry 55, 197–230. doi:10.2138/gsrmg.55.1.197

Young, E.D., Manning, C.E., Schauble, E.A., Shahar, A., Macris, C.A., Lazar, C., Jordan, M., 2015. High-temperature equilibrium isotope fractionation of non-traditional stable isotopes: Experiments, theory, and applications. Chem. Geol. 395, 176–195. doi:10.1016/j.chemgeo.2014.12.013

Young, E.D., Shahar, A., Nimmo, F., Schlichting, H.E., Schauble, E.A., Tang, H., Labidi, J., 2019. Near-equilibrium isotope fractionation during planetesimal evaporation. Icarus 323, 1–15. doi:10.1016/j.icarus.2019.01.012

Young, E.D., Tonui, E., Manning, C.E., Schauble, E., Macris, C.A., 2009. Spinel–olivine magnesium isotope thermometry in the mantle and implications for the Mg isotopic composition of Earth. Earth Planet. Sci. Lett. 288, 524–533. doi:10.1016/j.epsl.2009.10.014

Yu, Y.G., Wentzcovitch, R.M., Tsuchiya, T., Umemoto, K., Weidner, D.J., 2007. First principles investigation of the postspinel transition in Mg 2 SiO 4. Geophys. Res. Lett. 34, L10306. doi:10.1029/2007GL029462

Yu, Y.G., Wentzcovitch, R.M., Vinograd, V.L., Angel, R.J., 2011. Thermodynamic properties of MgSiO 3 majorite and phase transitions near 660 km depth in MgSiO 3 and Mg 2 SiO 4 : A first principles study. J. Geophys. Res. 116, B02208. doi:10.1029/2010JB007912

Yu, Y.G., Wu, Z., Wentzcovitch, R.M., 2008. α–β–γ transformations in Mg2SiO4 in Earth's transition zone. Earth Planet. Sci. Lett. 273, 115–122. doi:10.1016/j.epsl.2008.06.023

Zhang, X.Q., Song, X.Y., Chen, L.M., Xie, W., Yu, S.Y., Zheng, W.Q., Deng, Y.F., Zhang, J.F., Gui, S.G., 2012. Fractional crystallization and the formation of thick Fe-Ti-V oxide layers in the Baima layered intrusion, SW China. Ore Geol. Rev. 49, 96–108. doi:10.1016/j.oregeorev.2012.09.003

Zou, F., Wu, Z., Wang, W., Wentzcovitch, R.M., 2018. An Extended Semianalytical Approach for Thermoelasticity of Monoclinic Crystals: Application to Diopside. J. Geophys. Res. Solid Earth 123, 7629–7643. doi:10.1029/2018JB016102

ell parameters and volumes of mantle minerals compared with experimental measurements. Cell parameters are calculated a
s at 300 K are obtained based on the QHA.

	a (Å)	b (Å)	c (Å)	α (º)	β (º)	γ (º)	Static volumes (Å^3)	Volumes at 300 K (Å^3)	
SiO_4)	4.738	10.115	5.941	90	90	90	284.714	290.274	LDA
	4.790	10.303	6.036	90	90	90	297.885		GG
K	4.752	10.192	5.978	90	90	90		289.529	
Si_2O_6)	9.692	8.835	5.213	90	105.35	90	430.477	439.677	
	9.879	8.986	5.308	90	106.48	90	451.844		GG
K	9.745	8.899	5.251	90	105.63	90		438.532	Ca
$MgSiO_3$)	18.110	8.755	5.138	90	90	90	814.640	832.179	LDA
	18.398	8.920	5.228	90	90	90	857.968		GG
K	18.251	8.814	5.181	90	90	90		833.438	Ya
Si_3O_{12})	11.357	11.357	11.357	90	90	90	1464.717	1495.661	
	11.545	11.545	11.545	90	90	90	1538.958		
K	11.454	11.454	11.454	90	90	90		1502.855	P
$_2O_4$)	8.013	8.013	8.013	90	90	90	514.470	523.131	
	8.185	8.185	8.185	90	90	90	548.442		GG
K	8.080	8.080	8.080	90	90	90		527.465	Pe
$gAl_{15})O_{32}$)	8.007	8.007	8.023	89.87	89.87	89.86	514.382	523.062	
CrO_4)	8.145	8.136	8.145	90.35	88.76	90.35	539.671	548.046	
$MgCr_2O_4$)	8.235	8.328	8.235	89.34	91.31	89.34	564.463	572.989	
	8.357	8.431	8.357	89.49	91.02	89.49	588.7366		
K	8.334	8.334	8.334	90	90	90		578.884	O'Ne
CO_3)	4.619	4.619	14.605	90	90	120	269.899	276.550	
	4.672	4.672	15.183	90	90	120	286.974		GG
K	4.634	4.634	15.018	90	90	120		279.272	
TiO_3)	5.040	5.040	13.743	90	90	120	302.336	307.919	LD
	5.125	5.125	14.014	90	90	120	318.818		
K	5.054	5.054	13.898	90	90	120		307.435	Ya
$MgFeTi_2O_6$)	5.072	5.072	13.717	90	90	120	305.551	311.000	LD
$g_2Fe_4Ti_6O_{18}$)	5.081	5.081	13.711	90	90	120	306.524	311.115	
$MgFe_2O_4$)	8.303	8.298	8.298	89.90	90.03	90.03	571.758	579.303	

Table 2. The average Mg-O bond lengths, coordination numbers, and force constants of Mg in minerals.

Minerals	Static LDA (Å)	LDA at 300 K (Å)	Static GGA (Å)	Exp. at 300 K (Å)	Coordination number (CN)	<F> (N/m)
Forsterite (Mg_2SiO_4)	2.0956	2.1109	2.1325	2.1115	6	182.1
Diopside ($MgCaSi_2O_6$)	2.0549	2.0764	2.1030	2.0764	6	195.1
Orthopyroxene ($MgSiO_3$)	2.0873	2.1072	2.1410	2.1146	6	186.9
Pyrope ($Mg_3Al_2Si_3O_{12}$)	2.2641	2.2685	2.2851	2.2694	8	110.1
Spinel ($MgAl_2O_4$)	1.9295	1.9429	1.9640	1.9262	4	250.8
*Spinel ($(Mg_7Al)(MgAl_{15})O_{32}$)	1.9484	-	-	-	4.25	247.5
Spinel ($MgAlCrO_4$)	1.9480	1.961	-	-	4	223.7
Magnesiochromite ($MgCr_2O_4$)	1.9530	1.966	-	1.959	4	212.3
Magnesite ($MgCO_3$)	2.0763	2.0962	2.1290	2.1009	6	171.2
Geikielite ($MgTiO_3$)	2.0889	2.1060	2.1229	2.1071	6	169.3
Geikielite-ilmenite ($MgFeTi_2O_6$)	2.0868	2.1039	-	-	6	167.5
Geikielite-ilmenite ($Mg_2Fe_4Ti_6O_{18}$)	2.0897	2.1041	-	-	6	165.8
Magnesioferrite ($^{M}MgFe_2O_4$)	2.0598	2.0702	-	-	6	191.4
Magnesioferrite ($^{T}MgFe_2O_4$)	1.9712	1.9900	-	-	4	190.0
†Majorite ($MgSiO_3$)	2.2163	2.2351	2.2640	2.2264	7.5	147.7
Wadsleyite (Mg_2SiO_4)	2.0688	2.0840	2.0973	2.0828	6	206.1
Ringwoodite (Mg_2SiO_4)	2.0561	2.0673	2.0794	2.0664	6	219.5
Bridgmanite ($MgSiO_3$)	2.1937	2.2084	2.2216	2.2030	8	177.4
Periclase (MgO)	2.0960	2.1102	2.1192	2.1055	6	199.2

The sources of experimental data are listed in Table 1.

*In this disordered spinel, 12.5 mol% of Mg occupies the octahedral sites with a CN of 6, and therefore, the average CN is 4.25. The average Mg-O bond lengths for octahedral and tetrahedral Mg are 2.0222 and 1.9326 Å, respectively.

†Majorite has a tetragonal structure with the chemical formula $^{VIII}Mg_3{}^{VI}(MgSi)(SiO_4)_3$. Three Mg cations are eight-fold coordinated and one Mg cation is six-fold coordinated. Thus, the average CN of Mg in majorite is 7.5. The average ^{VIII}Mg-O and ^{VI}Mg-O bond lengths are 2.2619 Å and 2.0339 Å based on our

Table 3. Calculated reduced partition function ratios of $^{26}Mg/^{24}Mg$ ($10^3 ln\beta$) for mantle minerals at static zero pressure as a function of temperature. The polynomial fitting equation is: $10^3 ln\beta$ (‰) = $ax+bx^2+cx^3$, where $x=10^6/T^2$, T is temperature in Kelvin. Temperature range for polynomial fittings is from 400 K to 2000 K.

Minerals	a	b	c	$10^3 ln\beta$ (‰) at 1000 K
Forsterite (Mg_2SiO_4)	2.565	-1.735E-02	1.947E-04	2.548
Diopside ($MgCaSi_2O_6$)	2.767	-1.812E-02	1.877E-04	2.749
Orthopyroxene ($MgSiO_3$)	2.641	-1.878E-02	2.136E-04	2.622
Pyrope ($Mg_3Al_2Si_3O_{12}$)	1.588	-9.624E-03	1.317E-04	1.579
Spinel ($MgAl_2O_4$)	3.548	-3.514E-02	4.975E-04	3.514
Spinel ($(Mg_7Al)(MgAl_{15})O_{32}$)	3.501	-3.448E-02	5.511E-04	3.467
Spinel ($MgAlCrO_4$)	3.148	-2.694E-02	3.381E-04	3.122
Magnesiochromite ($MgCr_2O_4$)	2.987	-2.395E-02	2.832E-04	2.964
Magnesite ($MgCO_3$)	2.423	-1.700E-02	2.603E-04	2.407
Geikielite ($MgTiO_3$)	2.383	-1.344E-02	1.204E-04	2.370
Geikielite-ilmenite ($MgFeTi_2O_6$)	2.358	-1.284E-02	1.093E-04	2.345
Geikielite-ilmenite ($Mg_2Fe_4Ti_6O_{18}$)	2.334	-1.260E-02	1.065E-04	2.321
Magnesioferrite ($^{M}MgFe_2O_4$)	2.695	-1.586E-02	1.291E-04	2.679
Magnesioferrite ($^{T}MgFe_2O_4$)	2.674	-1.848E-02	1.886E-04	2.656
Majorite ($MgSiO_3$)	2.099	-1.382E-02	1.644E-04	2.085
Wadsleyite (Mg_2SiO_4)	2.906	-2.061E-02	2.232E-04	2.885
Ringwoodite (Mg_2SiO_4)	3.098	-2.302E-02	2.530E-04	3.076
Bridgmanite ($MgSiO_3$)	2.510	-1.930E-02	2.489E-04	2.491
Periclase (MgO)	2.762	-1.732E-02	1.626E-04	2.745
*Dolomite ($MgCaC_2O_6$)	2.571	-1.177E-02	2.400E-04	2.558
*Calcite ($Mg_{1/12}Ca_{11/12}CO_3$)	2.136	-1.317E-02	1.190E-04	2.122

*The results are from Wang et al. (2017a).

ated reduced partition function ratios of $^{26}Mg/^{24}Mg$ ($10^3 ln\beta$) for mantle minerals at a function of pressure and temperatu

hod. The polynomial fitting equation is: $10^3 ln\beta$ (‰) = $(a+b*P+c*P^2)*(10^6/T^2)+(d+e*P+f*P^2)*(10^6/T^2)^2+(g+h*P+l*P^2)*(10^6$

and T is temperature in Kelvin. Temperature for polynomial fittings ranges from 400 K to 2000 K.

	a	b	c	d	e	f	g	h	
)	2.076	7.183E-02	-4.672E-04	1.049E-01	-3.359E-03	5.009E-05	-1.192E-02	2.739E-04	-5.5
$_6$)	2.246	8.548E-02	-7.425E-04	1.025E-01	-3.639E-03	5.172E-05	-1.169E-02	2.834E-04	-5.5
O_3)	2.246	6.206E-02	-7.331E-05	6.748E-02	-1.405E-04	-8.619E-05	-8.171E-03	-6.569E-05	8.82
$_{12}$)	1.302	2.732E-02	1.784E-04	4.919E-02	1.266E-03	-4.067E-05	-5.543E-03	-1.482E-04	3.78
	3.058	6.216E-02	-3.720E-04	8.472E-02	-3.421E-03	5.116E-05	-1.132E-02	2.555E-04	-5.5
)O_{32})	3.014	5.980E-02	-2.454E-04	8.306E-02	-2.481E-03	1.220E-05	-1.101E-02	1.577E-04	-1.5
)	2.736	5.647E-02	-1.233E-04	6.945E-02	-1.989E-03	1.310E-06	-9.122E-03	1.170E-04	-7.0
Cr_2O_4)	2.611	6.596E-02	-4.429E-04	6.135E-02	-4.495E-03	9.388E-05	-8.197E-03	3.802E-04	-1.0
)	1.852	8.151E-02	-6.499E-04	1.174E-01	-3.625E-03	5.687E-05	-1.299E-02	2.944E-04	-6.2
)	1.873	6.067E-02	-2.328E-04	1.116E-01	-2.462E-03	1.617E-05	-1.227E-02	1.959E-04	-2.0
	1.808	6.830E-02	-3.739E-04	1.306E-01	-4.609E-03	6.142E-05	-1.426E-02	4.187E-04	-6.8
	1.858	6.222E-02	-3.344E-04	1.149E-01	-5.439E-03	1.533E-04	-1.282E-02	5.322E-04	-1.6
e_2O_4)	2.452	2.941E-02	6.431E-04	2.943E-02	4.608E-03	-1.027E-04	-4.039E-03	-4.908E-04	7.22
e_2O_4)	2.247	5.620E-02	9.565E-04	1.046E-02	1.907E-02	-1.328E-03	1.490E-03	-2.944E-03	1.82
	1.774	3.599E-02	3.827E-06	5.534E-02	3.144E-05	-1.721E-05	-6.554E-03	-3.859E-05	1.58
$_4$)	2.416	6.086E-02	-2.440E-04	9.795E-02	-2.208E-03	1.485E-05	-1.149E-02	1.587E-04	-1.7
O_4)	2.621	5.657E-02	-1.832E-04	9.024E-02	-1.721E-03	5.186E-06	-1.091E-02	1.087E-04	-7.7
$_3$)	2.092	3.481E-02	-3.340E-05	8.393E-02	-9.066E-04	1.845E-07	-9.910E-03	5.081E-05	-1.1
	2.357	4.632E-02	-7.245E-05	1.070E-01	-1.279E-03	7.383E-07	-1.207E-02	7.262E-05	-1.6

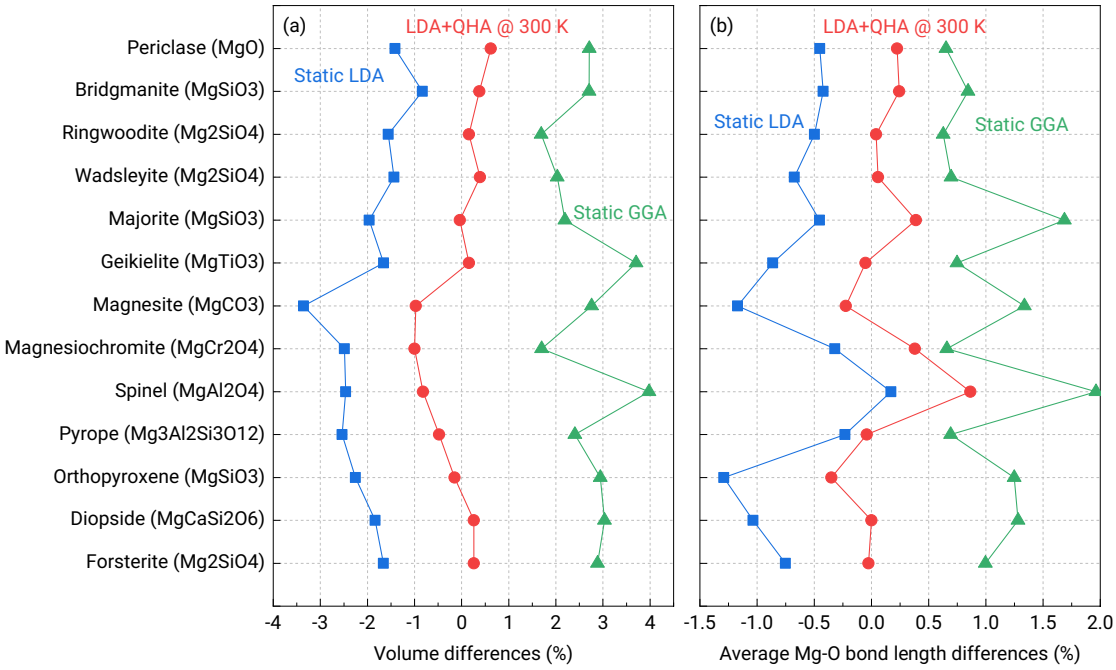

Figure 1. The differences in (a) mineral volumes and (b) average Mg-O bond lengths between first-principles calculations and experimental measurements. Magnesioferrite and geikielite-ilmenite solid solutions are not included because there are no experimental results. Static LDA and GGA refer to the static calculations at 0 GPa within the LDA and GGA, respectively. LDA+QHA represents the results at 300 K and 0 GPa calculated based on the QHA. All absolute values are listed in Table 1 and 2.

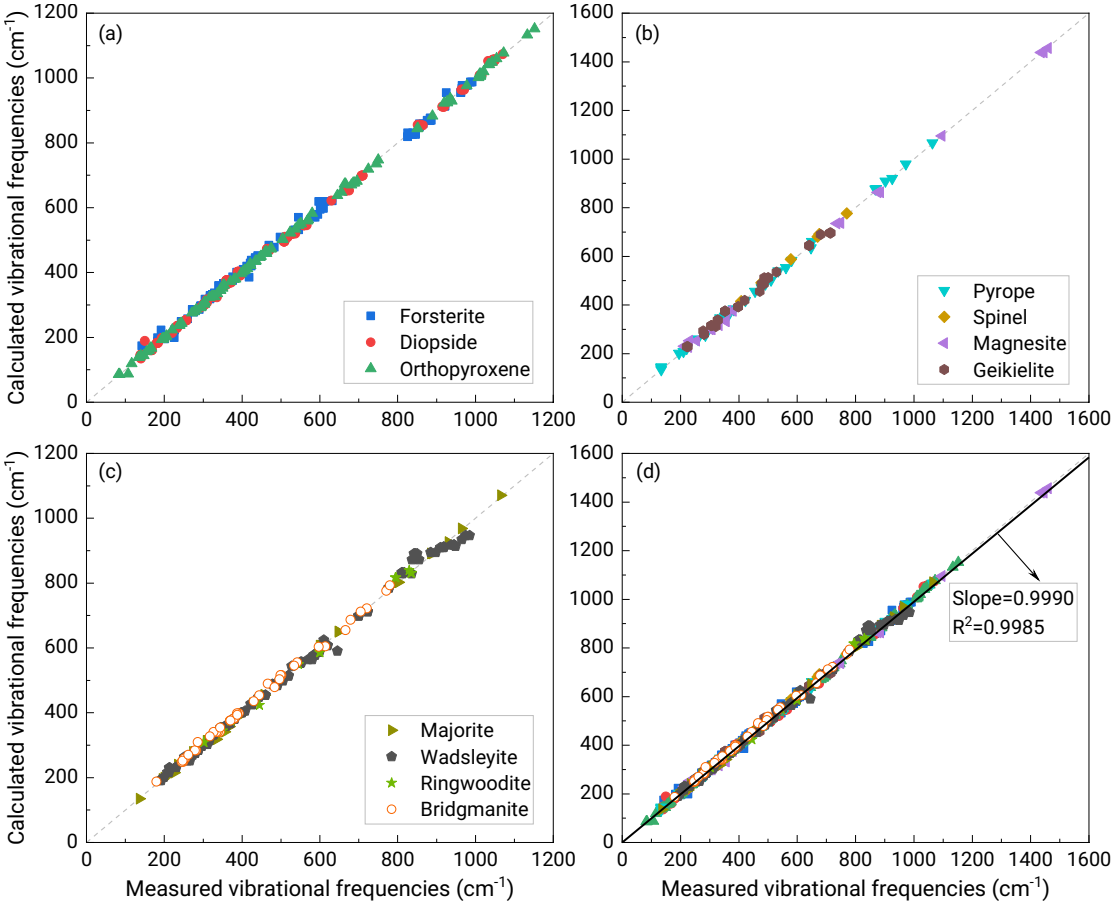

Figure 2. The calculated vibrational frequencies using LDA compared to the measured results. The dash lines in four panels refer to the 1:1 scale and the solid line in (d) represents the fitting line between the theoretical results and experimental measurements. The slope between calculated frequencies and measured frequencies is 0.999±0.002 (1σ, R^2 = 0.9985). All raw data can be found in Table S2.

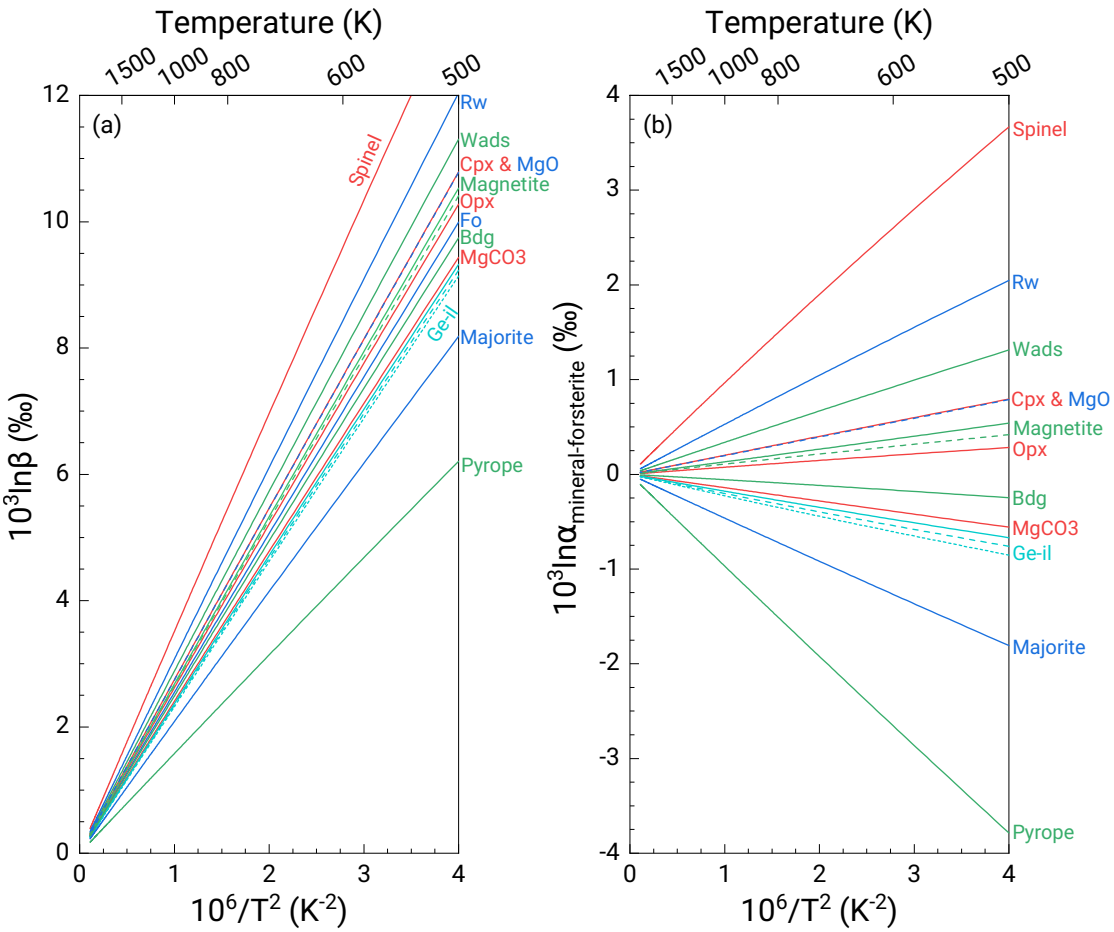

Figure 3. (a) The 10^3lnβ of $^{26}Mg/^{24}Mg$ of mantle minerals at 0 GPa calculated based on the static LDA method, and (b) the 10^3lnα between other minerals and forsterite. The polynomial fitting parameters of 10^3lnβ as a function of temperature are listed in Table 3. Mineral abbreviations: Rw, ringwoodite; Wads, wadsleyite; Cpx, diopside; MgO, periclase; Opx, orthopyroxene; Fo, forsterite; Bdg, bridgmanite; MgCO3, magnesite; Ge-il, geikielite-ilmenite solid solutions.

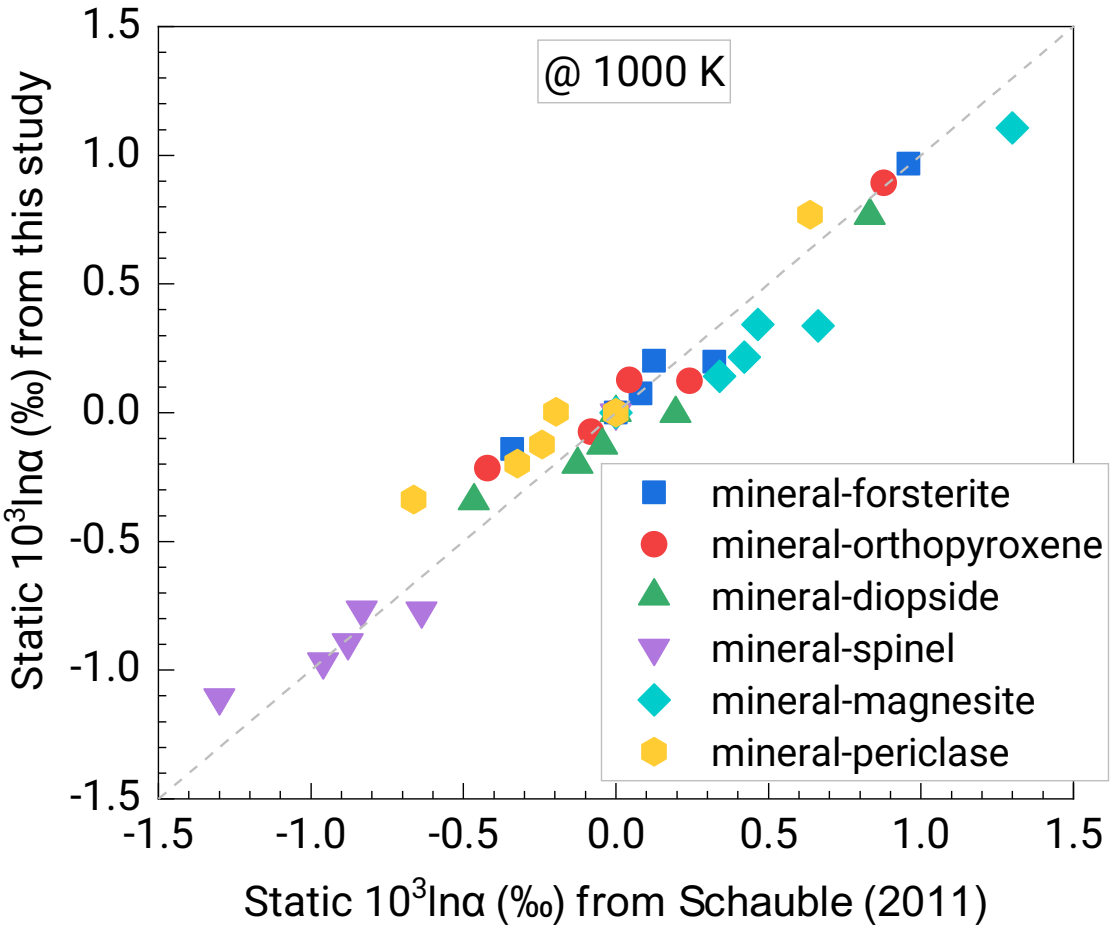

Figure 4. The $10^3 \ln\alpha$ among forsterite, orthopyroxene, diopside, spinel ($MgAl_2O_4$), magnesite, and periclase calculated using the static LDA method compared with those calculated using the static GGA method in Schauble (2011).

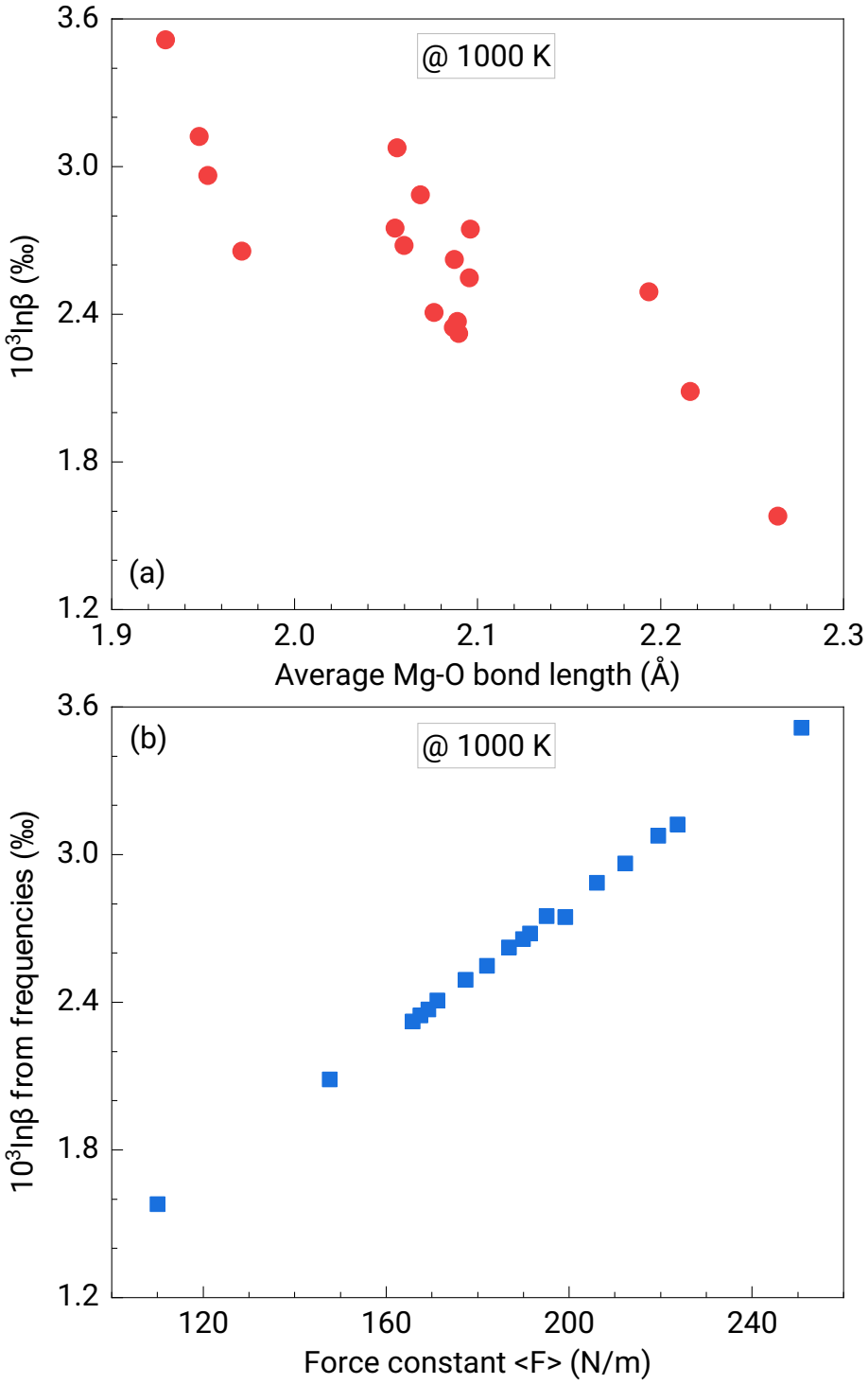

Figure 5. The 10^3lnβ of $^{26}Mg/^{24}Mg$ at 1000 K calculated using the static LDA method versus (a) the average Mg-O bond length and (b) the force constant of Mg.

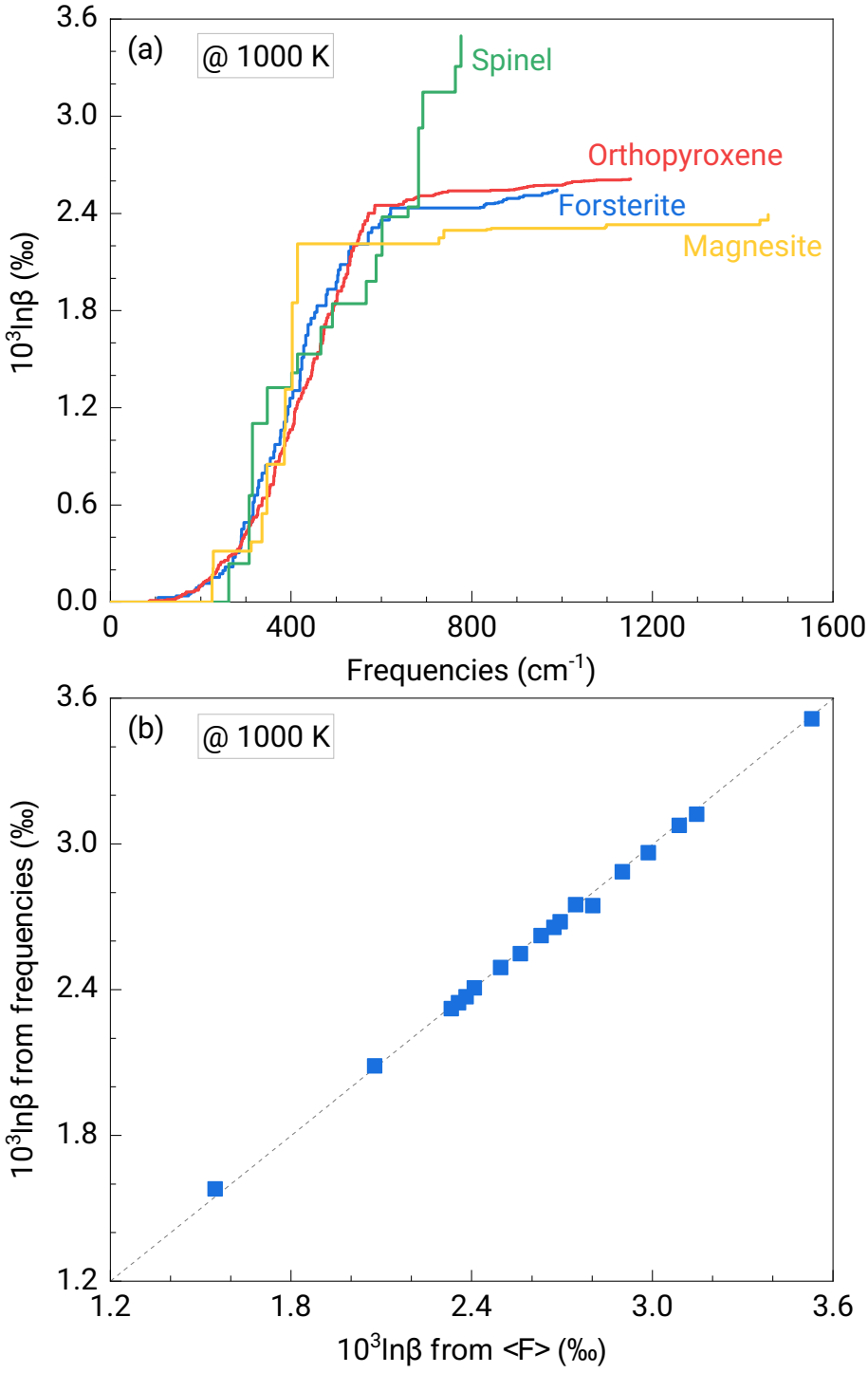

Figure 6. (a) The $10^3 \ln\beta$ integral of forsterite, orthopyroxene, magnesite, and spinel ($MgAl_2O_4$) at 0 GPa calculated using the static LDA method versus the upper-limit frequency values that are used in the calculations using Eq. (3). (b) The $10^3 \ln\beta$ calculated from frequencies using Eq. (3) compared to those estimated from the force constant of Mg.

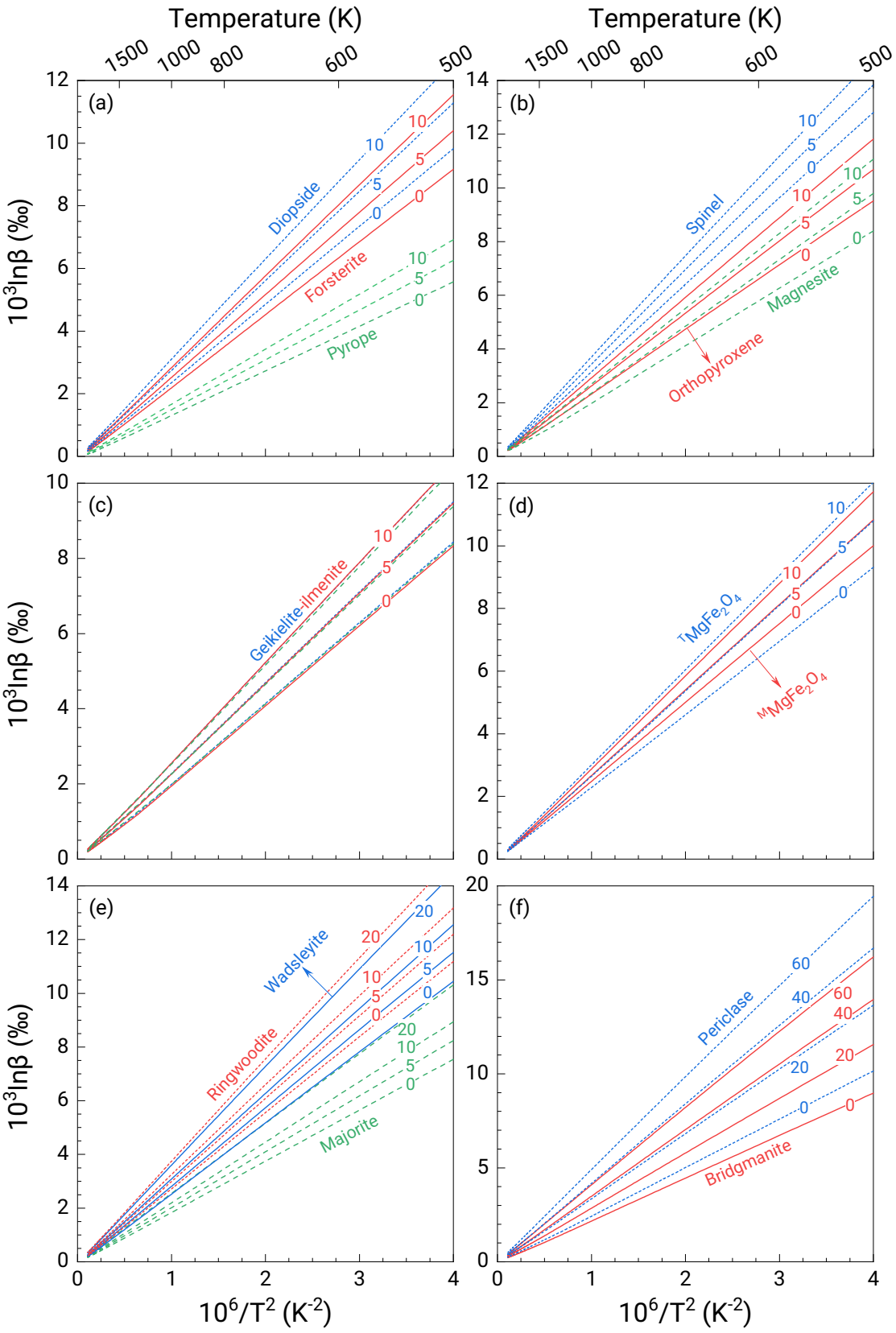

Figure 7. The $10^3 ln\beta$ of $^{26}Mg/^{24}Mg$ of mantle minerals as a function of temperature at different pressures calculated using the LDA+QHA method. The values in the middle of lines in all panels refer to the pressure values in GPa.

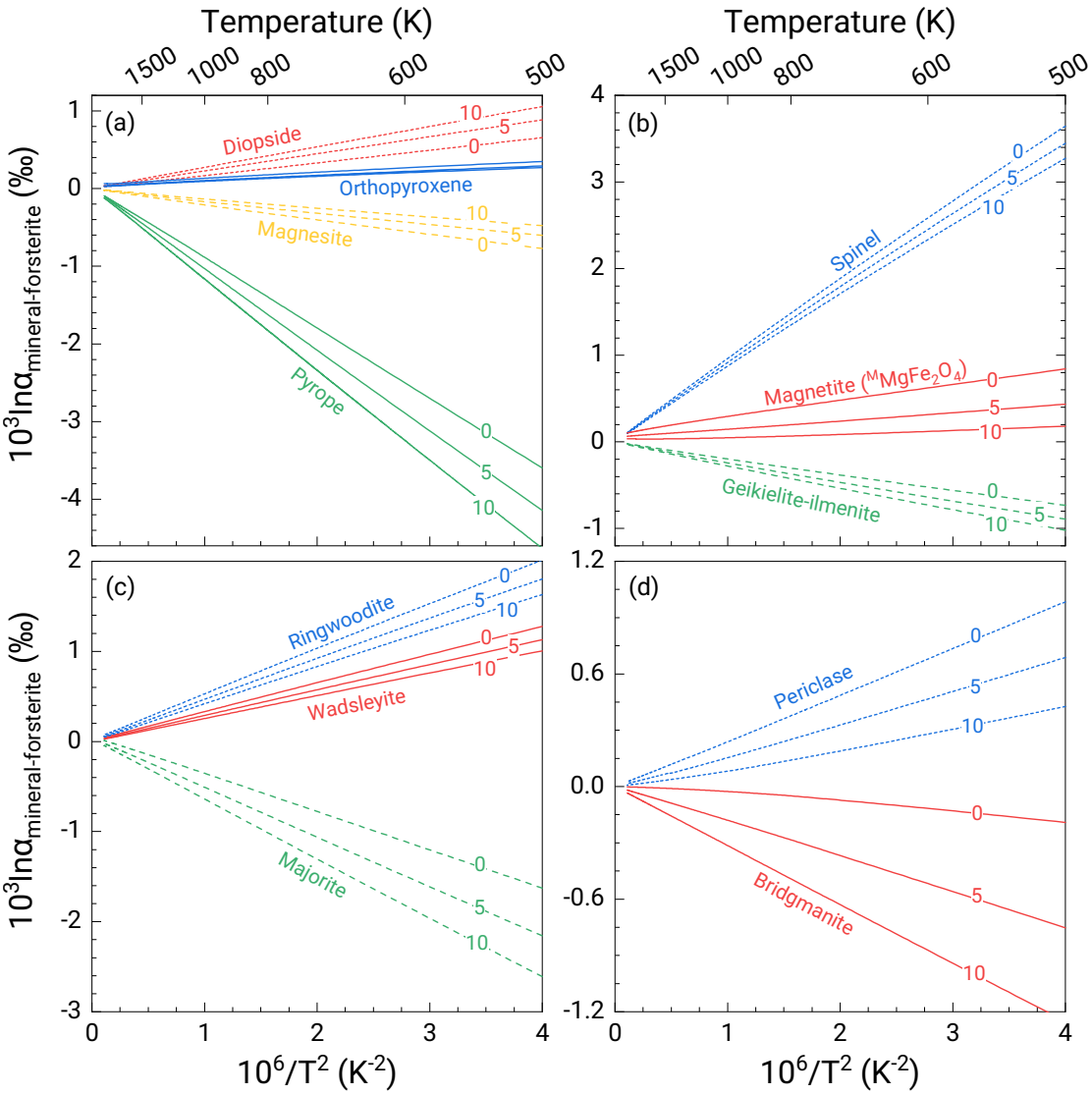

Figure 8. The $10^3 ln\alpha$ of $^{26}Mg/^{24}Mg$ between other minerals and forsterite as a function of temperature at different pressures (0, 5, and 10 GPa) calculated using the LDA+QHA method.

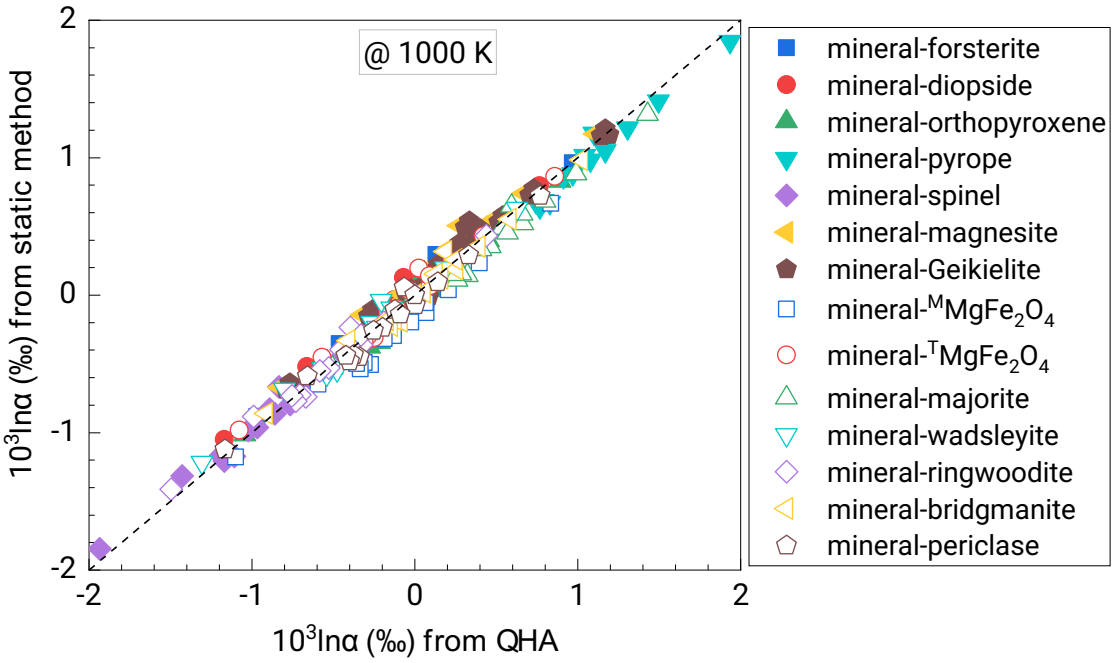

Figure 9. The 10^3lnα of $^{26}Mg/^{24}Mg$ between different mineral pairs calculated using the LDA+QHA method compared with those calculated using the static LDA method.

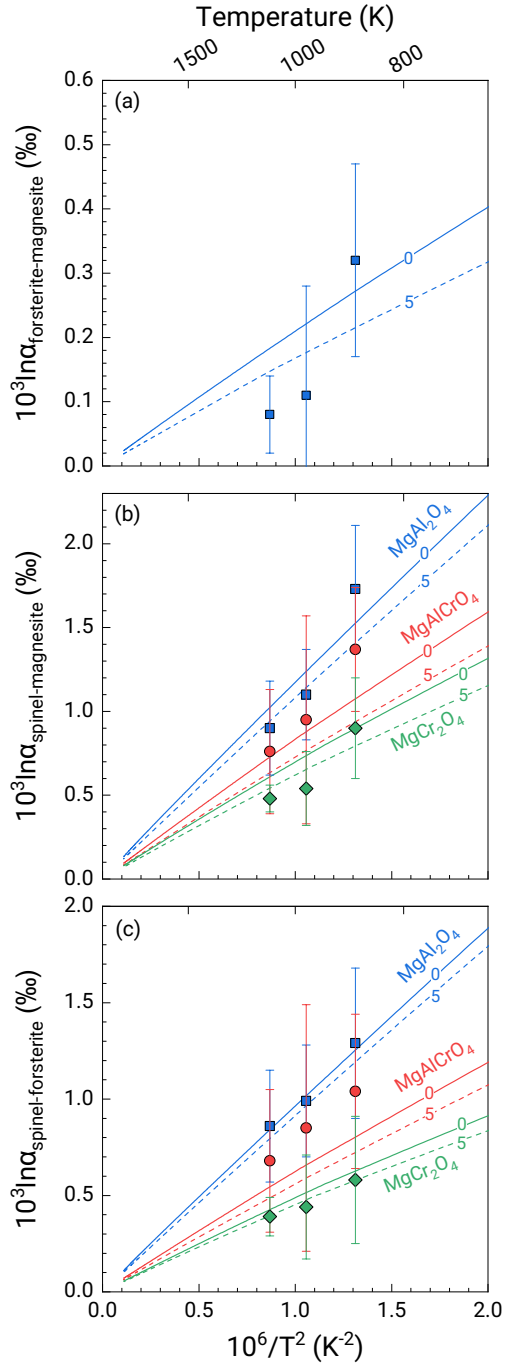

Figure 10. Calculated $10^3\ln\alpha$ of $^{26}Mg/^{24}Mg$ among spinel, forsterite, and magnesite compared with experimental measurements. (a) $10^3\ln\alpha$ between forsterite and magnesite, (b) $10^3\ln\alpha$ between spinel ($MgAl_2O_4$, $MgAlCrO_4$, and $MgCr_2O_4$) and magnesite, and (c) $10^3\ln\alpha$ between spinel ($MgAl_2O_4$, $MgAlCrO_4$, and $MgCr_2O_4$) and forsterite. Solid and dash lines represent our calculated results at 0 and 5 GPa using the LDA+QHA method, respectively. Experimental data: blue squares, Macris et al. (2013); red circles and green diamonds, Tang et al. (2021).

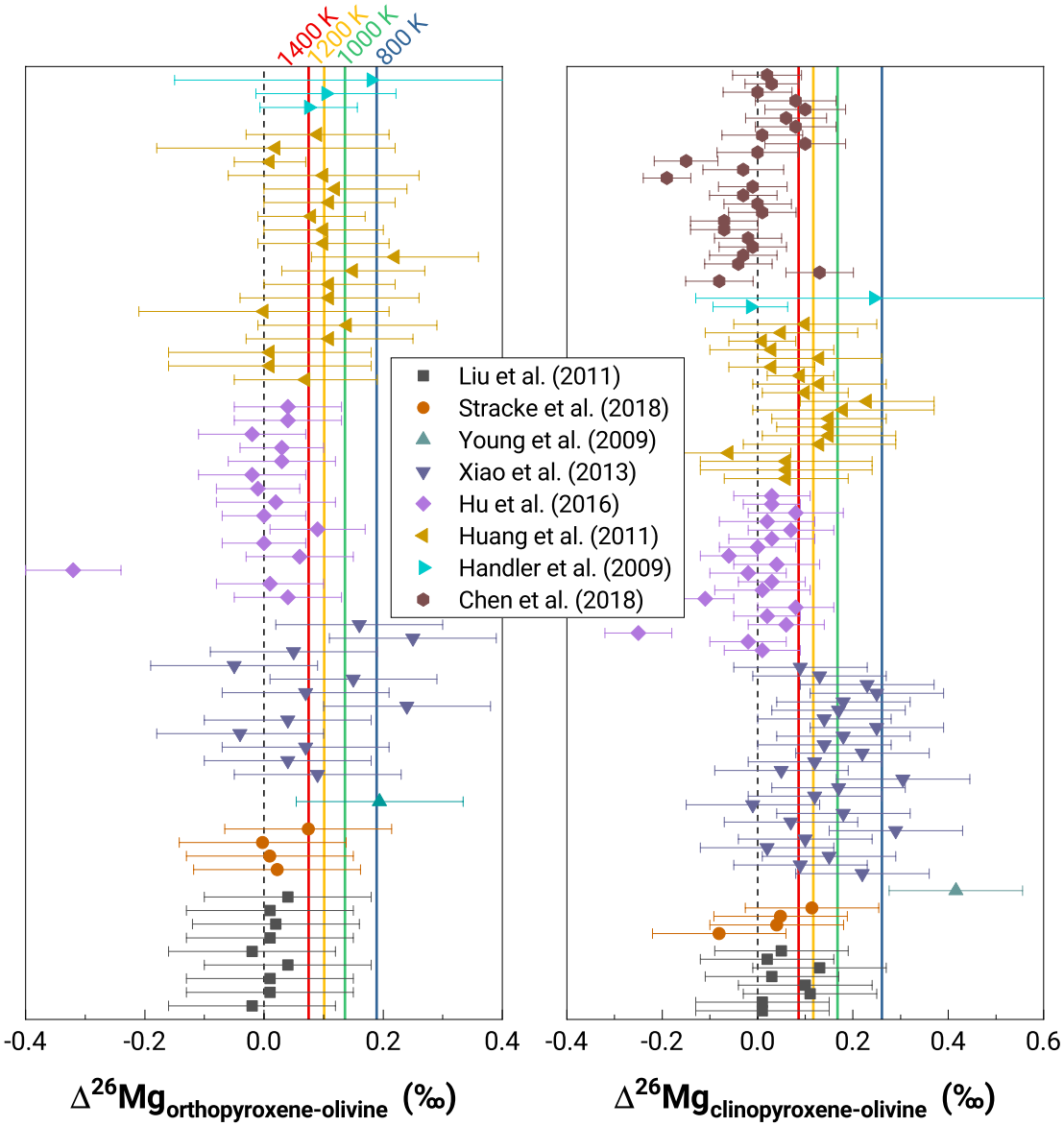

Figure 11. Comparison of observed orthopyroxene-olivine and clinopyroxene-olivine Mg isotope fractionation ($\Delta^{26}Mg_{orthopyroxene\text{-}olivine}$ and $\Delta^{26}Mg_{clinopyroxene\text{-}olivine}$) in natural peridotites, pyroxenites, xenoliths, and layered mafic intrusions with the calculated results in this study. Literature data are from (Chen et al., 2018; Handler et al., 2009; Yan Hu et al., 2016; Huang et al., 2011b; Liu et al., 2011; Stracke et al., 2018; Xiao et al., 2013; Young et al., 2009). The blue, green, yellow, and red lines refer to the calculated $10^3 ln\alpha_{orthopyroxene\text{-}forsterite}$ and $10^3 ln\alpha_{diopside\text{-}forsterite}$ values at 800, 1000, 1200, and 1400 K, respectively.

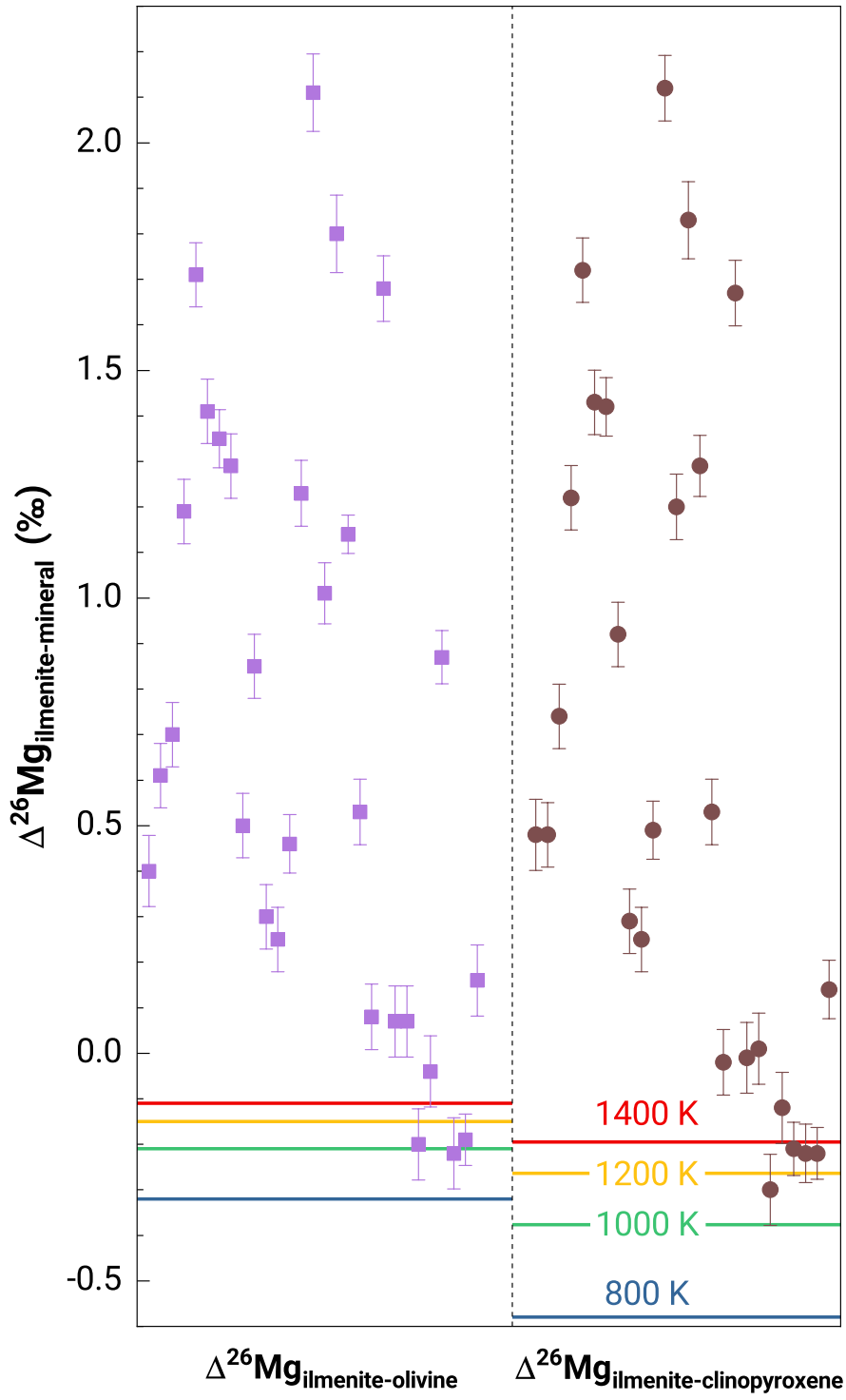

Figure 12. Mg isotope fractionation between ilmenite and olivine ($\Delta^{26}Mg_{ilmenite\text{-}olivine}$) and between ilmenite and clinopyroxene ($\Delta^{26}Mg_{ilmenite\text{-}clinopyroxene}$) in the Baima layered mafic intrusion compared with the calculated results in this study. The $\Delta^{26}Mg_{ilmenite\text{-}olivine}$ and $\Delta^{26}Mg_{ilmenite\text{-}clinopyroxene}$ data are from Chen et al. (2018). The blue, green, yellow, and red lines mark the calculated $10^3\ln\alpha_{ilmenite\text{-}orthopyroxene}$ and $10^3\ln\alpha_{ilmenite\text{-}diopside}$ values at 800, 1000, 1200, and 1400 K, respectively.

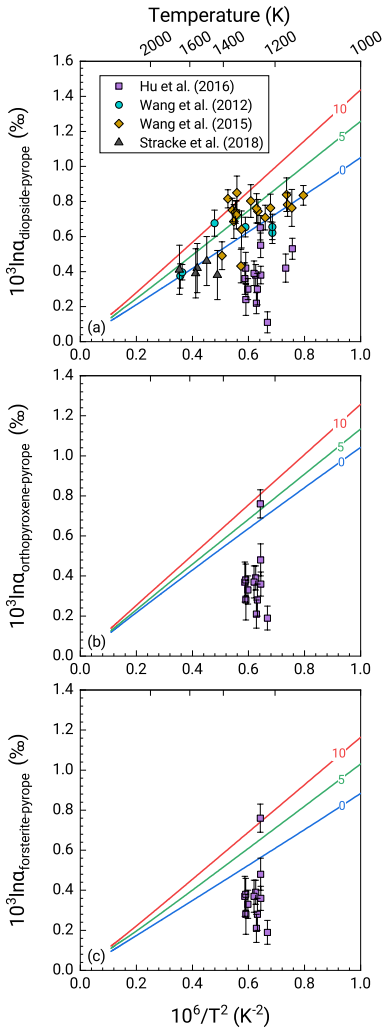

Figure 13. Comparison of observed clinopyroxene-garnet, orthopyroxene-garnet, and olivine-garnet Mg isotope fractionation ($\Delta^{26}Mg_{clinopyroxene\text{-}garnet}$, $\Delta^{26}Mg_{orthopyroxene\text{-}garnet}$, and $\Delta^{26}Mg_{olivine\text{-}garnet}$) in Hannuoba garnet-bearing xenoliths (squares, Yan Hu et al., 2016), cratonic eclogites from Koidu, Kaalvallei, and Bellsbank kimberlites (circles, Wang et al., 2012; diamonds, Wang et al., 2015), and Hawaiian garnet pyroxenites (triangles, Stracke et al., 2018) with the calculated results in this study. The equilibrium temperatures for Hannuoba xenoliths were estimated based on the Mg-Fe partitioning between clinopyroxene and orthopyroxene (Yan Hu et al., 2016), while those for cratonic eclogites and Hawaiian pyroxenites were calculated using the garnet-clinopyroxene Fe-Mg geothermometer (Bizimis et al., 2005; Wang et al., 2015; Williams et al., 2009). The blue, green, and red lines refer to (a) $10^3\ln\alpha_{diopside\text{-}pyrope}$, (b) $10^3\ln\alpha_{orthopyroxene\text{-}pyrope}$, and (c) $10^3\ln\alpha_{forsterite\text{-}pyrope}$ as a function of $10^6/T^2$ at 0, 5, and 10 GPa, respectively.

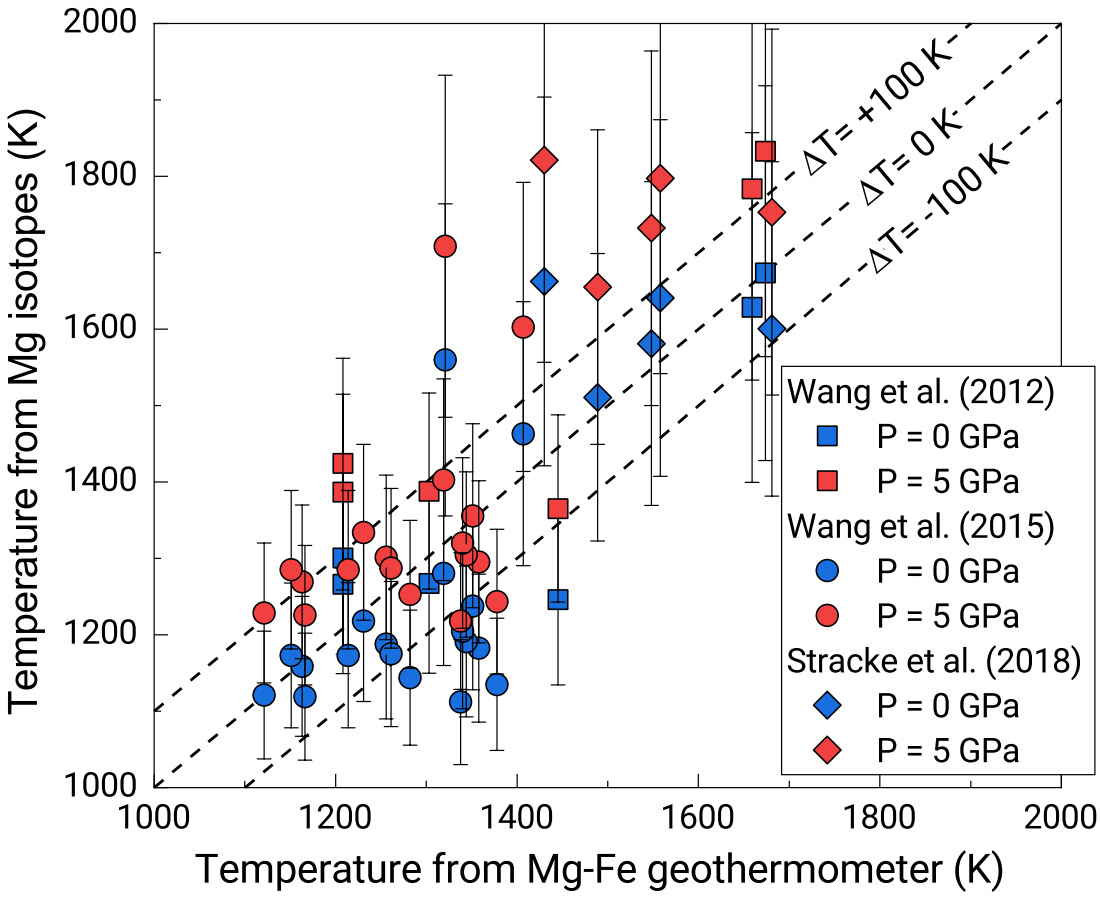

Figure 14. Temperatures estimated from $\Delta^{26}Mg_{clinopyroxene\text{-}garnet}$ compared with those estimated using the clinopyroxene-garnet Mg-Fe geothermometer. Data sources for $\Delta^{26}Mg_{clinopyroxene\text{-}garnet}$: circles, Wang et al. (2012); squares, Wang et al. (2015); diamonds, Stracke et al. (2018). Blue and red scatters refer to the results based on the temperature dependences of $10^3 ln\alpha_{diopside\text{-}pyrope}$ at 0 and 5 GPa, respectively.

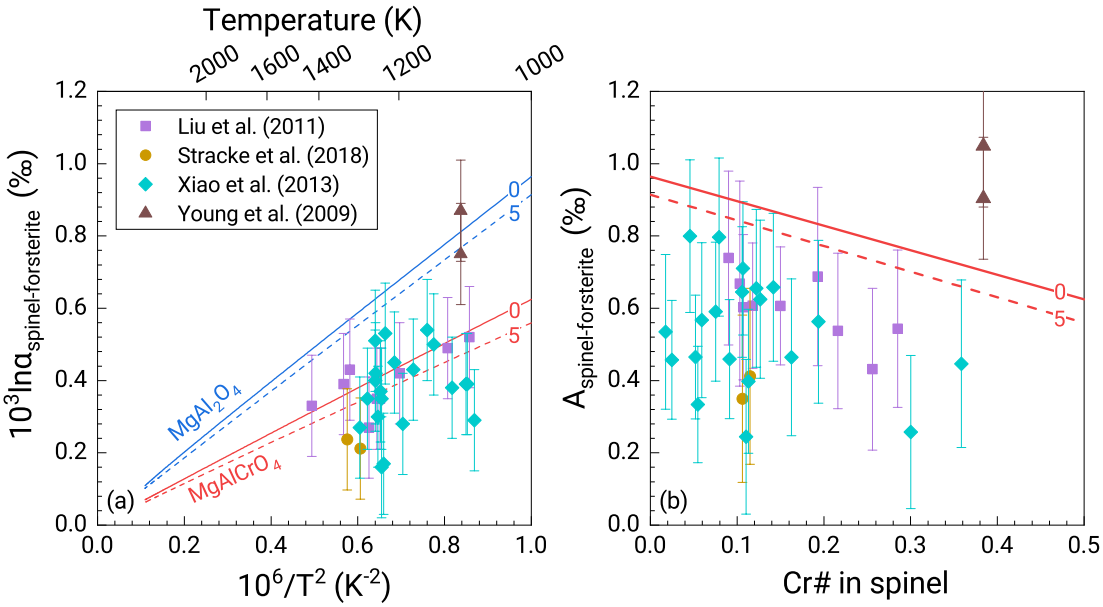

Figure 15. (a) Comparison of observed spinel-olivine Mg isotopic fractionation ($\Delta^{26}Mg_{spinel\text{-}olivine}$) in natural peridotites and xenoliths with the calculated results in this study. Literature data include San Carlos xenoliths (triangles, Young et al., 2009), north China craton peridotites (squares, Liu et al., 2011; diamonds, Xiao et al., 2013), and Hawaiian xenoliths (circles, Stracke et al., 2018). The temperatures for San Carlos xenoliths were estimated based on inversion parameter for Al-Mg ordering in spinel, whereas the temperatures of all other samples were calculated using the clinopyroxene-orthopyroxene Fe-Mg geothermometer. The blue and red lines represent the $10^3ln\alpha_{MgAl2O4\text{-}forsterite}$ and $10^3ln\alpha_{MgAlCrO4\text{-}forsterite}$ as a function of $10^6/T^2$, respectively. The solid and dash lines mark the calculated results at 0 and 5 GPa, respectively. (b) Correlation between the coefficient $A_{spinel\text{-}forsterite}$ ($A_{spinel\text{-}forsterite}$ = ($\Delta^{26}Mg_{spinel\text{-}olivine}$ or $10^3ln\alpha_{spinel\text{-}forsterite}$)*$T^2/10^6$) and Cr# in spinel (Cr# = Cr/(Cr+Al)). the coefficient $A_{spinel\text{-}forsterite}$ represents the corrected Mg isotope fractionation at 1000 K from the observed $\Delta^{26}Mg_{spinel\text{-}olivine}$ or the calculated $10^3ln\alpha_{spinel\text{-}forsterite}$ at a certain temperature. Error bars for $\Delta^{26}Mg_{spinel\text{-}olivine}$ (±0.14‰, 2SD) are drawn assuming an uncertainty of ±0.10‰ (2SD) on $\delta^{26}Mg_{olivine}$ and $\delta^{26}Mg_{spinel}$. The red solid and dash lines refer to the calculated results at 0 and 5 GPa, respectively, assuming a linear relationship between $10^3ln\alpha_{spinel\text{-}forsterite}$ and Cr# when Cr# varies from 0 to 0.5.

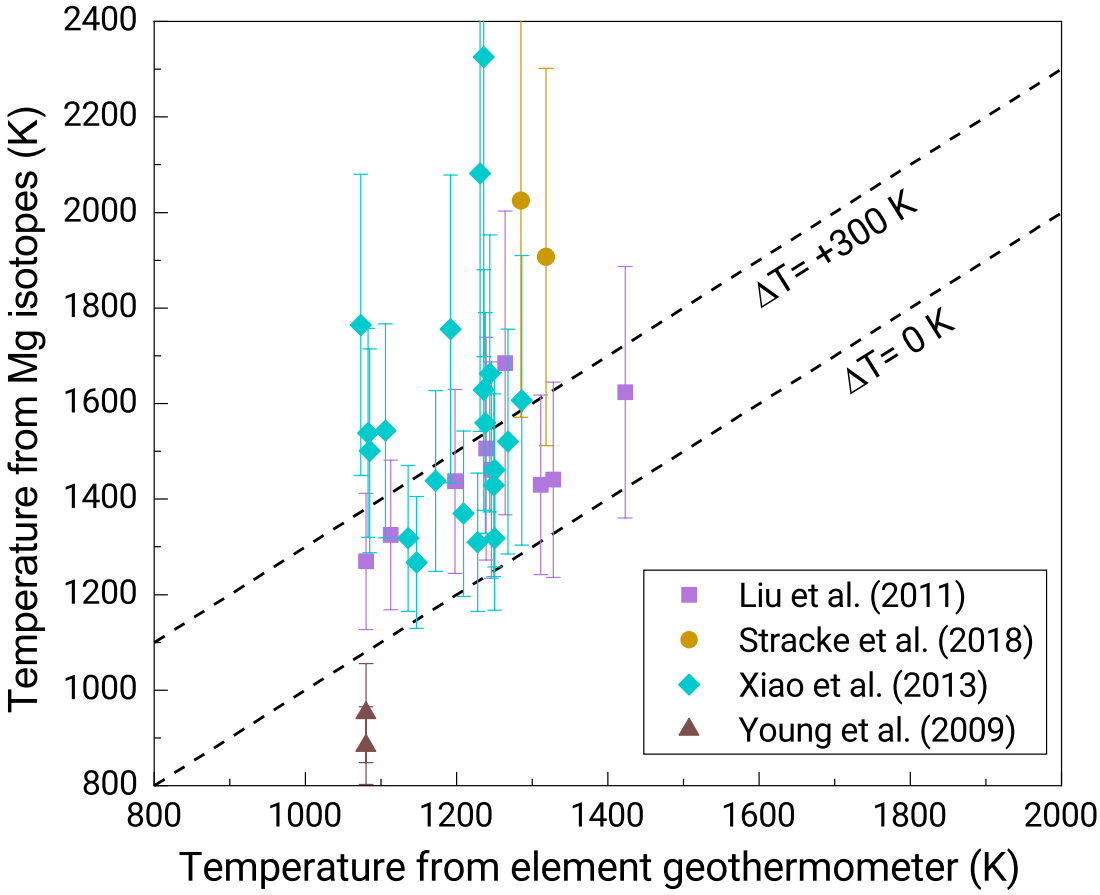

Figure 16. Temperatures estimated from $\Delta^{26}Mg_{spinel\text{-}olivine}$ compared with those estimated using the inter-mineral element geothermometers. Data sources: triangles, Young et al. (2009); squares, Liu et al., (2011); diamonds, Xiao et al. (2013); circles, Stracke et al. (2018). The errors for temperatures from Mg isotopes are estimated from the uncertainties of $\Delta^{26}Mg_{spinel\text{-}olivine}$ (±0.14 ‰, 2SD).

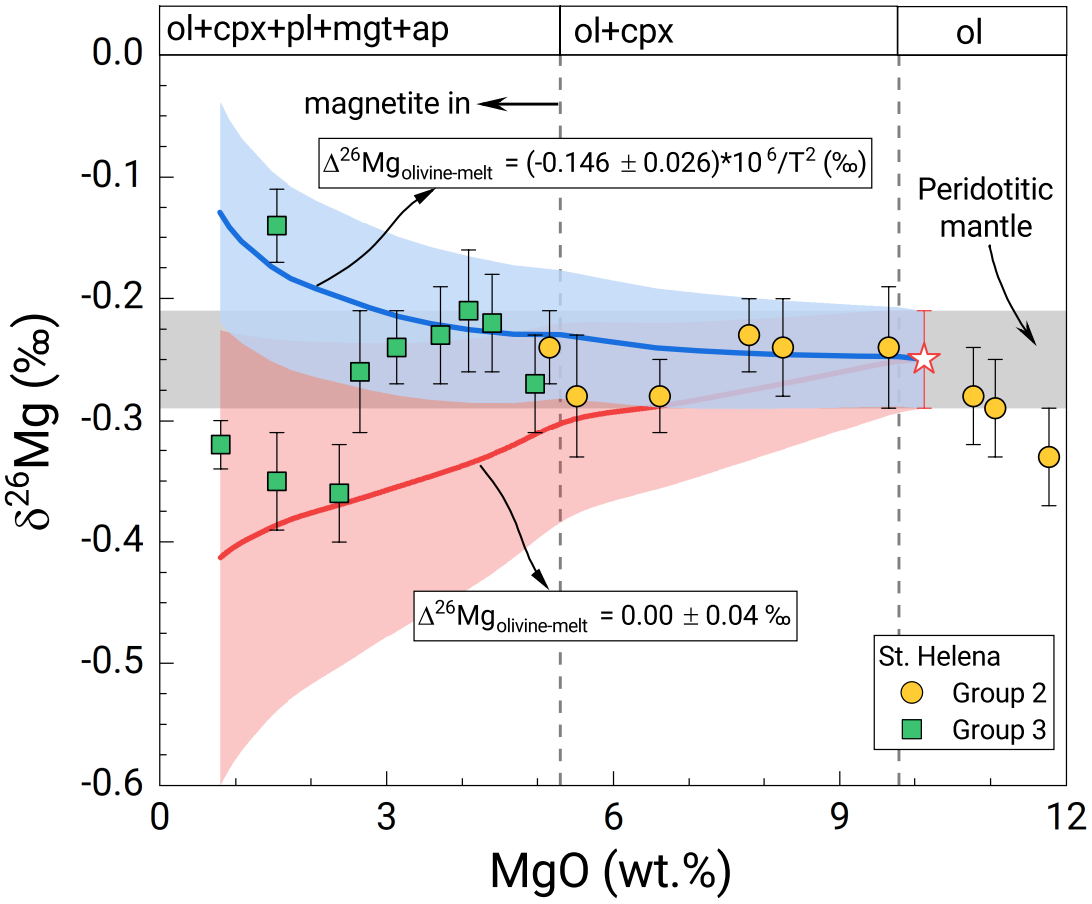

Figure 17. Mg isotopic variation during differentiation of St. Helena lavas. The δ^{26}Mg values of St. Helena group 2 and group 3 samples were measured by X.-J. Wang et al. (2021). The proportions and chemical compositions of segregated minerals and residual melts were calculated by X.-J. Wang et al. (2021) using the MELTS. Plagioclase (pl) and apatite (ap) are ignored in the calculation of melt δ^{26}Mg values because of their extremely low MgO contents. The grey range refers to the Mg isotopic composition of the peridotitic mantle (δ^{26}Mg = -0.25 ± 0.04 ‰; Teng, 2017), which is also assumed as the δ^{26}Mg value of primary melt. The red and blue regions refer to the modeling results with Mg isotope fractionation between olivine and melt ($\Delta^{26}Mg_{olivine\text{-}melt}$) of 0.00 ± 0.04 ‰ and (-0.146 ± 0.026)*10^6/T^2 ‰). Accordingly, the Mg isotope fractionation between clinopyroxene and melt ($\Delta^{26}Mg_{clinopyroxene\text{-}melt}$) and between magnetite and melt ($\Delta^{26}Mg_{magnetite\text{-}melt}$) at various temperatures can be derived from the temperature dependences of $10^3 ln\alpha_{clinopyroxene\text{-}forsterite}$ and $10^3 ln\alpha_{magnesioferrite\text{-}forsterite}$ calculated in this study.